Further development of NICE-OHMS

– an ultra-sensitive frequency-modulated cavity-enhanced laser-based spectroscopic technique for detection of molecules in gas phase

Patrick Ehlers

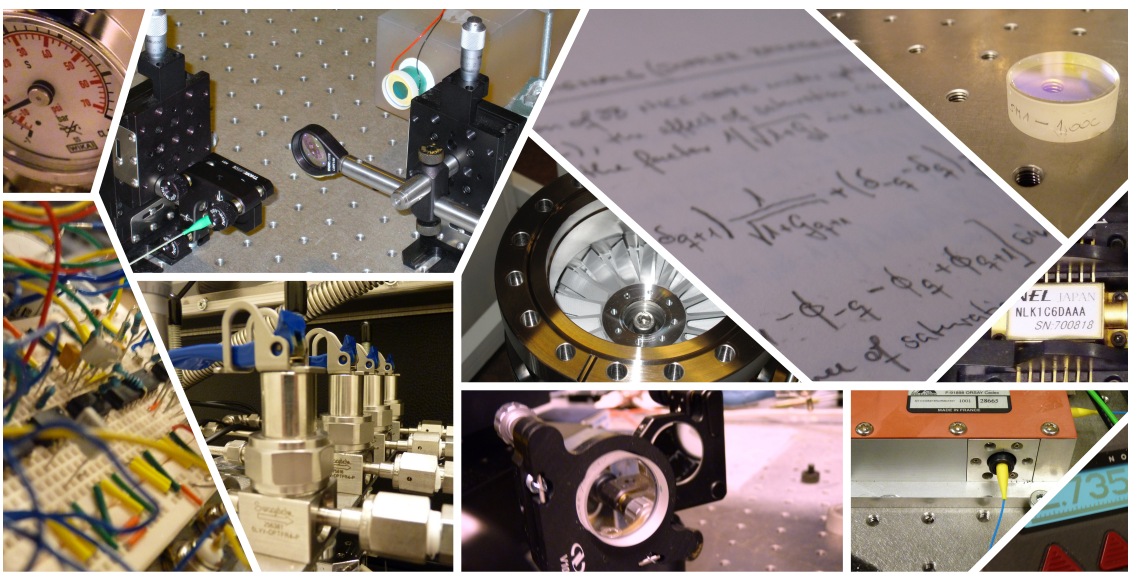

Department of Physics
Umeå university, Sweden
Doctoral thesis, 2014

Further development of NICE-OHMS
– an ultra-sensitive frequency-modulated cavity-enhanced laser-based spectroscopic technique for detection of molecules in gas phase

Patrick Ehlers

Doctoral thesis, 2014
Department of Physics
Umeå University
Sweden

Department of Physics
Umeå University
SE-901 87 Umeå , Sweden

ISBN 978-91-7601-107-2
Electronic version available at: http://umu.diva-portal.org/
Printed by Print & Media, Umeå University
Umeå, Sweden 2014

Hofstadter's Law: It always takes longer than
you expect, even when you take into account Hofstadter's Law.

Douglas Hofstadter, *Gödel, Escher, Bach: An Eternal Golden Braid*

Sammanfattning

Brusimmun kavitetsförstärkt optisk-heterodyndetekterad molekylärspektroskopi (NICE-OHMS) är en laser-baserad spektroskopisk teknik som förenar frekvensmodulation (för reducring av $1/f$-brus genom detektion vid en hög frekvens) och kavitetsförstärkning (KF, för en förlängning av den optiska väglängden) på ett unikt sätt. Korrekt realiserad uppvisar tekniken en inneboende immunitet mot omvandling av frekvensbrus till intensitetsbrus som många andra KF-tekniker är begränsade av. Allt detta ger tekniken en exceptionellt hög känslighet för molekyldetektion. Ursprungligen utvecklad för frekvensstandardändamål i slutet av 1990, har den sedan dess utvecklats för molekylspektroskopi och spårgasdetektering. Denna avhandling fokuserar på vidareutvecklingen av NICE-OHMS mot en tillämpbar, ultrakänslig detektionsteknik. Ett antal koncept har adresserats. Några av dessa är: *i*) Detektionskänsligheten hos fiberlaserbaserad NICE-OHMS har förbättrats till $10^{-12}\,\mathrm{cm}^{-1}$ området, vilket för detektion av C_2H_2 i gasfas motsvarar några få ppt (parts per biljon, $1{:}10^{12}$), genom att förbättra låsningen av lasern till en kavitetsmod med hjälp av en akustooptisk modulator. *ii*) Det har demonstrerats att NICE-OHMS kan realiseras mer kompakt med hjälp av en fiber-kopplad optisk cirkulator. *iii*) En systematisk och grundlig utredning av de experimentella förhållanden som ger maximala signaler, betecknade de optimala förhållanden, t.ex. modulering och demodulering och kavitetslängden, har utförts. Som ett led i detta har ett uttryck för NICE-OHMS linjeform bortom den konventionella triplett formalismen föreslagits och verifierats. *iv*) För att bredda tillämpbarheten av NICE-OHMS för detektering av tryckbreddade signaler har även en instrumentering baserad på en distribuerad-återkopplad (eng. *distributed feedback*, DFB) laser realiserats. *v*) I detta område kan inte Voigt profilen modellera signalen med den noggrannhet som krävs för en korrekt bedömning av analytkoncentrationer. Därför visar avhandlingen de första implementeringarna i NICE-OHMS av linjeprofiler som inkluderar Dicke avsmalning (eng. *Dicke narrowing*) och hastighetsberoende effekter (eng. *speed-dependent effects*). Emedan sådana profiler är välkända för absorption, fanns det inga uttryck för deras dispersiva motparter. Sådana uttryck har därför härletts och validerats av medföljande experiment. *vi*) Tillämpbarheten av tekniken för detektion av atomer, NICE-AAS, har diskuterats och förutspåtts.

Abstract

Noise-immune cavity-enhanced optical heterodyne molecular spectroscopy, NICE-OHMS, is a laser-based spectroscopic detection technique that comprises the concepts of frequency modulation (FM, for reduction of $1/f$-noise by detecting the signal at a high frequency) and cavity enhancement (CE, for a prolongation of the optical path length) in a unique way. Properly designed, this gives the technique an intrinsic immunity against the frequency-to-noise conversion that limits many other types of CE techniques. All this gives it an exceptionally high sensitivity for detection of molecular species. Although originally developed for frequency standard purposes in the late 1990s, soon thereafter development of the technique towards molecular spectroscopy and trace gas detection was initiated. This thesis focuses on the further development of Doppler-broadened NICE-OHMS towards an ultra-sensitive detection technique. A number of concepts have been addressed. A few of these are: *i*) The detection sensitivity of fiber-laser-based NICE-OHMS has been improved to the $10^{-12}\,\mathrm{cm}^{-1}$ range, which for detection of C_2H_2 corresponds to a few ppt (parts-per-trillion, $1{:}10^{12}$) in gas phase, by improving the locking of the laser to a cavity mode by use of an acousto-optic modulator. *ii*) It is shown that the system can be realized with a more compact footprint by implementation of a fiber-optic circulator. *iii*) A systematic and thorough investigation of the experimental conditions that provide maximum signals, referred to as the optimum conditions, e.g. modulation and demodulation conditions and cavity length, has been performed. As a part of this, an expression for the NICE-OHMS line shape beyond the conventional triplet formalism has been proposed and verified. *iv*) To widen the applicability of NICE-OHMS for detection of pressure broadened signals, also a setup based upon a distributed-feedback (DFB) laser has been realized. *v*) In this regime, the Voigt profile cannot model signal with the accuracy that is needed for a proper assessment of analyte concentrations. Therefore, the thesis demonstrates the first implementations of line profiles encompassing Dicke narrowing and speed-dependent effects to NICE-OHMS. While such profiles are well-known for absorption, there were no expressions available for their dispersion counterparts. Such expressions have been derived and validated by accompanying experiments. *vi*) The applicability of the technique for elemental detection, then referred to as NICE-AAS, has been prophesied.

List of Publications

This thesis is based on the following publications:

I. Distributed-feedback-laser-based NICE-OHMS in the pressure broadened regime

Optics Express Vol. 18, pages 18580–18591 (2010)

Aleksandra Foltynowicz, Junyang Wang, **Patrick Ehlers**, and Ove Axner

II. Dicke narrowing in the dispersion mode of detection and in noise-immune cavity-enhanced optical heterodyne molecular spectroscopy – theory and experimental verification

Journal of the Optical Society of America B Vol. 28, pages 2390–2401 (2011)

Junyang Wang, **Patrick Ehlers**, Isak Silander, and Ove Axner

III. Frequency modulation background signals from fiber-based electro optic modulators are caused by crosstalk

Journal of the Optical Society of America B Vol. 29, pages 916–923 (2012)

Isak Silander, **Patrick Ehlers**, Junyang Wang, and Ove Axner

IV. Fiber-laser-based noise-immune cavity-enhanced optical heterodyne molecular spectrometry instrumentation for Doppler-broadened detection in the 10^{-12} cm^{-1} $Hz^{-1/2}$ region

Journal of the Optical Society of America B Vol. 29, pages 1305–1315 (2012)

Patrick Ehlers, Isak Silander, Junyang Wang, and Ove Axner

V. Speed-dependent Voigt dispersion line-shape function: applicable to techniques measuring dispersion signals

Journal of the Optical Society of America B Vol. 29, pages 2971–2979 (2012)

Junyang Wang, **Patrick Ehlers**, Isak Silander, Jonas Westberg, and Ove Axner

VI. Speed-dependent effects in dispersion mode of detection and in noise-immune cavity-enhanced optical heterodyne molecular spectrometry: experimental demonstration and validation of predicted line shape

Journal of the Optical Society of America B Vol. 29, pages 2980–2989 (2012)

Junyang Wang, **Patrick Ehlers**, Isak Silander, and Ove Axner

VII. NICE-OHMS – Frequency Modulation Cavity-Enhanced Spectroscopy – Principles and Performance

Chapter 6 in "Cavity-Enhanced Spectroscopy and Sensing", Springer Series in Optical Sciences Vol. 179 (2014)

Ove Axner, **Patrick Ehlers**, Aleksandra Foltynowicz, Isak Silander, and Junyang Wang

VIII. Fiber-laser-based noise-immune cavity-enhanced optical heterodyne molecular spectrometry incorporating an optical circulator

Optics Letters, Vol. 39, pages 279–282 (2014)

Patrick Ehlers, Isak Silander, Junyang Wang, Aleksandra Foltynowicz, and Ove Axner

IX. On the accuracy of the assessment of molecular concentration and spectroscopic parameters by frequency modulation spectrometry and NICE-OHMS

Journal of Quantitative Spectroscopy and Radiative Transfer, Vol. 136, pages 28–44 (2014)

Junyang Wang, **Patrick Ehlers**, Isak Silander, Ove Axner

X. Doppler broadened NICE-OHMS – Optimum modulation and demodulation conditions, cavity length, and modulation order

Journal of the Optical Society of America B, Vol. 31, pages 2051–2060 (2014)

Patrick Ehlers, Isak Silander, Ove Axner

XI. NICE-OHMS beyond the triplet formalism: assessment of the optimum modulation index

Journal of the Optical Society of America B, Vol. 31, pages 1499–1507 (2014)

Patrick Ehlers, Junyang Wang, Isak Silander, Ove Axner

XII. On the use of etalon-immune-distances to reduce the influence of background signals in frequency modulation spectroscopy and noise-immune cavity-enhanced optical heterodyne molecular spectrometry

Journal of the Optical Society of America B (submitted in 2014)

Patrick Ehlers, Alexandra Johansson, Isak Silander, Aleksandra Foltynowicz, Ove Axner

XIII. Noise-immune cavity-enhanced analytical atomic spectrometry – NICE-AAS – a technique for detection of elements down to zeptogram amounts

Spectrochimica Acta B (accepted for publication in 2014)

Ove Axner, **Patrick Ehlers**, Thomas Hausmaninger, Isak Silander, and Weiguang Ma

Contents

Sammanfattning v

Abstract vii

List of Publications ix

---

1 Introduction and Background 1

2 Absorption and Dispersion Spectroscopy 7
2.1 Interaction of light and molecules 7
2.1.1 Lambert-Beer law 7
2.1.2 Attenuation and phase shift of the electrical field 9
2.2 Broadening mechanisms and line shapes 9
2.2.1 Voigt line shape function 10
2.2.2 Line shape effects beyond the Voigt formalism 11

3 Frequency Modulation Spectroscopy 13
3.1 FMS signal for arbitrary modulation index 14
3.2 Analytical FMS signal 16
3.3 Background signals in FMS 16
3.3.1 Origins of background signals 16
3.3.2 Background signals from RAM and means to reduce such 17
3.3.3 Background signals from etalons and the concept of etalon-immune-distances as a means to reduce such . 18

4 Optical Resonators **21**
4.1 Optical path length enhancement 21
4.2 Spatial mode matching 24
4.2.1 Gaussian beams 24
4.2.2 Spatial incoupling of a Gaussian beam into a resonator 25

5 Laser Frequency Stabilization **29**
5.1 Background 29
5.2 Pound-Drever-Hall error signal 31
5.3 Feedback design 32

6 NICE-OHMS **35**
6.1 Principles of NICE-OHMS 35
6.2 Doppler-broadened NICE-OHMS 37
6.2.1 Doppler-broadened NICE-OHMS signals 37
6.2.2 On the design of an instrumentation 37
6.3 Sub-Doppler NICE-OHMS 41

7 Limits of Concentration Assessment **43**
7.1 Statistical tools and definitions 43
7.1.1 Classical tools 43
7.1.2 Allan deviation and Allan-Werle plots 44
7.1.3 Standard deviation vs. Allan deviation 46
7.1.4 Detection limit 47
7.2 Shot-noise – a natural limit of detection 49

8 Experimental Details **51**
8.1 Fiber-laser-based NICE-OHMS 51
8.1.1 Basic setup 51
8.1.2 A closer look at the AOM frequency control 54
8.1.3 Environmental isolation 56
8.1.4 Vacuum system 57
8.1.5 Optical cavities 58
8.1.6 Fiber-coupled optical circulator 60
8.2 DFB-laser based NICE-OHMS 61

9 Results **65**
9.1 Reduction of the laser-cavity jitter by external means 65
9.2 NICE-OHMS instrumentation based on an optical circulator . . 68
9.3 NICE-OHMS beyond the triplet formalism – optimum system realization 70
9.4 Impact of noise-immune distances on NICE-OHMS 72
9.5 DFB-laser based NICE-OHMS 74
9.6 Line shapes beyond the Voigt profile 75
9.7 Additional but yet unpublished results 77

10 Conclusion and Future Prospects **79**

Appendix – AOM frequency control servo **83**

Acknowledgements **85**

Nomenclature **87**

Bibliography **93**

Scientific Publications **103**

Comments on the publications and my contributions to them 103

I. DFB-laser-based NICE-OHMS in the pressure broadened [...] . . . 109
II. Dicke narrowing in dispersion mode and NICE-OHMS [...] 123
III. FM background signals from fiber-based EOMs [...] 137
IV. FL-NICE-OHMS instrumentation for Db-detection [...] 147
V. Speed-dependent Voigt – theory 161
VI. Speed-dependent Voigt – experiment 173
VII. NICE-OHMS – Principles and Performance 185
VIII. FL-NICE-OHMS incorporating an optical circulator 229
IX. On the accuracy of the assessment of molecular [...] 235
X. Doppler broadened NICE-OHMS – Optimum modulation [...] . . 255
XI. NICE-OHMS beyond the triplet formalism [...] 267
XII. On the use of EIDs to reduce the influence [...] 279
XIII. NICE-AAS – a technique for detection of elements [...] 291

1

Introduction and Background

Spectroscopy is the study of the interaction of electromagnetic radiation with atoms or molecules. It can be used to obtain information about the energy-level structure of these particles, the strength of chemical bonds, and their geometry. Molecular absorption spectroscopy (AS) assesses these features by measuring the absorption of light by molecules as a function of the wavelength. There are different approaches to this, incorporating both narrow line width and broadband sources, the latter in combination with either a spectrometer, spectral filters, or a dispersive element on the detection side. Almost all molecular compounds that are present in the atmosphere show moderate to strong absorption spectra in the infrared (IR) region, which is divided in the near-IR (approximately 0.7 µm to 2.5 µm), mid-IR (2.5 µm to 25 µm), and far-IR region (25 µm to 500 µm), which then goes over into the microwave range [1]. The obtained spectroscopic data constitute a unique finger-print of a molecule and can be used for identification of constituents in unknown gases, but also for quantitative assessment of particular molecule concentrations therein. While energy-level spectra of molecules comprise transitions between both electronic, vibrational and rotational states, absorption in the IR region most often originate from transitions between vibrational and rotational states and are therefore commonly referred to as vibrational-rotational transitions. The strongest vibrational transition bands arise from transitions where the vibrational quantum number changes by one unit, from the ground level to the first excited level, which are called the fundamental vibrational bands and usually have wavelengths in the mid-IR, while overtones of these bands typically reside in the near-IR region. Transitions within a band can appear very close to each other, sometimes they are separated by only a few MHz, which is why spectrometers with high spectral resolution need to be used to be able to resolve these. Favorable light sources for such spectroscopic applications are diode lasers, which in the near-IR region can be found in a large variety.

The most simple approach of laser-based spectroscopy is direct absorption spectroscopy (DAS), where light from a laser is sent through the sample contain-

ing an absorber before it is detected by a photo detector. When the wavelength is scanned across a molecular transition, the detector will show a frequency-dependent response, from which the amount of absorption can be calculated. The smallest detectable amount of absorption, $\Delta I/I_0|_{\min}$, is determined by both the strength of the signal and the amount of noise in the detector output, the latter primarily governed by $1/f$-type amplitude modulation (AM) noise from the laser and the detection system. For DAS $\Delta I/I_0|_{\min}$ typically resides in the 10^{-3} to 10^{-4} region [1, 2], which corresponds to sample concentrations down to the %–‰ range when detected in the near-IR region, and in the parts-per-million (ppm) region when detected in the mid-IR region. For many applications, such as atmospheric trace gas spectroscopy or breath analysis, this is not sensitive enough.

In general, there are three ways to lower the minimum-detectable concentration: (*i*) active reduction of $1/f$-type noise by spectroscopic modulation techniques, e.g. by wavelength modulation spectroscopy (WMS) or frequency modulation spectroscopy (FMS); (*ii*) prolongation of the interaction length between light and sample, e.g. by the implementation of a multi-pass cell or a Fabry-Pérot resonator; (*iii*) use of a spectral region in which the molecules have larger transition line strengths. Note that the latter approach will have an impact only on the lowest amount of detectable concentration, while $\Delta I/I_0|_{\min}$ is unchanged. Since this thesis is solely devoted to further development of a specific technique based on lasers emitting light in the near-IR region, the latter is not further discussed here. Thus, the first two approaches, in turn, form the basis for the technique used in this thesis, and are therefore explained in short.

In WMS the wavelength of the laser is commonly modulated in the 1 to 100 kHz range and the signal is detected at an integer multiple of the modulation frequency, i.e. at $1f$, $2f$, or $3f$, and so on. This technique is also referred to as derivative spectroscopy or harmonic detection. Since the amount of technical noise falls with $1/f$, the frequency should be chosen as large as possible, preferably at a frequency for which the $1/f$-noise is below that of other sources of noise (see below). Since the modulation introduces a disturbance to the system, sometimes the maximum modulation frequency is limited by technical reasons. Most often the detection is performed at twice the modulation frequency, i.e. at $2f$, since this is the smallest harmonic that is non-zero at resonance, has its maximum there, and has a vanishing baseline [1]. This implies that in the absence of absorbers the WMS technique is background free.

In FMS the phase of the laser is modulated at modulation frequencies reaching from tens of MHz up to a few GHz. Especially in the hundreds of MHz regime there is no longer any significant contribution of $1/f$-type noise. Light modulated in this domain can be seen as a carrier accompanied by sidebands at distances given by multiples of the modulation frequency; in the case of weak modulation, i.e. for modulation indices well below unity, the FM spectrum is given by a triplet consisting of the carrier and two sidebands. If undisturbed, the two sidebands are perfectly out-of-phase with each other and the net-signal, which is composed of the sum of two beat signals (between the carrier and each of the sidebands), vanishes. For this reason, for a balanced triplet and in the absence of absorbers, also the FMS technique is background free.

The detection sensitivity of both WMS and FMS is often hampered by technical noise, primarily by multiple reflections between various optical components, which due to interference give rise to a wavelength-dependent background. Therefore commonly achieved values of $\Delta I/I_0|_{\min}$ are of the order of 10^{-5}, limiting the techniques to detection of molecular compounds at ppm levels, when detected in the near-IR, and at parts-per-billion (ppb) levels, when detected in the mid-IR. Properly realized, due to the high modulation frequency, FMS can come near the shot-noise limit for single-pass absorption and reach detection sensitivities in the 10^{-6} region.

Optical path length enhancement, the second way to lower $\Delta I/I_0|_{\min}$, is commonly achieved by redirecting the light between two or more mirrors so as to pass the absorber volume a multitude of times. In its most simple approach, the light beam is reflected between the mirrors a given number of times before it leaves the cell again. The maximum path length of such a multi-pass cells is solely determined by the cell geometry and beam properties. Although the longest path length that, to the author's knowledge, has been achieved so far was 252 m (with a physical cell length of 55.6 cm and with 453 reflections) [3], typical path lengths of multi-pass cells are below 100 m.

The most efficient way of optical path length enhancement, though, is the use of Fabry-Pérot (FP) cavities based on mirrors with high reflectivities, mostly above 99.9%. Path lengths of several kilometers can be obtained from small resonators with lengths below a meter, which corresponds to enhancement factors of several thousands. The repeated reflection of light in a cavity gives rise to an increased intensity inside the resonator. Therefore, high intracavity powers of several Watt can easily be achieved even for low power lasers in the mW regime. A drawback with using an FP cavity for ordinary AS is though that the laser has to be locked actively to the narrow cavity modes, which often requires high-bandwidth locking electronics. The by nature finite performance of the lock introduces, especially for cavities with large mirror reflectivities, excessive frequency-to-amplitude converted noise and eventually limits the technique of direct absorption cavity-enhanced absorption spectroscopy (CEAS) to detection sensitivities in the 10^{-9} region [1].

A way around the problem of remaining laser-cavity jitter noise is given by the cavity ring-down spectroscopy (CRDS) technique. The technique measures the time it takes for the signal to decay, also referred to as the ring-down time, from which the technique got its name. From the ring-down time the amount of an analyte can be derived. Originally, CRDS experiments incorporated pulsed laser sources. Since the width of the pulses typically was larger than the FSR of the cavities, which not only gave rise to simultaneous interaction with many modes, but also to a poor uncoupling efficiency, which was deteriorating the detection sensitivities. Later, continuous wave-CRDS (cw-CRDS) and integrated cavity output spectroscopy (ICOS) have been developed. In cw-CRDS, light is first coupled into the resonator either by scanning the frequency of the laser across a cavity mode or by an active lock [1]. In both cases, the light is switched off whenever enough power was established within the cavity; at the same time, an assessment of the ring-down time of the intracavity field is triggered. Since the incident light is turned off before the assessment of the ring-down times, the

technique is not affected by any frequency-to-amplitude noise conversion. In ICOS, which is another variant of CRDS, time-integrated ring-down events are recorded [1] while scanning the laser back-and-forth across one or several cavity resonances. This is in contrast to cw-CRDS, where single ring-down events are measured. Typically the incident beam is aligned slightly off the cavity-axis to evoke a number of higher-order transverse modes, which is referred to as off-axis (OA)-ICOS. The main limitation of both cw-CRDS and OA-ICOS is the low amount of light that can be coupled in narrow resonator modes. Despite this, cw-CRDS and ICOS detection sensitivities are typically in the order of 10^{-10}. The former of the techniques is the most commonly used CE-technique.

A technique that copes with the frequency-to-amplitude noise conversion (instead of avoiding it as it is the case with CRDS) is noise-immune cavity-enhanced optical-heterodyne molecular spectroscopy (NICE-OHMS). In a unique approach this technique combines the concepts of frequency modulation for active reduction of $1/f$ noise with cavity enhancement for prolongation of the interaction length [4]. By locking the modulation frequency to the free-spectral range (FSR) of the cavity, all FM-modes are able to enter the resonator, thereby allowing for FMS inside the cavity. If properly locked, all modes of the FM-spectrum are additionally affected in the same way by the cavity modes. This implies that the effect of frequency-to-amplitude noise conversion cancels in the detection, which provides the technique with an immunity against this type of noise. The technique gives access to both Doppler-broadened (Db) and, due to the presence of counter-propagating waves in the cavity, sub-Doppler (sD) signals. As an FM technique, these signals can be detected at both absorption and dispersion phase, as well as at any phase there in between, which provides information about both the attenuation and the phase shift the light experiences from a transition.

The technique was originally developed in the 1990s by John Hall, Jun Ye, and Long-Sheng Ma at JILA, Boulder, CO, USA, for frequency standard applications [5–7] based on a narrow line width Nd:YAG laser and a cavity with a finesse of around 10^5. This instrumentation was capable to detect a relative absorption of 5×10^{-13} ($1 \times 10^{-14}\,\mathrm{cm^{-1}Hz^{-1/2}}$) for sD detection of C_2HD at 1064 nm. Containing this great potential, the technique was during the following years developed for a variety of applications covering all above mentioned detection modes and a large number of molecules. Examples are sD spectroscopy of overtone bands in CH_4 [8] and CH_3I [9], an assessment of weak magnetic dipole moments of O_2 by Db detection [10], Db detection of the sixth overtone band of NO [11,12], Db detection of ultra weak transitions in the visible region of molecular oxygen [13, 14], Db assessments of CH_4 [15] and the HO_2 radical [16], fast molecular ion beam velocity modulation spectroscopy [17–20], and others [5–7, 21–28]. Figure 1.1 shows a summary of past and ongoing activities in the NICE-OHMS field, the number of currently published scientific publications in the field, as well as an overview of molecules that have been addressed. Even though there was an early attempt in 2004 to widen the spectral range of NICE-OHMS into the mid-IR region by the use of a quantum-cascade laser (QCL) for sD detection of N_2O [29], the technique has so far, due to access to instrumentation and devices from the telecom-sector in the

near-IR, primarily been developed around tunable lasers in this wavelength region. Since the line width of tunable lasers most often markedly exceeds that of a fixed-frequency solid-state lasers, the sensitivity of all realizations of NICE-OHMS based on tunable lasers has been inferior when compared to that of the original demonstration. As the laser line width in most cases is larger than the narrow modes of the incorporated cavities, the biggest challenges, and often the limiting factor throughout all realizations, has been the requirement of a tight laser-cavity lock.

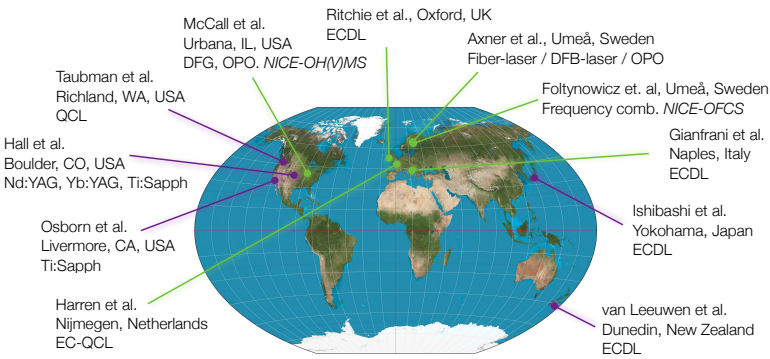

Research groups with ongoing and past NICE-OHMS activities around the world, indicated in green and purple color, respectively, together with the employed laser system.

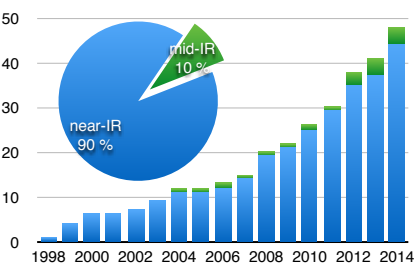

Accumulated total number of publications in the NICE-OHMS field by year, where blue and green color indicate publications based on works targeting the near-IR and mid-IR region, respectively. The pie chart shows the distribution of the publications by 2014.

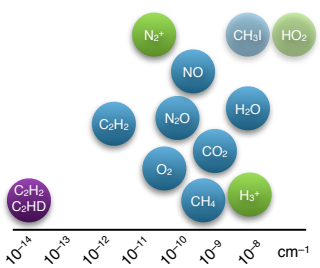

Molecules detected by NICE-OHMS and detection sensitivity of the corresponding setup (no numbers were available for CH_3I and HO_2). Purple: first demonstration based on a fixed-frequency laser.

Figure 1.1: NICE-OHMS activity at a glance. The activities indicated in the world-map [30] correspond to publications performed by the following senior scientists: Hall et al., Refs. [6,7,21,31]; Gianfrani et al., Refs. [10,25]; Ishibashi et al., Refs. [8,9]; Osborn et al., Refs. [11,12]; Taubmann et al., Ref. [29]; van Leeuwen et al., Refs. [13–16]; Axner et al., Refs. [4,32–52]; Ritchie et al., Refs. [15,16]; McCall et al., Refs. [17–20,53–55]; Foltynowicz et al., Ref. [56]; Harren et al., Ref. [57]. Beside the references above, this figure is based on information given in Ref. [58].

In 2007 fiber-laser-based (FL) NICE-OHMS was realized as the so far most successful approach incorporating a tunable laser [32], based upon a narrow line width erbium-doped distributed-feedback-laser pumped fiber-laser (EDFL) with

a free-running line width of only 1 kHz over 100 µs. In the following years, a large number of studies were performed on this instrumentation [32–40, 43]. By the time when the work this thesis is based on was commenced, a white-noise limited absorption sensitivity of $1.8 \times 10^{-11}\,\mathrm{cm^{-1}Hz^{-1/2}}$ was demonstrated for integration times up to around a minute. This detection sensitivity was the so far lowest reported (based on an instrument around a tunable diode laser) and primarily limited by noise arising from the remaining laser-cavity jitter and both drifts and vibrations in the optical system.

The main focus of this thesis work was on the further development of FL-NICE-OHMS with respect to improved performance, primarily better stability, lower noise levels, reduction of physical size, and general system design, see **publications III, IV, VIII, X, XI** and **XII** [44–46, 48–50]. In addition, as a spin-off of FL-NICE-OHMS, in order to widen the range of applicability and to allow for assessment of molecular and gaseous parameters from NICE-OHMS signals in the collisional broadened regime, a system around a distributed-feedback (DFB) laser was realized (see **publication I** [41]); a number of line shape studies were performed on this system, which are presented in **publications II, V, VI,** and **IX** [41, 42, 47, 51, 52]. Moreover, the thesis includes an extensive review of FL- and DFB-NICE-OHMS in **publication VII** [4]. A final **publication, XIII,** deals with the ability to perform noise-immune cavity-enhanced analytical absorption spectrometry on atomic elements, referred to as NICE-AAS.

The intention of this thesis is not to give consistent derivations of theoretical expressions that often are used with the technique. These can instead be found in earlier works or standard textbooks (see for example Refs. [59, 60] for laser physics and spectroscopy in general and Refs. [26, 31] for NICE-OHMS in particular). It instead provides a short summary of the basic properties and features of the technique and focuses on the author's contribution to the field. The outline therefore is as follows: in chapter 2 some of the most important spectroscopic basics for this work are explained; chapter 3, 4, and 5 describe the building bricks of NICE-OHMS, i.e. frequency modulation, cavity-enhancement, and laser frequency control, respectively. In chapter 6, these are assembled and the NICE-OHMS technique is presented in detail. The most common limitations for the detection sensitivity and tools for their assessment are outlined in chapter 7. The experimental details of FL-NICE-OHMS and to some extent DFB-NICE-OHMS are described in chapter 8, before the most important results are presented in chapter 9. A summary, as well as a silhouette of future prospects, are given in chapter 10, which finally is followed by a collection of the scientific publications this thesis work is based on.

2 Absorption and Dispersion Spectroscopy

2.1 Interaction of light and molecules

2.1.1 Lambert-Beer law

Light that passes a volume containing a molecular absorber (Fig. 2.1) will be attenuated whenever the frequency of the light is in resonance with a transition of the molecule. For the case when the light is not affecting the absorber, but solely probing it, the intensity, I, after a given interaction length, L, is given by the Lambert-Beer-law, i.e.

$$I(\nu_{\mathrm{d}}) = I_0 \, \mathrm{e}^{-\alpha(\nu_{\mathrm{d}})L}, \tag{2.1}$$

where I_0 is the incoming intensity ($\mathrm{W/m^2}$), and α the so-called absorption coefficient[1] ($1/[L]$), where $[L]$ represents the units of L. For a transition with integrated molecular line strength, $\hat{S}$ [in $\mathrm{cm^{-1}/(molecule\ cm^{-2})}$], and a number density of molecules, n_{A} (i.e. the number of molecules per unit volume), the

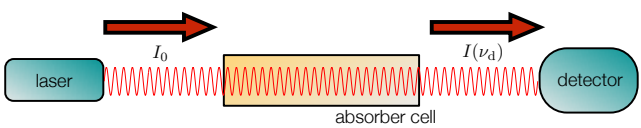

Figure 2.1: Principle of direct absorption spectroscopy (DAS). Laser light with incident intensity, I_0, will be attenuated due to the frequency-dependent interaction with a molecular absorber.

[1] In many works the absorption coefficient is defined as the product of the frequency-dependent transition cross section, $\sigma(\nu_{\mathrm{d}})$, and the number density of molecules, n_{A}. As stated in the work of Fried and Richter [1], the cross section can conveniently be related to expressions containing the molecular line strength, which commonly is tabulated in databases such as "HITRAN" [61].

absorption coefficient can be written as [1, 61]

$$\alpha(\nu_\mathrm{d}) = \hat{S} n_\mathrm{A} \chi^\mathrm{abs}(\nu_\mathrm{d}), \tag{2.2}$$

with χ^abs being the area-normalized absorption line shape function. The difference between the frequency of the light, ν, and the center frequency of the transition, ν_0, i.e. $\nu - \nu_0$, is called the frequency detuning, ν_d. A common quantity in this context is the relative absorption, $\Delta I/I_0$, which is given by

$$\frac{\Delta I(\nu_\mathrm{d})}{I_0} = \frac{I_0 - I(\nu_\mathrm{d})}{I_0} = 1 - \mathrm{e}^{-\alpha(\nu_\mathrm{d})L} \approx \alpha(\nu_\mathrm{d})L, \tag{2.3}$$

where the approximation in the last step is valid in the case of small absorption, for which the exponential function in Eq. (2.1) can be expanded as $\exp[-\alpha(\nu_\mathrm{d})L] \approx 1 - \alpha(\nu_\mathrm{d})L$. For practical work, it is often convenient to express the absorption coefficient in term of the relative molecular concentration, c_rel, and the total gas pressure, p, as [1, 26]

$$\alpha(\nu_\mathrm{d}) = S c_\mathrm{rel} p \chi^\mathrm{abs}(\nu_\mathrm{d}), \tag{2.4}$$

where S is the molecular line strength ($\mathrm{cm}^{-2}/[\mathrm{p}]$), which, for a given temperature, T_exp, is related to the integrated molecular line strength, $\hat{S}$, through [61]

$$\hat{S} = \frac{S p_\mathrm{atm} T_\mathrm{exp}}{T_0 n_0}, \tag{2.5}$$

where, in turn, n_0 is the Loschmidt constant, which for $T_0 = 273.15\,\mathrm{K}$ and atmospheric pressure, p_atm, is equal to $2.686\,780\,5(24) \times 10^{25}\,\mathrm{molecules/m^3}$. Another useful quantity is the on-resonance absorption coefficient, i.e. the absorption coefficient for zero detuning from the transition center, α_0, which can be written in either of the forms [26]

$$\alpha_0 = \hat{S} n_\mathrm{A} \chi_0 = S c_\mathrm{rel} p \chi_0, \tag{2.6}$$

where χ_0 is the peak-value of χ^abs. The absorption coefficient can therefore also be expressed in terms of a peak-normalized absorption line shape function, $\bar{\chi}^\mathrm{abs}$, as

$$\alpha(\nu_\mathrm{d}) = \alpha_0 \bar{\chi}^\mathrm{abs}(\nu_\mathrm{d}). \tag{2.7}$$

Info

Depending on the scientific field, there are three commonly used quantities to express frequencies: (*i*) the wavelength, λ (in units of length), (*ii*) the frequency itself, ν, given by c/λ (in units of Hz), where c is the speed of light, (*iii*) the wave number, $\bar{\nu} \equiv 1/\lambda$ (in units of cm^{-1}) [1]. A wavelength of 1500 nm corresponds to 1.5 µm, $6667\,\mathrm{cm}^{-1}$ or 200 THz. In the same wavelength range, a detuning of 1 GHz corresponds to $0.033\,\mathrm{cm}^{-1}$ or 7.5 pm.

2.1.2 Attenuation and phase shift of the electrical field

When light passes a molecular medium, the electric field of the light will both be attenuated and phase shifted. As has been in shown in [26] and [34], the transmitted complex electrical field, $\tilde{E}^{\mathrm{A}}$, i.e. the field after having passed an absorber over an interaction length, L, can be related to the undisturbed complex electrical field, $\tilde{E}$, according to

$$\tilde{E}^{\mathrm{A}}(\nu_{\mathrm{d}}, L, t) = \tilde{T}^{\mathrm{A}}(\nu_{\mathrm{d}})\tilde{E}(\nu_{\mathrm{d}}, L, t), \tag{2.8}$$

where $\tilde{T}^{\mathrm{A}}$ is the complex transmission function of the absorber, given by

$$\tilde{T}^{\mathrm{A}}(\nu_{\mathrm{d}}) = \mathrm{e}^{-\delta^{\mathrm{A}}(\nu_{\mathrm{d}}) - \mathrm{i}\,\phi^{\mathrm{A}}(\nu_{\mathrm{d}})}, \tag{2.9}$$

where δ^{A} and ϕ^{A} are the attenuation and the phase-shift of the electrical field due to the absorber, respectively. The latter two can be related to the area-normalized absorption line shape function, χ^{abs}, and its dispersion counterpart, χ^{disp}, respectively, according to [4, 34]

$$\delta^{\mathrm{A}}(\nu_{\mathrm{d}}, G) = \frac{Sc_{\mathrm{rel}}pL}{2}\chi^{\mathrm{abs}}(\nu_{\mathrm{d}}, G) \tag{2.10}$$

and

$$\phi^{\mathrm{A}}(\nu_{\mathrm{d}}, G) = \frac{Sc_{\mathrm{rel}}pL}{2}\chi^{\mathrm{disp}}(\nu_{\mathrm{d}}, G), \tag{2.11}$$

where G the degree of optical saturation.

2.2 Broadening mechanisms and line shapes

A molecular transition between two energy-levels has a center frequency that is given by the difference of the energy-levels involved. The finite lifetime of the transition gives rise to an uncertainty of this frequency and translates directly into a Lorentzian frequency distribution [59, 60] around the center frequency of the transition. This effect is called natural line broadening. For most practical cases when molecules are to be probed with light, however, the natural broadening is entirely clouded by primarily two other broadening mechanism, namely Doppler broadening and collisional broadening.

Doppler broadening accounts for the fact that the frequency of the light as seen by the molecule depends, due to the Doppler effect, on its velocity vector: molecules traveling in the same direction as the one in which the light propagates will experience a red-shift of the frequency, while the ones traveling towards the light will experience a blue-shift. Since the directions of the velocity-vectors of molecules in an ideal gas have a Gaussian distribution (if projected onto the dimension along which the light propagates), Doppler broadening will give rise to a Gaussian profile shape, as well. An important spectroscopic quantity is the width of the Doppler profile, also called the half-width at half-maximum (HWHM) Doppler width, Γ_{D}, which, for a given temperature, T (in K), and molecular mass, m (in kg), is given by [59]

$$\Gamma_{\mathrm{D}} = \frac{\nu_0}{c}\sqrt{\frac{2\ln(2)k_{\mathrm{B}}T}{m}} \approx 1.07 \times 10^{-4}\frac{1}{\lambda_0}\sqrt{\frac{T}{M}}\mathrm{MHz}, \tag{2.12}$$

where c is the speed of light (m/s) and k_B is the Boltzmann constant, given by 1.380×10^{-23} J/K. In the last step, M is the molecular mass of the molecule (in u) and λ_0 the wavelength of the light (m).

Collisional broadening, sometimes also referred to pressure broadening, accounts for the fact that absorption processes are interrupted by collisions with other molecules [60]. The effective lifetime of a transition thereby becomes shortened, giving rise to a larger energy-level uncertainty and thereby a broadening of the Lorentzian frequency spectrum. The larger the amount of molecules per unit volume and the faster the molecules move (the higher the temperature), the more dominant this effect becomes (since the collision rate becomes larger [59]). Since the number of molecules in a volume and their velocity are proportional to the pressure of a gas, it is clear that the collisional broadening becomes stronger as the pressure increases. The collisional width of a transition, i.e. the HWHM of the Lorentzian profile, Γ_L, is therefore often conveniently written as the product of a pressure broadening coefficient, B_p (e.g. in MHz/Torr), and the pressure of the gas sample, p (in Torr), i.e. as [59]

$$\Gamma_L = B_p p. \tag{2.13}$$

Example

For an illustration of how the two broadening mechanisms contribute to the line width, consider a transition of acetylene (C_2H_2, with a molecular mass of 26 u) in the near-infrared region at 1.5 μm, which at room temperature (296 K) has a Doppler width of 240 MHz, while carbon dioxide (CO_2, with a molecular mass of 44 u) has a width of only 180 MHz due to the larger mass of the molecule. For the former, assuming a typical pressure broadening coefficient $B_p = 3.5$ MHz/Torr, the Lorentzian width becomes 1% of the Doppler width already at around 0.7 Torr $\approx 9 \times 10^{-4}$ atm. To yield a collisional width that exceeds the Doppler width by two orders of magnitude, the pressure would have to be increased up to around 7000 Torr or 9 atm. This implies that a transition is often affected by both collisional and Doppler broadening.

As can be seen from the example, Doppler-broadening dominates only for pressures far below an atmosphere, while collisional broadening, in turn, dominates for pressures from a few atmospheres and upwards[2]. In the intermediate regime, where both broadening mechanisms are contributing to a significant amount to the line shape, neither of the two can be neglected and they have therefore to be taken into consideration simultaneously, which, under some general conditions, can be done by the Voigt profile.

2.2.1 Voigt line shape function

The most common line shape profile in the regime where both Doppler and collisional broadening are taken into account is the Voigt profile[3]. This profile

[2] It should be noted in this context that always both broadening mechanisms are present, even though their contribution might be neglected. In this sense, pure Doppler broadening or pure collisional broadening does not exist.

[3] The Voigt profile is named after Woldemar Voigt [fo:kt] (1850–1919)

is based on the assumption that collisional broadening and Doppler broadening are uncorrelated and is therefore represented by a convolution of a Lorentzian and a Doppler line shape function. It can be written as [34]

$$\chi_{\mathrm{V}}^{\mathrm{abs}}(x, y, G) = \frac{c}{\sqrt{\pi}\Gamma'_{\mathrm{D}}} \frac{1}{\sqrt{1+G}} \mathrm{Re}\left[W(x + \mathrm{i}\, y)\right] \tag{2.14}$$

and

$$\chi_{\mathrm{V}}^{\mathrm{disp}}(x, y, G) = -\frac{c}{\sqrt{\pi}\Gamma'_{\mathrm{D}}} \mathrm{Im}\left[W(x + \mathrm{i}\, y)\right] \tag{2.15}$$

for the absorption and dispersion part, respectively, where W is the complex error function for a complex argument, x the Doppler-width normalized frequency detuning (given by $\nu_{\mathrm{d}}/\Gamma'_{\mathrm{D}}$), y the saturated Voigt parameter given by $\sqrt{1+G}\Gamma_{\mathrm{L}}/\Gamma'_{\mathrm{D}}$, G the degree of saturation, given in Eqs. (20)-(22) in Ref. [34], and where finally Γ'_{D} is given by $\Gamma_{\mathrm{D}}/[\ln(2)]^{1/2}$.

Example

This example shows, by the left plot, a comparison of three area normalized absorption profiles and, by the right plot, their dispersion counterparts. The Doppler, Lorentzian, and Voigt profile for a transition at 1.5 µm with a HWHM Doppler-width of 236 MHz and an equally large Lorentzian width are illustrated in black, red, and blue color, respectively.

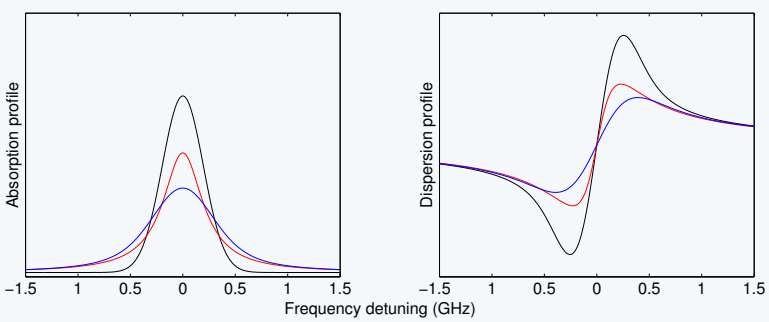

2.2.2 Line shape effects beyond the Voigt formalism

For many spectroscopic applications the Voigt profile is an adequate description of line shapes in the intermediate pressure regime, i.e. when both Doppler and collisional broadening are present. However, when spectroscopic line parameters or analyte concentrations are to be determined with high precision, it is not accurate enough, since it neglects both the effect of Dicke narrowing, as well as speed-dependent effects. Both effects narrow the line profile and are well known for the absorption line shapes, but up to recently there were no descriptions for their dispersion counterparts. Since NICE-OHMS as a FMS technique also gives rise to dispersion signals, such descriptions had to be derived. Examples of

such are shown in **publication II** and **VI**. In the following, the both narrowing mechanisms are described on a phenomenological basis.

Dicke narrowing

A molecule in a gas sample travels with a certain velocity, i.e. with a specific speed in a given direction, until it collides with another molecule in the gas volume. The average distance between two successive collisions is called the mean free path, $\bar{\Lambda}$. After a collision, the molecule under consideration will change its velocity. This fact gives rise to a narrowing of the Doppler profile [42], since the molecules have an averaged speed that is smaller than the thermal speed that is assumed in the Doppler profile when collisions are taken into account. Since photons of light with wavelength, λ, can be assigned a momentum, p_λ, given by h/λ, where h is the Planck constant, the smallest displacement information, Δx, that a photon can resolve, is given by the uncertainty relation $\Delta x \Delta p \leq h/2\pi$, and is equal to $\lambda/2\pi$. For small collision rates, for which $\bar{\Lambda} \gg \lambda/2\pi$, the molecules can be supposed to be undisturbed and the Doppler profile is maintained. If, however, the collision rates are so large that $\bar{\Lambda} \lesssim \lambda/2\pi$, the mean velocity of the molecules will be reduced, which yields a narrowed Doppler profile. This phenomenon is called Dicke narrowing and was mentioned for the first time by Dicke in 1953 [62]. This means that collisions do not only give rise to an increased Lorentzian width of the Voigt profile, but simultaneously also to a decreased Doppler width. The two most common models for this effect are the Galatry [63] and Rautian model [64], considering soft collisions (strong correlation between the velocity before and after the collision) and hard collisions (the molecule has no memory of their velocity before the collision), respectively. A detailed discussion of this can be found in the literature, e.g. in Refs. [4, 27, 42].

Speed-dependent effects

As was alluded to above, the conventional Voigt profile constitute a convolution of a Doppler profile with a velocity-shifted Lorentzian profile, with the latter being assumed constant for all velocity groups. However, due to the fact that the relaxation rate of the molecules has a velocity dependence, different velocity groups do not have the same Lorentzian width [51, 65], whereby the Lorentzian profile becomes velocity-dependent through the weighting with a Maxwell-Boltzmann distribution, where the effect is stronger for larger velocities. This gives rise to a narrowing of the Lorentzian profile and is referred to as speed-dependent effects (SDEs) [4, 27, 51, 52]. The most common model that accounts for SDEs is the so-called speed-dependent Voigt (SDV) profile presented in [51], originally suggested by Rohart et al. in 1994 [66] and later demonstrated by Boone et al. [67, 68].

3

Frequency Modulation Spectroscopy

Frequency modulation (FM) is a modulation technique for reduction of noise and frequency stabilization in laser spectroscopic techniques and applications that has been around since the early 1980s. Pioneers in the development and utilization of the technique were Gary C. Bjorklund, John L. Hall, Edward A. Whittaker, and Ronald Drever, to name a few [69–73]. Laser spectroscopists became soon thereafter aware of the large potential this technique holds.

In FM the phase of the light – and not the frequency, as the name suggests – is modulated at a high frequency, typically in the radio frequency domain. This causes sidebands to appear that are interfering with the carrier, which gives rise to beat notes at the modulation frequency. Since the odd order sidebands (1st, 3rd, etc.) are out of phase, the beat notes cancel each other, wherefore there is no FM signal in the absence of absorbers. The presence of an absorber, however, will affect the perfect balance between the sidebands, creating a modulation of the power at integer multiples of the modulation frequency. This beat-signal can be detected and demodulated, which, as is illustrated in Fig. 3.1, can

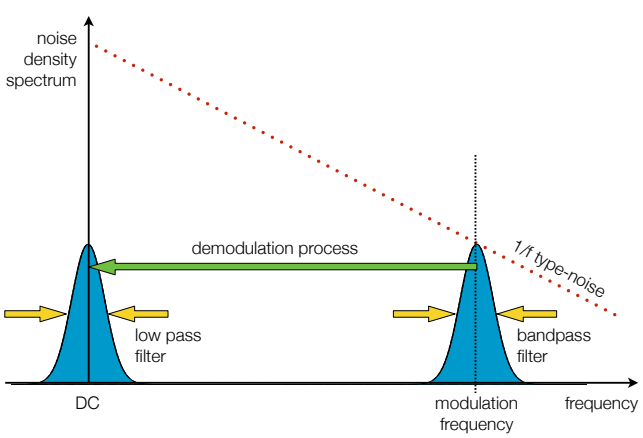

Figure 3.1: Principle of the FMS technique. The green arrow indicates the downshift of the signal spectrum (blue area) around the modulation frequency to DC. The red line indicates the $1/f$-noise-contribution. See text for details.

be seen as a down-shift of the signal spectrum (the blue area to the right in the Figure) by the demodulation process, indicated by the green arrow. The $1/f$-noise density (the red dotted line) at the modulation frequency is significantly smaller than it is at low frequencies, wherefore the FM technique can be seen as an active reduction of this type of noise. Moreover, since the entire signal spectrum is shifted by the demodulation process, it becomes clear that a bandpass filter around the modulation frequency has the same impact as a lowpass filter (indicated by the yellow arrows).

3.1 FMS signal for arbitrary modulation index

A typical FM setup is shown in Fig. 3.2. The laser frequency is modulated either directly or by external means before the light passes a cell containing an absorber, which, if in resonance with one of the modes of the FM spectrum, distorts the balance, giving rise to a beat-note that can be detected with a photodetector and demodulated with a phase-adjustable reference signal from the local oscillator. Depending on the setting of the detection phase, either absorption or dispersion signals can be obtained, corresponding to the attenuation and phase shift of the electrical field, respectively, as well as any combination of them.

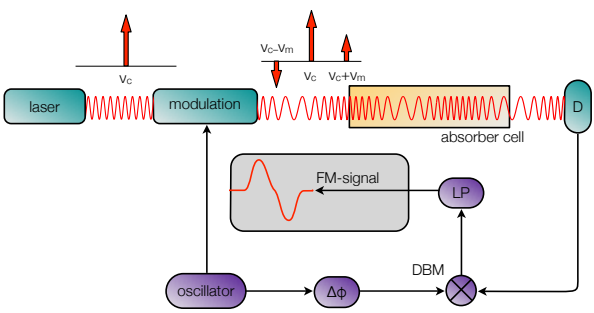

Figure 3.2: Frequency modulation setup. Light is modulated either by modulating the laser frequency directly or by external means. Beside the carrier frequency sidebands spaced from the carrier by integer multiples of the modulation frequency, which is indicated by the mode triplet for the case of moderate modulation indices. The modes will give rise to beat-notes at the modulation frequency that can be received by fast photo detectors. The FM signal is eventually demodulated with a reference signal from the local oscillator.

For a quantification of the concept, it is convenient to write the electrical field of the frequency modulated (fm) light as [69, 71]

$$E(\nu_\mathrm{c}, t) = \tilde{E}(\nu_\mathrm{c}, t) + \tilde{E}^*(\nu_\mathrm{c}, t), \tag{3.1}$$

with

$$\tilde{E}(\nu_\mathrm{c}, t) = \hat{\epsilon}\frac{E_0}{2}\,\mathrm{e}^{-2\pi\,\mathrm{i}\,\nu_\mathrm{c} t}\,\mathrm{e}^{-\,\mathrm{i}\,\beta\sin(2\pi\nu_\mathrm{m} t)}, \tag{3.2}$$

where $\hat{\epsilon}$ is a unity vector indicating the direction of the electrical field, E_0 its magnitude, β the modulation index, ν_c the frequency of the carrier, ν_m the

modulation frequency, t the time elapsed, and the star indicates the complex conjugate. Using the Jacoby-Anger expansion [74], this expression can be written as

$$\tilde{E}(\nu_{\rm c},t)=\hat{\epsilon}\frac{E_0}{2}\,{\rm e}^{-2\pi\,{\rm i}\,\nu_{\rm c}t}\sum_{k=-\infty}^{+\infty}T_k^{\rm A}(\nu_{\rm c})J_k(\beta)\,{\rm e}^{-2\pi\,{\rm i}\,k\nu_{\rm m}t}, \tag{3.3}$$

where J_k is the $k^{\rm th}$ order Bessel function and $T_k^{\rm A}(\nu_{\rm c})=\exp[-\delta_k^{\rm A}(\nu_{\rm c})-{\rm i}\,\phi_k^{\rm A}(\nu_{\rm c})]$ is the transmission function of an absorber causing a field attenuation $\delta_k^{\rm A}$ and phase shift $\phi_k^{\rm A}$ at the frequency $\nu_k=\nu_{\rm c}+k\nu_{\rm m}$ [34]. The output of the photodetector will be proportional to the intensity of the incident light, i.e.

$$I(\nu_{\rm c},t)=c\epsilon_0\langle[E(\nu_{\rm c},t)]^2\rangle=2c\epsilon_0\tilde{E}(\nu_{\rm c},t)\tilde{E}^*(\nu_{\rm c},t), \tag{3.4}$$

where the angled brackets indicate the time average over the fast components $\mathcal{O}(\nu_{\rm c})$ of the field. The last expression follows from the fact that all rapidly oscillating terms are averaged out [59]. Inserting Eq. (3.2) into the above expression yields for the intensity of light transmitted through an absorber

$$I(\nu_{\rm d},t)=I_0\left[\sum_{p=-\infty}^{+\infty}T_p^{\rm A}(\nu_{\rm d})J_p(\beta)\,{\rm e}^{-2\pi\,{\rm i}\,p\nu_{\rm m}t}\right]\left[\sum_{q=-\infty}^{+\infty}T_q^{\rm A*}(\nu_{\rm d})J_q(\beta)\,{\rm e}^{2\pi\,{\rm i}\,q\nu_{\rm m}t}\right], \tag{3.5}$$

where $\nu_{\rm d}$ is the frequency detuning from resonance given by $\nu_{\rm d}=\nu_{\rm c}-\nu_0$, with ν_0 being the absorber resonance frequency, and where $I_0\equiv c\epsilon_0E_0^2/2$.

Taking into account (i) that the detector signal is demodulated and detected at $\nu_{\rm m}$ so that only terms oscillating at this frequency contribute to the signal and (ii) that both $|\delta_k^{\rm A}-\delta_{k+1}^{\rm A}|\ll 1$ and $|\phi_k^{\rm A}-\phi_{k+1}^{\rm A}|\ll 1\ \forall k$, the transmitted intensity can be written as

$$\begin{aligned}I(\nu_{\rm d},t)|_{\nu_{\rm m}} &= 2I_0\,{\rm e}^{2\delta_0^{\rm A}}\sum_{k=0}^{+\infty}J_kJ_{k+1}\left[\left(\delta_{-k-1}^{\rm A}+\delta_{-k}^{\rm A}-\delta_k^{\rm A}-\delta_{k+1}^{\rm A}\right)\cos(\nu_{\rm m}t)\right]\\ &\quad+\left[\left(\phi_{-k-1}^{\rm A}-\phi_{-k}^{\rm A}-\phi_k^{\rm A}+\phi_{k+1}^{\rm A}\right)\sin(\nu_{\rm m}t)\right],\end{aligned} \tag{3.6}$$

where $\delta_k^{\rm A}\equiv\delta_k^{\rm A}(\nu_{\rm d})$ and $\phi_k^{\rm A}\equiv\phi_k^{\rm A}(\nu_{\rm d})$.

The FM signal is eventually obtained by demodulating the detector output with a reference signal from the local oscillator, delayed a given phase, $\theta_{\rm fm}$, with respect to the modulation, yielding, and extracting the DC component, which gives

$$\begin{aligned}S_{\rm fm}^{\rm T}(\nu_{\rm d},\theta_{\rm fm}) &= \eta_{\rm fm}P_0\,{\rm e}^{2\delta_0^{\rm A}}\sum_{k=0}^{+\infty}J_kJ_{k+1}\left[\left(\delta_{-k-1}^{\rm A}+\delta_{-k}^{\rm A}-\delta_k^{\rm A}-\delta_{k+1}^{\rm A}\right)\sin(\theta_{\rm fm})\right]\\ &\quad+\left[\left(\phi_{-k-1}^{\rm A}-\phi_{-k}^{\rm A}-\phi_k^{\rm A}+\phi_{k+1}^{\rm A}\right)\cos(\theta_{\rm fm})\right],\end{aligned} \tag{3.7}$$

where P_0 is the incident power of the detector (W) and $\eta_{\rm fm}$ is an instrumentation factor (V/W) accounting for both detector responsivity and amplification of

the signal. For modulation indices well below unity, for which the contribution from second and higher order sidebands can be neglected, Eq. (3.7) simplifies to

$$\begin{aligned} S^{\mathrm{T}}_{\mathrm{fm}}(\nu_{\mathrm{d}},\theta_{\mathrm{fm}}) &= \eta_{\mathrm{fm}} P_0 J_0 J_1 \, \mathrm{e}^{2\delta^{\mathrm{A}}_0} \left\{ \left[\left(\delta^{\mathrm{A}}_{-1} - \delta^{\mathrm{A}}_{1}\right) \sin(\theta_{\mathrm{fm}}) \right] \right. \\ &\quad \left. + \left[\left(\phi^{\mathrm{A}}_{-1} - 2\phi^{\mathrm{A}}_{0} + \phi^{\mathrm{A}}_{1}\right) \cos(\theta_{\mathrm{fm}}) \right] \right\}, \end{aligned} \tag{3.8}$$

which is equal to the well known formula describing an FM triplet.

3.2 Analytical FMS signal

In the presence of an analyte, the expressions for the attenuation, $\delta^{\mathrm{A}}(\nu_{\mathrm{d}})$, and phase shift, $\phi^{\mathrm{A}}(\nu_{\mathrm{d}})$, of the modes can be related to absorption and dispersion line profiles, $\chi^{\mathrm{abs}}(\nu_{\mathrm{d}}, G)$ and $\chi^{\mathrm{dips}}(\nu_{\mathrm{d}}, G)$, by the Eqs. (2.10) and (2.11), respectively. Figure 3.3 shows examples of some typical FM line profiles from a transition in the Doppler limit with an arbitrarily chosen, but fixed, Doppler width of $0.62\nu_{\mathrm{m}}$, for a set of three different modulation indices, β, namely 0.4 (solid), 1.0 (dashed), and 5.0 (dotted). It can be seen from the figure that the signal for $\beta = 1.0$ is the largest in this set (see also the discussion in chapter 6.2.2), while it is only marginally broader than the one for $\beta = 0.4$. Modulation indices significantly larger than unity, in turn, do primarily broaden the signal as higher order sidebands start to contribute, while the signal size drops, as can be seen from the signal for the case with $\beta = 5.0$. The dependence of the FM signal on the modulation index is studied in some detail in **publications X** and **XI** and is further discussed in chapter 6.2.2 below.

3.3 Background signals in FMS

3.3.1 Origins of background signals

In principle, in the absence of structured absorbers the FMS technique (and thereby also NICE-OHMS) should be background free, as can easily be seen form the Eqs. (3.7) and (3.8), i.e. when $\delta^{\mathrm{A}}_{-1} = \delta^{\mathrm{A}}_{+1}$, and when $\delta^{\mathrm{A}}_{-1} = \delta^{\mathrm{A}}_{0} = \delta^{\mathrm{A}}_{+1}$. However, as soon as there is a structure in the transmission the balance of the FM mode spectrum becomes disturbed and optical background signals appear. Whenever these structures come from the optical system, the signals are present also in the absence of absorbers, and they are called background signals. These background signals can have a variety of sources [4]. The most important ones are residual amplitude modulation (RAM), background signals from birefringent components, and those arising from multiple reflections between optical surfaces, so called etalons. Common to all of them is the fact that they cause a distortion of the balance of the FM mode spectrum, thereby introducing an offset in the FM signal through which low frequency noise and drifts can couple. The effects of background signals are manifold and they can have an impact onto the entire frequency spectrum of the signal, e.g. deteriorating its quality and causing either long-term disturbances (drifts), intermediate disturbances (flicker noise), or short-term disturbances (noise), all of them hampering the detection sensitivity

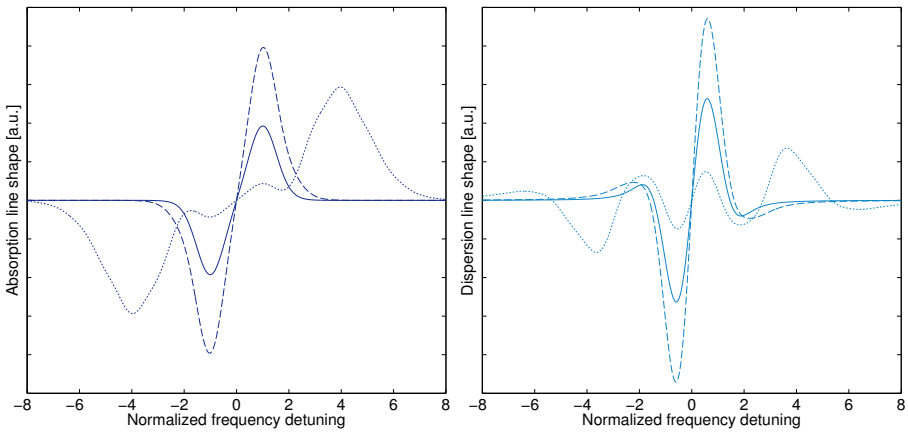

Figure 3.3: FM signals for absorption (left panel) and dispersion signals (right panel) as a function of modulation-frequency-normalized frequency detuning from mode-center, i.e. $\nu_{\mathrm{d}}/\nu_{\mathrm{m}}$. See text for details.

of the technique in one way or another. While noise can be reduced by either stabilization schemes (e.g. improved intensity-noise elimination), drifts can be tackled in two ways, either by eliminating or by stabilizing the source of the drift, i.e. "freezing" the background. In the case of periodical drifts, e.g. as can appear from etalons, it is also possible to dither one of the optical components at a fast frequency; if the dither amplitude is sufficiently large (several FSRs of the etalon), the effect of the etalon is averaged out.

3.3.2 Background signals from RAM and means to reduce such

RAM is originally defined as the accompanying modulation of the intensity that arises in some lasers when the laser frequency is modulated. The contribution of RAM to background signals can be significantly reduced by instead modulating the frequency by external means, most often by the implementation of electro-optic modulators (EOMs) [4, 75]. However, unfortunately, the use of an EOM can, in turn, also give rise to background signals. One such cause is the fact that although both the extraordinary (e) and the ordinary (o) axis impose a phase shift of the incoming light, they give rise to dissimilar amounts. Moreover, the modulation takes only place along the e-axis of the crystal in the EOM, while the o-axis remains unmodulated. Any slight deviation of the direction of polarization of the incoming light from the e-axis will therefore cause an unbalance of the triplet, which, in turn, gives rise to a background signal. The use of polarization maintaing (PM) fibers is yet another source of background signals. As is shown in **publication III** [44], which has served as a basis for the work performed in Ref. [43], in which background signals were minimized by active feedback of a reference signal (taken at a monitor point in front of

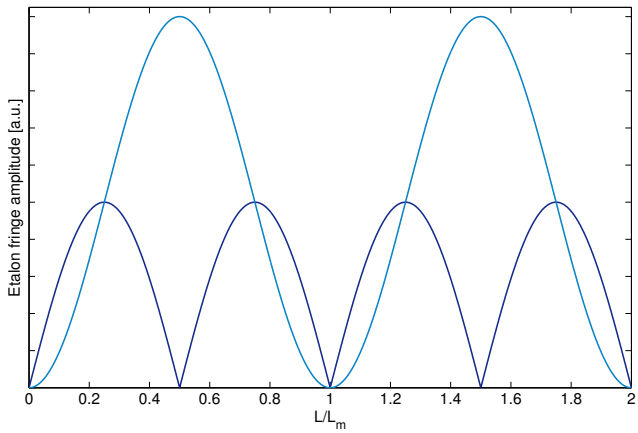

Figure 3.4: Etalon fringe amplitude as a function of normalized etalon surface separation, i.e. L/L_{m}, where L_{m} is given by $c/(2n\nu_{\mathrm{m}})$, for the absorption (dark blue) and dispersion mode of detection (light blue), according to Eqs. (11) and (12) in **publication XII**. Note the different behavior of the two modes of detection for surface separations close to integer values of L_{m} (i.e. $L/L_{\mathrm{m}} = 0, 1, 2$, etc.)

the cavity and demodulated in the same way as the FMS signal) to the EOM, these can be affected and controlled, and thereby minimized, by applying a voltage across the EOM. In that work it is also shown that background signals from EOMs can be kept reasonably stable by the use of an EOM with proton exchanged waveguide since such a waveguide does not support light propagation along the o-axis; this type of EOM has been used for all experimental work this thesis is based upon.

3.3.3 Background signals from etalons and the concept of etalon-immune-distances as a means to reduce such

Since the reflection and transmission of light from etalons are wavelength dependent (due to interference), etalons give rise to background signals in FMS. Parasitic background structures arising from etalons are the source of background signals that can be coped with to some extent by placing as many optical surfaces as possible at so-called etalon-immune distances (EIDs) [4, 43, 45–47, 76, 77]. This concept involves the fact that, whenever the FSR of an etalon matches the spacing of the FM modes (which, in NICE-OHMS, often is equal to the modulation frequency), the modes of the FM spectrum are affected equally (attenuated or phase-shifted) by the etalon. Since the FMS signal depends on differences in the attenuation and phase shift of the various modes, such etalons do not give rise to any FMS signals. Even though this phenomenon has been well-known since 1985, when it was proposed that the background signal from a given etalon originating from an EOM could be eliminated by choosing the modulation frequency equal to the FSR of the EOM-crystal [72],

it was only in 2011, when the concept of etalon-immune-distances (EID) was introduced and used [43]. As is further discussed in **publication XII** and as is illustrated in Fig. 3.4, the EID principle says that there are lengths, $L_{\mathrm{EID}}^{q,\mathrm{abs/disp}}$, equal to $qc/(2n\nu_{\mathrm{m}})$, where q can be equal to $0, 1, 2, ...$ for the dispersion mode of detection and $0, {}^1\!/_2, 1, {}^3\!/_2, ...$ for the absorption mode, for which the contribution of etalons to the attenuation and phase-shift of the modes of the FM spectrum does not appear in the FMS signal.

An important finding of **publication XII** is that although the contribution from an etalon with a length that is close to, but not exactly equal to, an EID, is much stronger in the absorption mode of detection than it is in the dispersion mode[1], although the dispersion signal can become twice as large as the largest absorption signal, which is the case for $q = {}^1\!/_2, {}^3\!/_2, ...$, as can readily be seen from Fig. 3.4 and the following example. It is also showed that the use of the EID concept is of particular importance in NICE-OHMS when an optical circulator is used (see chapter 8.1.6 or **publication VIII**), since then any there cannot be any isolation between the cavity and the fiber coupler, whereby the back-reflection will be coupled back into the circulator again.

Example

Consider an FMS experiment running with a modulation frequency, ν_{m}, of 400 MHz, whereby $L_{\mathrm{EID}}^{1,\mathrm{abs/disp}}$ becomes 37.5 cm. If an etalon has a spacing that is 5 mm larger than $L_{\mathrm{EID}}^{1,\mathrm{abs/disp}}$, the etalon fringe amplitude in absorption is larger than the one for dispersion mode of detection by a factor of around 25. For all plane-parallel optical components with finite thickness (such as lenses, polarizers etc.) only one surface can be put on an EID, implying that the other surface necessarily is positioned off-EID. This underlines the importance of either the use of wedged substrates or a suitable choice of detection mode (preferably dispersion).

[1] This is only valid for EIDs with integer index, where both the absorption and dispersion contribution are close to zero.

4 Optical Resonators

4.1 Optical path length enhancement

As was alluded to above, single-pass absorption spectroscopic techniques are often not capable of detecting small sample concentrations with accompanying weak overall on-resonsance absorbances. Therefore, the sample can be placed in between two mirrors that reflect the probing light back and forth across the sample a number of times. When the light probes different parts of the sample each passage, the combination of sample compartment and mirrors is called a multi-pass cell. A configuration like this effectively increases the interaction length between light and sample to $L(2m+1)$, where L is the spacing between the mirrors and m is the number of round-trips. Here, the number of round-trips is limited by practical issues such as the mirror spacing, mirror size, and properties of the incident Gaussian beam that will inevitably increase in diameter with propagation length, wherefore the effective interaction length does rarely exceeds a few hundreds of metres [1].

The most effective way of optical path length enhancement is a Fabry-Pérot cavity[1]. In its most simple realisation it consists of two highly-reflective mirrors

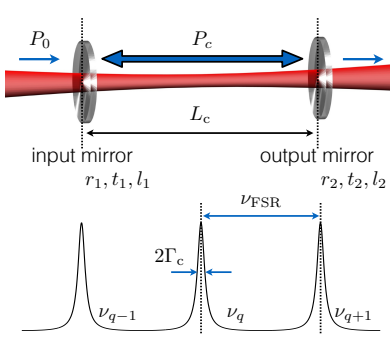

Figure 4.1: Two parallel mirrors constituting a Fabry-Pérot cavity. Light inside the cavity creates a standing wave allowing only certain frequencies to exist inside the resonator. See text for definitions and explanations of the symbols.

[1] Fabry-Pérot cavities are also termed Fabry-Pérot resonators, optical resonators or optical

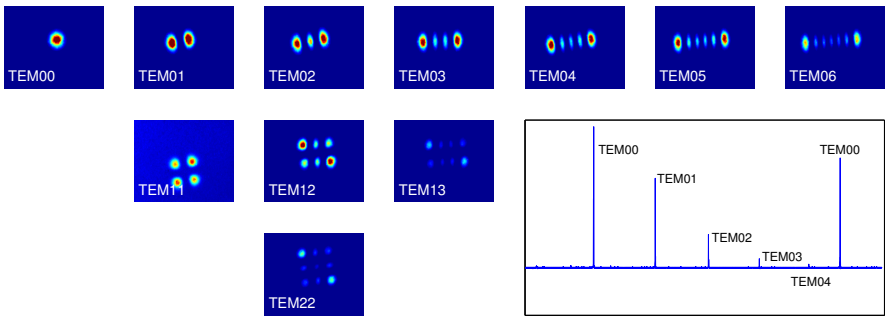

Figure 4.2: Transmission of a Fabry-Pérot cavity for a beam that is slightly off from perfect alignment. The lowermost right panel shows the spectrum for a laser frequency excursion slightly larger than one FSR and for a spatial detuning in one dimension. Some of the higher order TEM modes become evoked. All the other panels (i.e. those with blue background) illustrate the beam-profile of the resonator modes from a cavity created by two mirrors with reflectivity 99.94% and separated by a distance of 39.4 cm, recorded with a CCD camera under locked conditions.

that are parallel to each other (Fig. 4.1). Light inside the cavity that propagates perpendicularly to the mirror surfaces will travel in both directions and will thereby create a standing wave, provided that the length of the cavity, L_c, fulfills the condition $L_c = q\lambda_0/2$, where λ_0 is the wavelength of the light and q is a positive integer. This implies that only frequencies

$$\nu_q = \frac{qc}{2nL_c}, \tag{4.1}$$

with n being the index of refraction of the gas in the cavity and c the speed of light, can exist inside the resonator, as all other frequencies will interfere destructively. These modes are called fundamental transverse electromagnetic (TEM) or longitudinal modes of the resonator, commonly labelled as TEM_{00}. The frequency spacing of two consecutive TEM_{00} modes is called the free-spectral range (FSR) of the resonator and is given by

$$\nu_{\mathrm{FSR}} = \nu_q - \nu_{q-1} = \frac{c}{2nL_c}. \tag{4.2}$$

For an inclining incident beam, also higher order TEM modes can be evoked. As an illustration of this, Fig. 4.2 shows, by the lowermost right panel, the transmission spectrum of one of the cavities described in chapter 8 for a laser frequency excursion that is slightly larger than one FSR and for an incident beam that was slightly detuned from perfect alignment in one dimension. The other panels in the figure show the shape of the beam transmitted through the resonator when the laser was locked successively to various TEM modes. Note that not all modes from the blue panels are evoked in the particular spectrum

cavities.

displayed; in order to induce some of the modes, the initial alignment had to be changed. Moreover, to get a good contrast, the mode the laser was locked to was maximized for the corresponding case represented in one of the blue panels.

In order to characterize the properties of a resonator, the following entities can conveniently be defined. Firstly, it is convenient to characterize each mirror, i, by its intensity transmission, reflection, and losses coefficients, i.e. t_i, r_i, and l_i, respectively. Since energy is conserved, the coefficients are related by $t_i + r_i + l_i \equiv 1$. Secondly, the (HWHM) width of a resonator mode can, for the case of highly reflective mirrors ($r_{1,2} \approx 1$), be written as [26]

$$\Gamma_c = \frac{\nu_{FSR}}{\pi} \frac{1 - \sqrt{r_1 r_2}}{2\sqrt[4]{r_1 r_2}}. \tag{4.3}$$

Thirdly, the resonator finesse, F, is defined as the ratio of the FSR and the full mode width, i.e. as

$$F \equiv \frac{\nu_{FSR}}{2\Gamma_c} = \frac{\pi \sqrt[4]{r_1 r_2}}{1 - \sqrt{r_1 r_2}}, \tag{4.4}$$

which, for the case of mirrors with equal reflection coefficients, i.e. for $r_1 = r_2 \equiv R$ becomes $\pi\sqrt{R}/(1-R)$, which, for a cavity constructed around high reflectivity mirrors (i.e. with $R \approx 1$) in turn can be written as $\pi/(1-R)$. Fourthly, the finesse also determines the enhanced interaction length between light and sample, which can be written as [10]

$$L_{eff} = \frac{2F}{\pi} L_c. \tag{4.5}$$

This is valid for the case when the intra-cavity absorption due to an absorber, $\alpha(\nu)$, does not compromise the finesse of the resonator, i.e. when $\alpha(\nu) \ll \pi/2F$. Fifthly, some fraction of the light will leak out through the second mirror after each round-trip implying that each photon has an average life-time inside the resonator that is given by its decay time, τ_c, which is connected to the finesse and FSR through the relation [26]

$$\tau_c = \frac{F}{\pi \nu_{FSR}}. \tag{4.6}$$

Sixthly, yet another important property, especially when saturation spectroscopy

Example

Consider an optical resonator with mirrors of equal reflectivity spaced by 0.4 m. The table below shows the corresponding cavity properties for two different mirror reflectivities.

r	F	ν_{FSR}	Γ_c	L_{eff}	τ_c	κ
0.995	630	375 MHz	30 kHz	160 m	0.5 µs	200
0.9999	31000	375 MHz	6.0 kHz	8000 m	27 µs	10000

is to be performed, is the intra-cavity power buildup, κ, which for a impedance matched cavity (no reflection on resonance) is given by

$$\kappa = \frac{P_\mathrm{c}}{P_0} = \frac{F}{\pi}, \tag{4.7}$$

where P_c is the unidirectional intra-cavity power and P_0 the incident power.

4.2 Spatial mode matching

In order to make it possible for a beam to enter an optical resonator, the shape of the beam has to spatially match the resonator's geometry. In practice, most often the shape of a laser beam is given by properties of the laser or, in the case of light exiting through an optical fiber, by the output coupler. In many cases, and in particular when light passes a single mode optical fiber followed by a good quality output coupler, the light can be assumed to have a Gaussian intensity distribution.

4.2.1 Gaussian beams

A Gaussian beam propagating in the z-direction has an intensity distribution in the x-y-plane that is given by [59]

$$I(r,z) \sim \left(\frac{w_0}{w(z)}\right)^2 \mathrm{e}^{-2r^2/w^2(z)}, \tag{4.8}$$

where r the distance from the optical axis, given by $(x^2+y^2)^{1/2}$ and w_0 is the spot size (radius) in the waist. For any position, z, along the optical axis the spot size is given by

$$w(z) = w_0\sqrt{1+\frac{z^2}{z_0^2}}, \tag{4.9}$$

where z_0 is the so called Rayleigh range, which, in turn, is given by

$$z_0 = \pi w_0^2/\lambda_0 \tag{4.10}$$

and which is a measure of the length of the waist region. It is convenient to describe a Gaussian beam at a position z along the optical axis in terms of its complex beam parameter, q, as

$$\frac{1}{q(z)} = \frac{1}{R_\mathrm{G}(z)} + \frac{i\lambda}{\pi w^2(z)}, \tag{4.11}$$

where R_G is the radius of curvature of the beam, as illustrated in Fig. 4.3, given by

$$R_\mathrm{G}(z) = z + \frac{z_0^2}{z}. \tag{4.12}$$

The complex beam parameter at a given position is a measure of both the width of the beam at that position, represented by the imaginary part, as well as

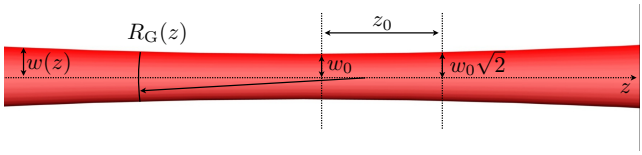

Figure 4.3: Laser beam with Gaussian intensity distribution. See text for definitions of the parameters.

	ABCD-matrix	Details
Propagation	$\begin{pmatrix} 1 & d \\ 0 & 1 \end{pmatrix}$	d: length of propagation
Thin lens	$\begin{pmatrix} 1 & 0 \\ -1/f & 1 \end{pmatrix}$	f: focal length $f > 0$ for a positive lens $f < 0$ for a negative lens

Table 4.1: ABCD matrices for propagation in a medium with constant refractive index and for refraction by a thin lens.

the curvature of the beam, represented by its real part. If q is known for a position, z_1, it can be calculated for any other position, z_2, by the ABCD law for Gaussian beams, i.e. according to

$$q(z_2) = \frac{Aq(z_1) + B}{Cq(z_1) + D}, \tag{4.13}$$

where A, B, C, and D are the components of the corresponding ray transfer matrix or ABCD-matrix, M, given by

$$M = \begin{pmatrix} A & B \\ C & D \end{pmatrix}, \tag{4.14}$$

which describes the physical effect that is affecting the beam, e.g. a translation, refraction, or reflection. Table 4.1 shows the ABCD-matrices that are commonly used in context with optical resonators, viz. this for propagation in a medium with constant refractive index and for refraction by a thin lens. As is shown below, these individual matrices are combined in reverse order to provide the total matrix for the entire optical system.

4.2.2 Spatial incoupling of a Gaussian beam into a resonator

Since both the geometry of the laser beam and that of the resonator are given, the beam has to be shaped spatially to match the resonator's geometry. The key point is to match the radii of curvature of the beam at the position of the mirrors to those of the mirrors. Since it is of importance to reduce the number of optical surfaces in the system (to reduce the risk for etalons), it is an

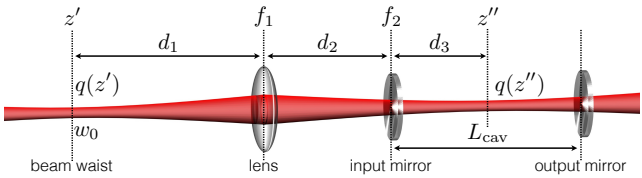

Figure 4.4: Incoupling of a Gaussian beam into a symmetrical cavity. See text for a definition of the variables.

advantage if this can be done by a single lens. As is shown below, in the case of a Gaussian beam, this is often achievable by the use of a single positive lens.

Figure 4.4 illustrates this for the case of a symmetrical cavity, i.e. one with two identical mirrors spaced by a distance L_{cav}. The initial beam emerging from the fiber collimator has a focus at the position z', i.e. a distance d_0 after the collimator (not indicated in the Figure) with a beam size of w_0. As the wave-front is flat in the focus, this implies that its complex beam parameter at this position, $q(z')$, becomes

$$q(z') = -iz'_0, \tag{4.15}$$

which follows from Eqs. (4.10) and (4.11) with $R_{\mathrm{G}}(z') = \infty$. For symmetry reasons, the new focus inside a symmetrical cavity has to be in its center, z''. The complex beam parameter at this position, $q(z'')$, can be calculated by the ABCD-law, according to Eq. (4.13), as

$$q(z'') = \frac{Aq(z') + B}{Cq(z') + D}, \tag{4.16}$$

where A, B, C, and D now are the components of the matrix M_{tot} describing the entire beam path from the initial focus, z', to the new focus, z''. Along this path the beam first propagates in free-space over a distance d_1 to the lens, is then refracted by the lens with focal length f_1, travels another distance d_2 until it reaches the input mirror, is refracted by the input mirror, which acts as a negative (diverging) lens with focal length f_2, before it finally propagates another distance $d_3 = L_{\mathrm{cav}}/2$ into the focus of the cavity. This implies that M_{tot} is given by

$$M_{\mathrm{tot}} = \begin{pmatrix} 1 & L_{\mathrm{cav}}/2 \\ 0 & 1 \end{pmatrix} \begin{pmatrix} 1 & 0 \\ -1/f_2 & 1 \end{pmatrix} \begin{pmatrix} 1 & d_2 \\ 0 & 1 \end{pmatrix} \begin{pmatrix} 1 & 0 \\ -1/f_1 & 1 \end{pmatrix} \begin{pmatrix} 1 & d_1 \\ 0 & 1 \end{pmatrix}, \tag{4.17}$$

where f_2, for a thin plano-concave mirror substrate with an index of refraction n_{m}, can be calculated by [78]

$$\frac{1}{f_2} = (n_{\mathrm{m}} - 1)\left(-\frac{1}{r_{\mathrm{m}}}\right), \tag{4.18}$$

where, in turn, $r_{\mathrm{m}} > 0$ is the radius of the concave mirror surface.

The Rayleigh range of a symmetrical cavity can be calculated by Eq. (4.12) to

$$z_0^{\mathrm{cav}} = \sqrt{\frac{L_{\mathrm{cav}}}{2}\left(r_{\mathrm{m}} - \frac{L_{\mathrm{cav}}}{2}\right)}, \tag{4.19}$$

which yields a beam parameter in the cavity focus of

$$q(z'') = -iz_0^{\mathrm{cav}}. \tag{4.20}$$

Combining Eqs. (4.16) and (4.20) and comparing the real and imaginary part, one obtains the two conditions

$$\frac{z_0^{\mathrm{cav}}}{z_0'} = \frac{AD - BC}{C^2 z_0'^2 + D^2} = \frac{1}{C^2 z_0'^2 + D^2} \tag{4.21}$$

and

$$BD + ACz_0'^2 = 0, \tag{4.22}$$

which, for a given focal length f_1 of the incoupling lens, can be solved for the two remaining parameters d_1 and d_2. The last step in 4.21 is valid since the determinant of M_{tot}, which is given by $AD - BC$, is unity, as a consequence of the fact that the determinants of all sub-matrices in M_{tot} are unity as well. The two above equations yield the two solutions

$$d_1 = f_1 \mp \frac{\xi}{f_2^2 z_0^{\mathrm{cav}}} \tag{4.23}$$

and

$$d_2 = \frac{(d_3 - d_2)[d_2(f_1 + f_2) - f_1 f_2]z_0' + (f_1 + f_2)z_0'(z_0^{\mathrm{cav}})^2 \mp \xi}{z_0'\left[(d_3 - f_2)^2 + (z_0^{\mathrm{cav}})^2\right]}, \tag{4.24}$$

where

$$\xi = \sqrt{f_2^2 z_0' z_0^{\mathrm{cav}}\left[f_1^2(d_3 - f_2)^2 - f_2^2 z_0' z_0^{\mathrm{cav}} + f_1^2 z_0^{\mathrm{cav}}\right]}. \tag{4.25}$$

Example

Assume a symmetric cavity with a length of 40 cm and mirrors with a radius, r_{m}, of 1 m, and an index of refraction of the 6.35 mm thick substrates of 1.44. Assume furthermore that the light, which has a wavelength of 1531 nm, has a focus 20 cm after the collimator with a beam waist of 0.66 mm.
For efficient incoupling of the light into the cavity, a lens with focal length $f_1 = 60$ cm could be placed at $d_1 = 17$ cm after the focus (and therefore 37 cm after the collimator), whereas the cavity input mirror has to be placed at $d_2 = 21$ cm after the lens. Alternative values for the same lens are $d_1 = 103$ cm $d_2 = 52$ cm.
A lens with focal length $f_1 = 100$ cm yields $d_1 = -38$ cm and $d_2 = 25$ cm or $d_1 = 238$ cm and $d_2 = 127$ cm. Note that the first solution is unrealisable since the lens would have to be placed before the fiber collimator. A lens with focal length $f_1 = 50$ cm, in turn, provides no solution at all.

5 Laser Frequency Stabilization

5.1 Background

In many laser-applications it is necessary to lock the laser's frequency to a high-finesse resonator, e.g. in laser metrology or analytical and precision spectroscopy [79]. While in some applications the cavity has to be an ultra-stable reference, in NICE-OHMS it is sufficient to stabilize the laser frequency with respect to the cavity, while the cavity itself can jitter[1] to some extent. In any case, in order to make use of an optical cavity, light has to enter the cavity, i.e. the frequency spectrum of the laser has to (at least partly) overlap with at least one transmission mode of the cavity. Since a narrow cavity mode will convert frequency noise of the laser with respect to the cavity into amplitude (intensity) noise, it is beneficial if the laser center frequency is perfectly on resonance with the cavity mode, as is illustrated in Fig. 5.1. It can be seen from the Figure that a given excursion of the laser frequency will yield significantly different amplitude noise depending on whether the laser frequency is locked

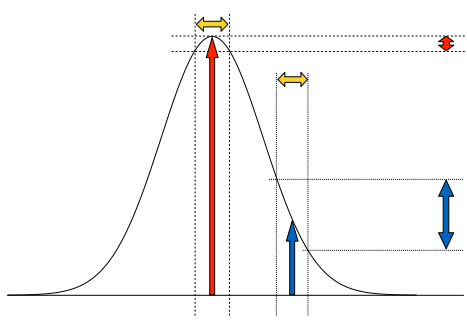

Figure 5.1: Illustration of frequency-to-amplitude noise conversion. For the same amount of frequency noise (yellow), a laser will give rise to significantly more amplitude noise when the laser is locked to the side of a cavity mode (blue), as compared to when it is locked to the center of the mode (red).

[1] It should be clear though that excessive cavity jitter still ought to be avoided, as it will affect also the relative laser-cavity jitter by putting high tension on the locking scheme. Moreover, it cannot jitter too much with respect to an analytical transition, since the line profile then will become affected by noise, as well.

to the center or to a flank of a mode, which makes the first choice much more desirable. Also the transmission of light through a cavity will be higher if a laser can be held locked at resonance of a cavity mode.

While the width of the cavity mode is well-defined (see chapter 4), the line width of the laser depends on the timescale which it is evaluated on, since the spectrum of the laser-noise is dissimilar for fast and slow components [79]. While a typical diode laser can have a fast line width of only a few tens of kHz on a short timescale (tens to hundreds of microseconds), defining the smallest spectral features the laser can resolve, this fast line width (commonly referred to as the laser line width) might be completely covered by the slow line width arising from low frequency fluctuations in the acoustic domain, or really slow drifts mostly from temperature effects. Since, in the best case, the total line width of the laser is smaller than the cavity mode width, the problem of laser-cavity locking is projected onto different time or frequency scales, as is exemplified in Fig. 5.2.

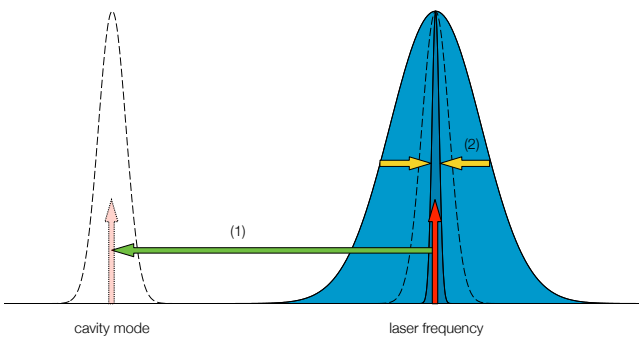

Figure 5.2: Principle of laser frequency stabilization. (1) The slow line width (light blue area) of the laser is shifted as indicated by the green arrow to be centered around a cavity mode (dashed curve to the left. (2) The fast line width is squeezed (yellow arrows) into the cavity mode and becomes in the best case smaller than that.

On a slow time scale, the line-width of the laser is excessively larger than on fast time scales, so initially the laser center frequency has to be adjusted (preferably locked) so it becomes equal to (or at least in the closest proximity to) the center frequency of the cavity mode. In this case, there will be a lot of frequency-to-amplitude noise conversion, as the laser frequency still jitters over the entire cavity mode profile. In fact, for some instants of time it can even be outside the cavity mode[2]. As the next step the remaining laser frequency line width has to be squeezed into the cavity mode, which usually is the technically more demanding part, as the corrections of the laser frequency have to be fast.

[2]If this happens on a really short time scale (shorter than the lifetime of the electric field of the cavity, also called storage-time and equal to τ_{cav} in chapter 4), the lock can still be maintained since the cavity has a memory of the average laser frequency during the passed time interval of length τ_{cav}; if the frequency excursion, however, was longer than τ_{cav}, the lock will be lost.

Common to all locking techniques is the need of an error signal, a measure that tells the experimentalist, or more precise, the controller circuit through which the error signal is fed back to the laser, how the frequency of the laser has to be changed, i.e. how much and in which direction, so as to be on resonance with the cavity mode. The two most common techniques [79] for the derivation of this error signal are side-of-fringe locking and the Pound-Drever-Hall (PDH) technique [73]. The former works as follows: the laser frequency is deliberately put on the side of a cavity fringe (therefrom the name) and the intensity is monitored for example in the cavity-transmitted light, whereby the transmitted intensity indicates in which direction the laser frequency has to be adjusted. Even though this method is strikingly simple to implement, it has a number of drawbacks, e.g. that the laser error signal is detected at DC frequencies and it is fully affected by any amplitude noise in the laser at low frequencies. In addition, the laser cannot be locked to the center of a mode (which would be the best as described above), since the error signal in this case would no longer contain any information about the direction of the frequency excursion. In contrast, the PDH technique derives a sign-sensitive error signal with less noise by detection in the radio-frequency domain (in fact, leaving the major part of the technical noise behind).

5.2 Pound-Drever-Hall error signal

As a pure FM technique, the PDH technique derives an error signal in the same way as was the case for the FMS signal described in chapter 3. For this, the frequency of the laser is modulated[3] at a frequency, ν_{PDH}, which is chosen smaller than the FSR of the cavity, but typically well outside[4] the cavity mode width, most often in the 10 to 50 MHz range [79]. For low modulation indices this provides the carrier with two PDH sidebands, which, in turn, gives rise to two perfectly out-of-phase beat-notes at ν_{PDH} from the interference with the reflected carrier and the leakage of the electrical field stored in the cavity. For the case when the laser is on resonance with the cavity mode, the beat-notes cancel. Any small deviation of the laser frequency, though, will contribute to a net beat-note on the detector in cavity-reflection. In the same way as in FMS, this beat-note can be demodulated by mixing it with a phase-adjusted reference signal from the PDH modulation source (in order to obtain the dispersion signal), yielding—after filtering out the low-pass component—the PDH error signal, which is depicted in Figure 5.3, for the case when the laser frequency is swept around a cavity mode with a total span of more than $2\nu_{\mathrm{PDH}}$.

As was alluded to above, apart from the PDH-sidebands, the light in cavity-reflection consists of the fraction of the incident carrier that is reflected back

[3]The laser can either be modulated directly if the response is sufficiently large (e.g. by modulating the current of a diode laser) or by external means (e.g. by sending the light through an EOM to which the modulation signal is applied).

[4]In some systems, where two cavities in series have to be locked to a laser frequency, the modulation frequency can be chosen within the cavity mode width of the first cavity, so that the sidebands are partly reflected for generating a PDH error signal for the locking of the first cavity and partly transmitted for being "recycled" for the derivation of an error signal at the second cavity.

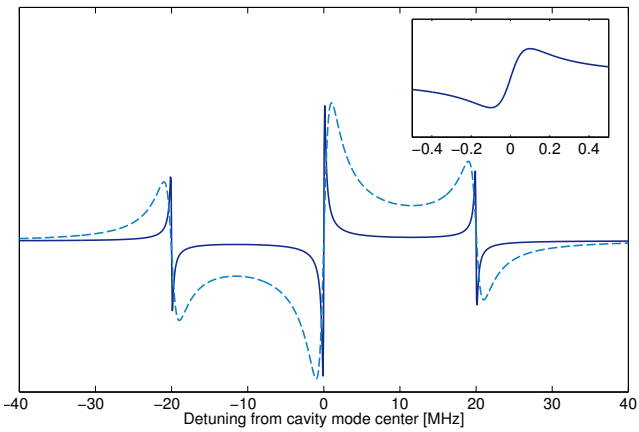

Figure 5.3: Pound-Drever-Hall error signals for a modulation frequency, ν_{PDH}, of 20 MHz and two different cavity HWHM mode widths, viz. 100 kHz (solid, dark blue curve) and 1 MHz (dashed, light blue curve). The plot in the upper right corner shows an enlargement of the center part of the signal for the first case. As can be seen, the peaks are separated by the FWHM of the cavity mode width so that the slope can be approximated [26] as $V_{\mathrm{PDH}}^{\mathrm{pp}}/(2\Gamma_{\mathrm{c}})$, where $V_{\mathrm{PDH}}^{\mathrm{pp}}$ is the peak-to-peak voltage of the center part of the PDH error signal.

from the cavity together with the leakage from cavity that was stored for an average time of τ_{cav}; the latter can be seen as a memory of the average laser frequency during the passed time interval of length τ_{cav}. For optical frequency excursions at (Fourier) frequencies below the cavity mode width, the PDH error signal is a measure of the frequency deviation of the carrier from the cavity mode center (given in units of V/Hz, where Hz is to be understood as an optical frequency) [79]. For (Fourier) frequencies above the mode width of the cavity, the PDH error signal becomes instead a measure of the phase, and the system response falls with $1/f$, wherefore a cavity in control systems has to be treated as a low-pass filter with a corner frequency equal to the mode width.

5.3 Feedback design

As soon as the PDH error signal is present it can be used to actively control and stabilize the laser frequency so as to be resonant with a cavity mode. This can be done by negative feedback of the error signal to the laser through a loop filter servo [79]. The entire closed system consisting of laser, cavity, detection and demodulation, and loop filter is called a feedback loop. Such a feedback loop is depicted in Fig. 5.4. The stabilized laser frequency, X, in the presence of an external disturbance, Z, is given by [26, 80]

$$X = \frac{1}{1 + [G(f)H(f)]^{-1}} \left[X_{\mathrm{ref}} + \frac{Z}{H(f)} \right], \tag{5.1}$$

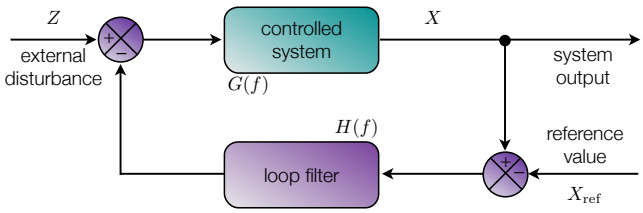

Figure 5.4: Control loop structure for negative feedback. The output of the controlled system is compared with a reference value which yields the error signal, that is sent through the loop filter before it is fed back to the controlled system. In this scheme, external disturbances will be corrected for.

where G and H denote the frequency transfer function (FFT) of the laser and loop filter, respectively, and X_{ref} is a reference value[5]. The factor in front of the square brackets is called the closed-loop FFT and determines how well the laser frequency agrees with the reference value. It can be seen that if the open-loop FFT, defined as $G(f)H(f)$, is large, whereby $[G(f)H(f)]^{-1}$ is small, the closed-loop FFT approaches unity. In this case, disturbances enter with a factor of $1/H(f)$, i.e. the inverse of the loop filter FFT.

A convenient way to illustrate FFTs are so-called Bode-plots (see Fig. 5.5), which typically consist of two graphs, showing the gain (the absolute value of the FFT, most commonly in terms of dB) and the phase (the angle between the FFT and the real axis in the complex plane) as a function of frequency. The frequency, where the gain becomes unity (0 dB), is called the unity gain point, denoted $f_{0\mathrm{dB}}$, and is also referred to as the bandwidth of the system. To fulfill conditions of stability, at this point the phase should have a certain margin to $-180°$, that often is referred to as the phase margin and considered to be around 35°. The gain margin is the amount the gain can be increased, so that $f_{0\mathrm{dB}}$ becomes $f_{-180°}$, the frequency at which the phase has developed to $-180°$.

A start in designing the loop filter electronics is to assess the FFT of the laser, $G(f)$, i.e. it has to be measured how much optical frequency excursion the laser exhibits as a reaction to a sinusoidal input signal with a given frequency, f, and a given amplitude. As a consequence $G(f)$ is given in units of Hz/V; note the relation to the slope of the PDH error signal, which has the inverse dimensions, i.e. V/Hz. Once $G(f)$ is known, the loop filter FFT, $H(f)$, can be designed. In general, this can be complex. There are a few rules of thumb, though, that can serve as a guideline: (*i*) The bandwidth of the controller should be as large as needed, which practically in the case of laser stabilization means as large as possible. However, there should always be enough phase margin in the phase of the open-loop FFT within the bandwidth of the system. (*ii*) The slope of the gain curve around the unity gain frequency should be not more than -20 dB/decade in order to ensure an appropriate gain margin. Also here care should be taken to keep sufficient phase margin. (*iii*) Technical noise is largest at low frequencies. One such is the additional disturbance at

[5]In this case representing the center frequency of a cavity mode.

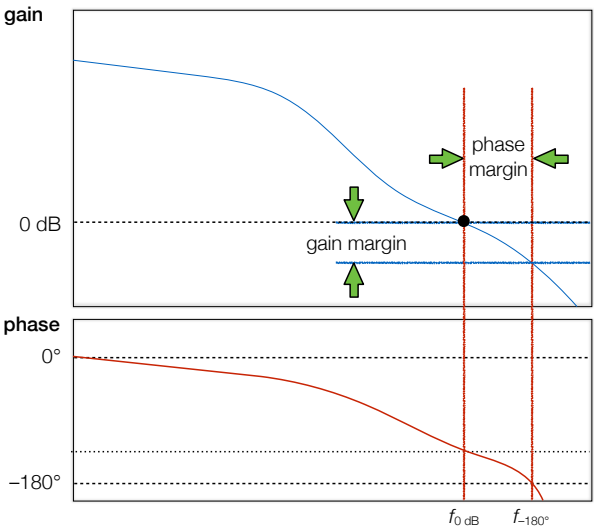

Figure 5.5: Bode plot of an arbitrarily chosen system. The gain and phase of the FFT are typically shown in two separate graphs on top of each other so as to provide a common frequency scale. See text for details.

a low frequency that is introduced in order to sweep the laser frequency over a molecular transition. For this reason, one should aim for as large open-loop gain as large as possible in the low frequency domain. Especially helpful in this context is a $-40\,\mathrm{dB/decade}$ slope[6] for the lowest frequencies; in this case at pure DC (which in a Bode-plot never is reached) the phase approaches $-180°$, which, however, does not cause any problem since the gain is far from zero in this region, it is often huge. (*iv*) In the case of parallel feedback to different frequency actuators, the FFT of the entire system is given by the sum of the different sub-systems. Here, it is important that the slopes of the gain curves at the so-called hand-over point[7] should have a difference of not more than $20\,\mathrm{dB/decade}$ and the phases at this point should not differ by more than $90°$. (*v*) As was alluded to above, the cavity acts as low-pass filter. To circumvent that this affects the bandwidth of the system, a phase-lead could be added to the loop filter to compensate for this.

[6] This can be achieved by two integrators in series.

[7] The point when the gain of sub-system 1 becomes larger than the one of sub-system 2.

6 NICE-OHMS

6.1 Principles of NICE-OHMS

NICE-OHMS combines cavity-enhancement for prolongation of the interaction length between laser light and a molecular sample and frequency modulation (FM) for active reduction of noise. In addition, as is further discussed below, and, as is an important property of the technique, their combination gives rise to an immunity to frequency-to-intensity noise conversion that many other cw-CE techniques suffer from. Both the CE and the FM have to work together properly in order to take full advantage of all concepts. Figure 6.1 illustrates the generic structure of the NICE-OHMS technique, explained below.

As was discussed above, cavity-enhancement implies that the laser frequency has to be locked to a mode of the optical cavity. This is most often done by the

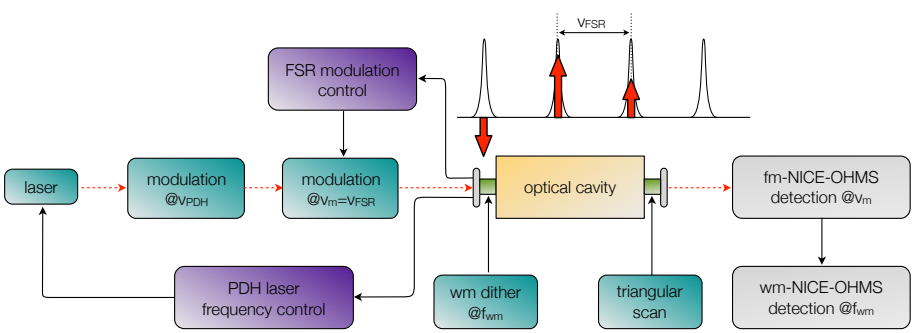

Figure 6.1: Generic NICE-OHMS setup [4]. In order to perform FMS inside the cavity, both the laser frequency and the sideband spacing have to be controlled. The light is modulated at the two frequencies ν_{PDH} and ν_{m} for PDH locking and FMS detection, respectively. The cavity-transmitted light is demodulated with a reference signal of the modulation at ν_{m}, yielding the fm-NICE-OHMS signal. Optionally, a WM layer can be applied for further noise-reduction.

Pound-Drever-Hall (PDH) technique [73]. For this, the light is modulated at a frequency, ν_{PDH}, in the RF domain, typically a few up to a few tens of MHz, but at least so large that the first order sidebands are situated well-outside the cavity modes. Depending on the particular system, this can either be done by modulating the laser source directly or by external means with an electro-optic modulator (EOM). The two beat-notes at ν_{m} that arise from the interference between the carrier and the two sidebands, whenever the laser frequency is slightly detuned from a cavity mode, are then detected in cavity-reflection. This beat-note is then demodulated with a reference signal (in dispersion phase) from the local oscillator, yielding the PDH error signal, which is fed back to the laser frequency control. Typically, this error signal is filtered with PID-regulators so that the entire feedback-loop matches the criteria for a stable control system. Sometimes the bandwidth of the laser frequency actuator is not large enough to correct for major noise contributions; whenever this is the case, the frequency of the laser needs to be stabilized by additional external means, e.g. by the use of an acousto-optic modulator (AOM) or electro-optic modulator (EOM).

Having the laser well-locked to a cavity mode, the light is additionally modulated at a second frequency, ν_{m}, which, in the presence of an optical cavity, has to be controlled to be equal to a multiple of the FSR of the cavity, ν_{FSR}. For this, as was suggested by deVoe and Brewer [81], an error signal can be derived in cavity-reflection by demodulating the light at one of the frequencies[1] $\nu_{\mathrm{m}} \pm \nu_{\mathrm{PDH}}$, which then is fed back to the tunable modulation source. This will allow both the carrier and the sidebands to enter the cavity and FM spectroscopy can be performed as if the cavity would not be present, yet fully benefiting from the cavity-enhanced interaction length. Moreover, since the length of the cavity is changed in order to induce a laser frequency scan across a molecular transition, the modulation frequency, ν_{m}, will follow the accompanied change of the FSR. Having both the laser-cavity lock and the modulation frequency lock well adjusted, remaining laser frequency jitter will, in the absence of absorbers, cause the same attenuation and phase shift (induced by the cavity modes) to all modes of the FM mode spectrum, the effect of which will cancel as can immediately seen from Eq. (3.7). This feature is called noise-immunity and is part of the term "NICE-OHMS", since it arises from the combination of cavity enhancement and frequency modulation, while it is not inherent to either of the techniques themselves.

The NICE-OHMS signal can finally be derived by demodulating the beat-note from the interference of the carrier and the two FM sidebands in cavity-transmission with a phase-adjusted reference signal from the modulation source. Further noise-reduction or elemination of sloping backgrounds can be achieved by wavelength modulation (WM). A signal from a modulation source is then used to dither the cavity length. Care has to be taken to guarantee a tight laser-cavity lock at that frequency. The modulation can be detected by lock-in detection at f_{wm} of the NICE-OHMS signals derived above. This is of particular importance for sD detection since the sD-signals reside on top of Db-signals.

[1] Due to the simultaneous modulation at two frequencies, beat notes appear even at the sum and difference frequency of those.

6.2 Doppler-broadened NICE-OHMS

6.2.1 Doppler-broadened NICE-OHMS signals

In the presence of an optical cavity containing an absorber, the Doppler-broadened (Db) NICE-OHMS signal, S_{Db}, is obtained directly from Eq. (3.7) together with Eqs. (2.10) and (2.11), additionally taking into account the cavity enhanced interaction length between light and sample, which according to Eq. (4.5) is increased by a factor of $2F/\pi$, and can thereby be written as [48]

$$S_{\mathrm{Db}}(\nu_{\mathrm{d}}, \theta_{\mathrm{fm}}, G) = S_0 \bar{\chi}_{\mathrm{NO}}^{\mathrm{Db}}(\nu_{\mathrm{d}}, \theta_{\mathrm{fm}}, G), \tag{6.1}$$

where S_0 is the signal strength, given by

$$S_0 = \eta_{\mathrm{fm}} \frac{F}{\pi} \alpha_0 L P_0 = \eta_{\mathrm{fm}} \frac{F}{\pi} S c_{\mathrm{rel}} p \chi_0 L P_0, \tag{6.2}$$

and where $\bar{\chi}_{\mathrm{NO}}^{\mathrm{Db}}$ is the Doppler-peak-normalized NICE-OHMS line shape function, given by

$$\begin{aligned} \bar{\chi}_{\mathrm{NO}}^{\mathrm{Db}}(\nu_{\mathrm{d}}, \theta_{\mathrm{fm}}, G) = \frac{1}{\chi_0} \sum_{k=0}^{+\infty} & J_k(\beta) J_{k+1}(\beta) \\ & \left[\left(\chi_{-k-1}^{\mathrm{abs}} + \chi_{-k}^{\mathrm{abs}} - \chi_k^{\mathrm{abs}} - \chi_{k+1}^{\mathrm{abs}} \right) \sin(\theta_{\mathrm{fm}}) \right] \\ & + \left[\left(\chi_{-k-1}^{\mathrm{disp}} - \chi_{-k}^{\mathrm{disp}} - \chi_k^{\mathrm{disp}} + \chi_{k+1}^{\mathrm{disp}} \right) \cos(\theta_{\mathrm{fm}}) \right], \end{aligned} \tag{6.3}$$

where the area normalized line shape functions, $\chi_k^{\mathrm{abs/disp}}$, are to be understood as function of frequency detuning and degree of saturation, i.e. as $\chi_k^{\mathrm{abs,disp}} \equiv \chi_k^{\mathrm{abs,disp}}(\nu_{\mathrm{d}}, G_k)$. Here, L is the length of the cavity and G_k represents the degree of saturation induced by mode k of the FM spectrum, thus given by $J_k^2(\beta) I_{\mathrm{c}}/I_{\mathrm{sat}}$, where I_{c} is the intra-cavity intensity, which is given by $(F/\pi) I_0$ and I_{sat} is the saturation intensity of the transition. Note, that in the case of optical saturation, i.e. for the situation when $G_k \ll 1$ does not hold for at least one mode, the Eqs. (6.1)–(6.3) only hold for the case when the collisional width of the transition, Γ_{L}, is much smaller than the modulation frequency, ν_{m}, so that no group of molecules is exposed to an interaction with more than one mode of the light at a time; for the case when $\nu_{\mathrm{m}} \gg \Gamma_{\mathrm{L}}$ does not hold, Eq. (6.1) is still valid under unsaturated conditions, i.e. when $G_k \ll 1$ for all modes. As stated above, the product $S c_{\mathrm{rel}} p \chi_0$ represents the on-resonance absorption coefficient, i.e. absorption per unit length, α_0. The factor $\mathrm{e}^{2\delta_0}$ in Eq. (3.7) has here been neglected since NICE-OHMS typically is run under the condition of small sample absorption. Since the shape of NICE-OHMS signals is similar to that of FMS signals, the reader is referred to Fig. 3.3 for an illustration; note though that the signal size is increased by a factor of $2F/\pi$.

6.2.2 On the design of an instrumentation

In some cases an experimentalist has the possibility to design a new system from scratch. Even though this for sure might be a challenging task, it offers

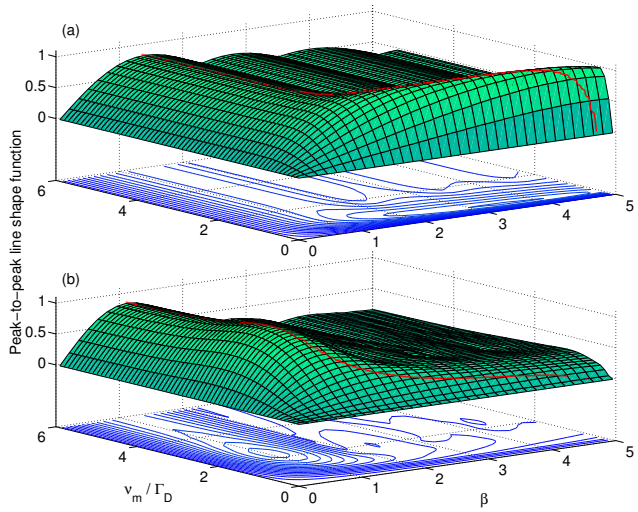

Figure 6.2: Peak-to-peak of the NICE-OHMS line shape as a function of β and $\nu_{\mathrm{m}}/\Gamma_{\mathrm{d}}$ for the absorption (panel [a]) and dispersion phase (panel [b]) in the Doppler limit. The red crest line indicates the optimum choice of for β for any given ratio $\nu_{\mathrm{m}}/\Gamma_{\mathrm{d}}$.

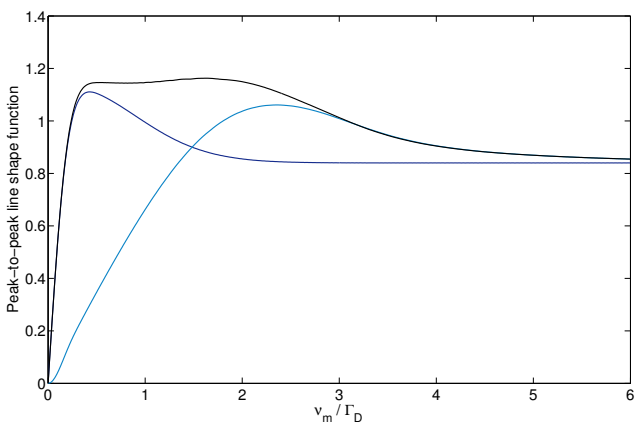

Figure 6.3: NICE-OHMS line shape peak-to-peak in the Doppler limit as a function of the normalized modulation frequency for absorption (dark blue) and dispersion phase (light blue), as well as the phase that yields maximum signal (black).

a unique chance to choose technical solutions or optimize system parameters. While for the former experimental knowledge and experience are necessities, the latter can be tackled by choosing system parameters that maximize the NICE-OHMS signal as given by Eqs. (6.1)–(6.3) above. Although the dependencies of both FMS and Db-NICE-OHMS on various entities have been investigated previously in the literature, there was until recently no coherent description that encompassed all relevant parameters. The development of such a description has been a part of the work on which this thesis is built. Therefore, for the first time, such an analysis is provided in **publication X**, with some experimental verifications presented in **publication XI**

A close look at Eq. (6.1) makes it obvious that for a maximum NICE-OHMS signal, the signal strength, $S_0, given by$Eq. (6.2), should be maximized. As long as the signal is not limited by noise in the laser light, the most straightforward action is to choose a detector with large responsivity, and to shine as much

light on it as it can sustain without being saturated. The cavity finesse[2], as the next parameter, should be chosen as large as possible, without introducing too much noise due to a decreased performance of the mode locking. The choice of a transition with large line strength is, in general, limited by the wavelengths accessible with the laser, but can be optimized within that range. In addition, of course, the signal is proportional to the gas concentration, but since the main aim of the development of highly sensitive techniques for trace gas detection is to be able to detect low concentrations, the case of maximizing the gas concentration as a part of the optimization procedure is not considered here.

The situation becomes more fiddly when it comes to the pressure of the gas, the interaction length, and the modulation and demodulation parameters included in Eq. (6.3), i.e. the optimum choice of modulation frequency, modulation index, detection phase, and, in particular, the optimum combination of all of them. While the gas pressure will increase the signal for small pressures, for intermediate pressures the signal will level off (primarily due to pressure broadening) and eventually decrease for high pressures. However, in order to reduce the complexity of this topic, this chapter focuses without loss of generality on the case of pure Doppler broadening[3], since in this limit the signal is proportional to the pressure; the pressure-dependence can then be excluded from the discussion. Due to all of this, the discussion here is limited to the entities included in the NICE-OHMS line shape function, together with the length of the cavity, L. The case when also pressure broadening is present is considered in **publication X**.

Figure 6.2 shows simulated 3D-plots of the peak-to-peak value of the Db-NICE-OHMS line shape function as a function of the modulation index, β, and the ratio of the modulation frequency and the Doppler width, i.e. $\nu_{\mathrm{m}}/\Gamma_{\mathrm{D}}$, of a transition, for the absorption (panel [a]) and the dispersion modes of detection (panel [b]). It can be seen that for any given β there is an optimum choice of modulation frequency [26]. In addition, it can also be seen that for any given $\nu_{\mathrm{m}}/\Gamma_{\mathrm{D}}$ ratio, there exists an optimum choice for β, indicated by the red crest line. To maximize the NICE-OHMS signal, the experimentalist should, whenever possible, strive to reside in the vicinity of this line. The two crest lines for absorption and dispersion phase are also plotted in Figure 6.3, as a function of the normalized modulation frequency, by the dark blue and light blue curve, respectively. These two curves thus illustrate the maximum peak-to-peak value the NICE-OHMS line shape function can take for the absorption and dispersion modes of detection for a given modulation index (thus in each case for the optimum β). The figure also shows, by the black curve, the maximum peak-to-

[2]Care has to be taken when a transition can be optically saturated: the more power inside the cavity, the stronger the effect of saturation will be. Nevertheless, as long as one is interested in maximum signal size, one can detect the dispersion mode, which is not affected by optical saturation.

[3]In the work presented in **publication X** three cases are discussed, both the Doppler limit, the case when $\Gamma_{\mathrm{D}} = \Gamma_{\mathrm{L}}$, and, to some extent, the case of pure Lorentzian broadening, where the latter sometimes is an quite adequate approximation for gases at atmospheric pressure. In fact, for a sophisticated analysis of the topic, the pressure as a parameter-to-be-optimized would have to be added.

peak value the NICE-OHMS line shape function can take when additionally the phase is chosen so as to maximize, for each ν_m/Γ_D ratio, the peak-to-peak value of the signal; it can be seen that this response has a broad maximum, where it is above 95% of its globally maximum value, which is between 1.1 and 1.2, within the entire $0.4 \lesssim \nu_m/\Gamma_D \lesssim 2.4$ range.

Example

The analysis of Fig. 6.3 implies that for molecules with a molecular mass of 26 (corresponding to C_2H_2) with Γ_D equal to 240 MHz the modulation frequency is optimally chosen in the 100 to 575 MHz range.

As was discussed above, the modulation frequency in NICE-OHMS has to be equal to an integer multiple of ν_{FSR}, i.e. $\nu_m = k\nu_{FSR}$, where k is the modulation order and where ν_{FSR}, in turn, is given by $c/2L$; hence, ν_m is closely related to the length of the cavity, L. Beyond the findings of the preceding paragraph it is manifested that an increased cavity length, to a first approximation will yield a larger signal, as the interaction length between light and sample will be increased. However, it is worth to investigate this dependence more deeply, since, in fact, a change in cavity length is associated with an alteration of the modulation frequency, as well. Figure 6.4 shows, by the light-blue and dark-blue

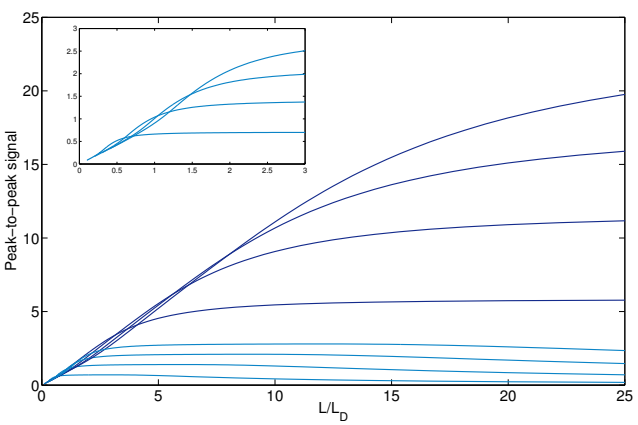

Figure 6.4: NICE-OHMS signal peak-to-peak value in the Doppler limit, represented as $L\bar{\chi}_{NO}^{Db,pp}/L_d$, as a function of the normalized cavity length, for absorption (upper set of curves, dark blue) and dispersion mode of detection (lower set of curves, light blue). The four curves in each set mode correspond upwardly to $k = 1, 2, 3$, and 4.

curves for the absorption and dispersion phase, respectively, the behavior of the NICE-OHMS signal, represented by $L\bar{\chi}_{NO}^{Db}/L_D$, as a function of the normalized cavity length, given by L/L_D, where L_D is given by $c/(2\Gamma_D)$ and referred to as the characteristic cavity length. The four curves in the two sets display the

behavior for four different modulation orders, i.e. for $k = 1, 2, 3$, and 4, thereby representing the cases of modulation at multiples of the FSR; the lowermost curve in each set corresponds to $k = 1$. It can be seen that the absorption and dispersion phase differ in their behaviors. The lowermost curve for the dispersion phase levels off (deviates from linear behavior) for $L/L_{\mathrm{D}} \approx 0.35$ and successively converts to a flat response before it slowly decreases. This shows that for the dispersion mode of operaton it is clearly beneficial to switch to the next modulation order, i.e. $k = 2$, corresponding to a modulation at twice the cavity FSR already for L/L_{D} around unity, for which the situation is similar for a further increasing cavity length. For the absorption mode of detection, in contrast, the response continues to increase even for the lowest modulation order up to L/L_{D} of around 2.6, before it deviates from linear behavior. First at values above 5 the signal size becomes significantly increased for a switch to the next modulation order. Another, maybe less important, but still interesting fact is that for large ratios L/L_{D} and a given modulation order the absorption phase becomes independent of the cavity length, while the dispersion phase decreases with L/L_{D}, roughly as $1/L$ [48].

Example

A typical transition of acetylene (C_2H_2) in the 1.5 µm region has a Doppler width Γ_{D} of around 240 MHz and thereby a characteristic cavity length of $L_{\mathrm{D}} \approx 63$ cm. This implies that the response of the dispersion phase starts to level off already for a cavity length of 22 cm. The corresponding length for the absorption mode of detection is around 160 cm. However, significant differences between the various curves are only present for values of L/L_{D} above unity for the dispersion mode of detection and 5 for absorption, which correspond to cavity lengths of around 60 cm and 3 m, respectively, of which the latter is a rarely realized resonator length. This illustrates that the use of higher than unity modulation orders is of particular importance for the dispersion mode of detection.

6.3 Sub-Doppler NICE-OHMS

The optical resonator in NICE-OHMS can give rise to counter-propagating waves with large intra-cavity intensities, so that transitions with a large dipole moment can be saturated, yielding sub-Doppler (sD) NICE-OHMS signals that can be observed on top of the Db-NICE-OHMS signal [4]. These signals appear whenever two counter-propagating modes of the FM spectrum interact with the same velocity group of molecules.

Figure 6.5 shows NICE-OHMS signals at absorption (left panel) and dispersion phase (right panel) taken with a modulation index of 2.2, which gives rise to a broad FM spectrum, which the modes 2, 3, 4, and 5 have the highest intensities, causing several sD-NICE-OHMS to appear. The center sD signal, which arises from the carrier-carrier interaction, is only present for the dispersion mode. sD signals appear at both detection phases for all frequency detunings of $\pm q\nu_{\mathrm{FSR}}/2$, where q is a positive integer, i.e. 1, 2, 3 etc. For sD

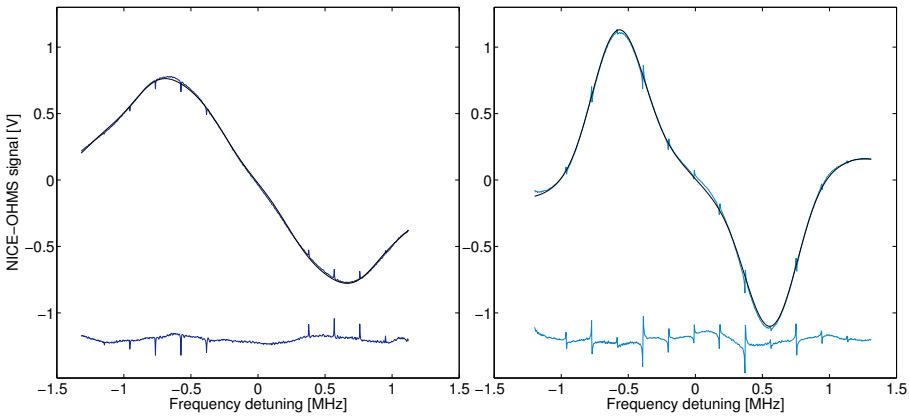

Figure 6.5: SD-NICE-OHMS signals on top of Db-NICE-OHMS signals in the Doppler regime for absorption (left panel) and dispersion mode of detection (right panel). The black line shows a fit of the Eq. (6.1) to the data, where the lowermost line in each panel is the residual of the fit, for illustrational purposes enlarged by a factor of two. The modulation index was chosen to be 2.2 giving rise to a broad FM spectrum, visible by the multitude of sD signals that can be clearly seen in the residuals. Note the absence of the center sD signal in absorption phase.

line shape expressions and further explanations the reader is referred to the detailed surveys on this topic in the Refs. [4, 26].

7 Limits of Concentration Assessment

7.1 Statistical tools and definitions

All assessments of a physical quantity by measurement are governed by measurement errors. There are two groups of such errors, systematic and statistical errors [82]. Systematic errors most often arise from conceptual incorrect assumptions or inattentive instrumental procedures during the experiment, e.g. an inaccurate calibration of the measurement instrument or an unconsidered drift of ambient conditions during the experiment. These errors can be hard to reveal, especially if several of them appear at the same time, e.g. when both the calibration gas has an incorrect concentration and an electron gain factor has changed without knowledge of the experimentalist. Having such errors eliminated or minimized, measurements of a physical quantity still scatter around a certain value due to statistical errors, sources of which can be the reading from a finite scale, vibrations of the instrumentation or fluctuation of the quantity itself, to name a few. All this makes it important to present measurement results together with an estimate of the confidence interval.

7.1.1 Classical tools

Statistics provide tools to characterize a distribution of measurement values, such as the standard deviation or standard deviation of the mean. A set of N measurement values, x_n, that are random and uncorrelated, i.e. have a white spectrum, will have a normal distribution around the expected value, μ, see Figure 7.1. The standard deviation, σ, given by

$$\sigma = \sqrt{\frac{\sum(\bar{x} - x_n)^2}{n-1}}, \tag{7.1}$$

can then be used to specify confidence intervals of a single measurement, so that the result of the measurement can be given as $\mu = \bar{x} \pm \sigma$, where $\bar{x} = \sum x_n/N$ represents the mean value of the data. For the particular and important case

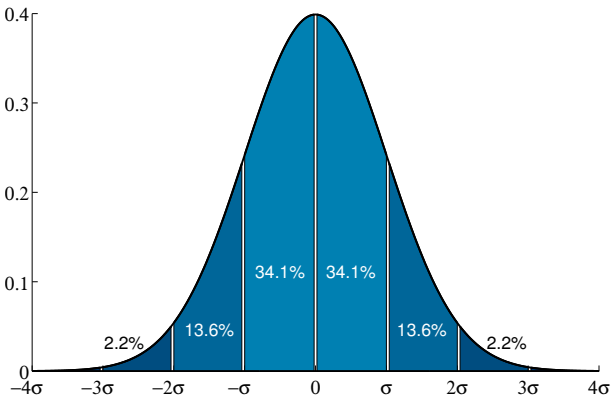

Figure 7.1: Gaussian distribution for $\mu = 0$ and $\sigma = 1$. The numbers in the graph give the probability to find a sample in the corresponding region. Note that almost a third of the data is situated outside the 1σ interval [84].

of a white spectrum, and in the absence of systematic errors, this means that the probability that μ can be found within the interval $\bar{x} \pm \sigma$ is given by 68.3%, which is often referred to as the 1σ confidence interval. The probability that μ is situated within the 2σ or 3σ confidence interval, is given by 95.4% and 99.7%, respectively. The latter implies that it is almost certain to find μ within $\bar{x} \pm 3\sigma$. Often measurement results are reported using multiples of the standard deviation of the mean, the latter given by $\sigma_m = \sigma/N^{-1/2}$, as confidence intervals, now indicating the distribution of subsequent measurements of the mean value [83].

These statistical tools start to fail though as soon as the spectrum no longer is white, which for instance is the case if the measurement is affected by a drift. While, in general, averaging of random uncorrelated measurement values of a quantity makes the mean value to an all better estimate of the expected true value, this is no longer the case if a drift is present: after a certain time, the mean value will start to be affected by the disturbance, leading away from the expected value. In such cases, the Allan-Werle plot [85, 86] is a powerful tool to analyze the noise and the stability of a given instrumentation.

7.1.2 Allan deviation and Allan-Werle plots

Originally, D.W. Allan proposed an M-sample variance in 1966 to describe the statistics of atomic frequency standards and to determine the stability of atomic clocks [85]. First when this concept later was set into a more modern context by the use of bias functions by J.A. Barnes, it was given the name "Allan variance" [87]. The first detailed description of how the concept can be employed in the analysis of optical spectrometers was given by Werle et al. in 1993 applied to tunable diode laser absorption spectroscopy (TDLAS) [86]. The nomenclature here follows that of Werle et al. It is about to become common to refer a plot of the Allan deviation for spectroscopic purposes as an Allan-Werle plot.

For an assessment of the Allan deviation, assume again a set of N times-series data, x_n, with $n = 1, ..., N$. This time series can be divided into M sub-groups, each containing $k = N/M$ elements. The mean value of subgroup s

(with $s = 1, ..., M$) is then given by

$$A_s(k) = \frac{1}{k} \sum_{l=1}^{k} x_{(s-1)k+l}. \tag{7.2}$$

Assuming that the data have been collected with equal time intervals, Δt, the Allan deviation for a given averaging time $\tau = k\Delta t$ can be expressed as

$$\sigma_A(\tau) = \sqrt{\frac{1}{2(M-1)} \sum_{s=1}^{M-1} [A_{s+1}(k) - A_s(k)]^2}. \tag{7.3}$$

This shows that the Allan deviation constitutes the square root of half of the mean value of the squares of the differences between the mean values of two subsequent sub-groups.

Example

To illustrate the use of Allan-Werle plots, sets of data were simulated with $N = 10^4$ according to $x_n = \bar{G}(\sigma) + bn + \bar{S}$, where $\bar{G}(\sigma)$ represents noise with a normal or Gaussian distribution with standard deviation σ, b is a linear drift coefficient, and $\bar{S}$ is a sinusoidal drift component. Figure 7.2 shows the Allan-Werle plot of five different data set simulations: (1) a purely random distributed set of data with $\bar{G}(\sigma = 1)$ and no other contributions, (2) the same as the previous but with a linear drift ($b = 0.002$), (3) the same as the previous, but with a ten times stronger drift ($b = 0.02$), (4) the same as previous ($b = 0.02$) but with ten times larger noise amplitude [$\bar{G}(\sigma = 10)$], and (5) the same as the first, but with an additional sinusoidal drift component $\bar{S}(n) = 5[\sin(20\pi n/N)]$.
In optical spectrometers the five scenarios can possibly correspond to (1) a perfectly optimized system that is only affected by white noise, (2)-(4) systems with different noise levels that are additionally affected by drifts that can for instance be caused by accidentally changing the amount of the sample analyte or changing the amplification levels in detection electronics, and (5) a system that is affected by an etalon that is drifting with time.

Figure 7.2 shows the Allan-Werle plot of the simulated data (i.e. the Allan deviation) from the above example. Curve (1) is decreasing for all averaging times τ with a slope proportional to $\tau^{-1/2}$ indicating a white noise spectrum. The Allan deviation of set (2) follows that of set (1) up to an averaging time of around 60 relative time units, at which it starts to be affected by the linear drift resulting in an upward sloping Allan deviation that is proportional to τ. Curve (3) starts to deviate from curve (1) towards a linear drift behavior already after ten relative time units due to the ten times stronger drift component in the corresponding data set. Curve (4) is for short averaging times a factor of ten higher than curve 1 due to the ten times stronger noise component; it starts to bend upwards after around 50 relative time units, before finally overlapping with curve (3), the data of which having the same drift parameters. Curve (5), corresponding to the set of data affected by a sinusoidal drift but otherwise identical to set (1), first decreases with $\tau^{-1/2}$ as well, before it starts to lift and

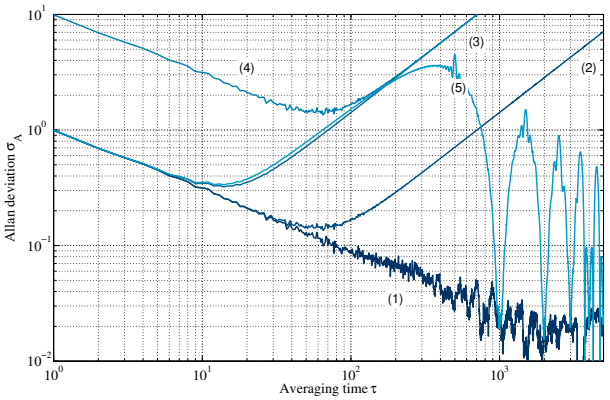

Figure 7.2: Allan deviation for a five different sets of data with different noise and drift characteristics. A slope proportional to $\tau^{-1/2}$ corresponds to white noise, while a τ slope indicates a linear drift. See text for details.

pass a maximum, before returning to the Allan deviation of set (1) again for an averaging time equal to the period of the drift, T, in this case equal to 10^3, where the sinusoidal influence is averaged out; moreover, curve (5) returns to curve (1) for averaging times equal to multiples of T. From curve (5) it can be seen that for $\tau \ll T$ even a sinusoidal drift can appear as a linear drift; it is therefore important to ensure a data acquisition time that is sufficiently long to distinguish between the two cases.

7.1.3 Standard deviation vs. Allan deviation

Since the standard deviation can be used to derive the detection limit of an instrument (see chapter 7.1.4), it is important to understand under which conditions it can be excerpted from the Allan deviation [88]. The definition of the standard deviation assumes a random uncorrelated set of data, wherefore a white spectrum has to be ensured. It has become clear from Figure 7.2 that white noise is indicated by a slope of the Allan deviation proportional to $\tau^{-1/2}$. As soon as the Allan deviation leaves this behavior, the averaging time is too large in order to guarantee a normal distribution of the measurement data.

As an illustration of this, i.e. how the standard deviation compares to the Allan deviation, the latter was calculated for a set of data ($N = 10^4$, taken with an acquisition rate of 1 Hz) with a slope parameter $b = 0.001$ and $G(\sigma = 1)$; the resulting Allan-Werle plot is shown in Fig. 7.3. The plot clearly indicates that there is a drift that becomes significant after around 100 relative time units, corresponding to 100 data points, in general also referred to as $\tau_{\min}$. Up to that time the data has a white-noise behavior.

In order to investigate the behavior of the standard deviation, first only the initial 100 data points of this data set were analyzed. Since the Allan-Werle plot shows that the drift sets in at around 100 time units, this data subset is assumed to primarily show a white noise distribution. This subset of data was then analyzed by the use of various integration times, τ. For each τ, the data in this subset was divided into $100/\tau$ packages. The standard deviation of the means of these packages was then calculated (indicated as circles in the Allan-Werle

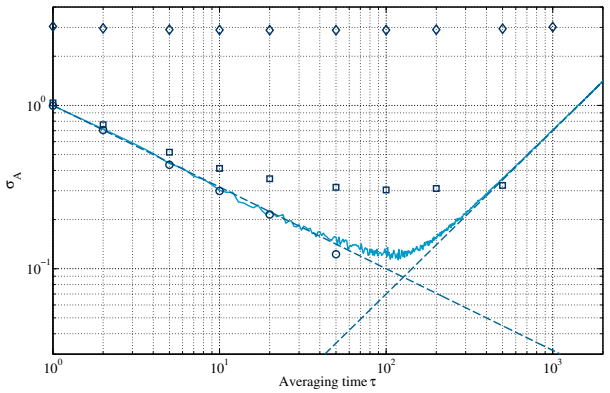

Figure 7.3: Comparison of the standard deviation (open markers) and Allan deviation (continuous curve) for the same set of data and two different maximum averaging times, i.e. 10^2, 10^3, and 10^4 relative time units. The dashed lines indicate white noise and linear drift behavior of the Allan deviation, respectively. See text for details.

plot)[1]. It can be seen from the plot that the standard deviation agrees with the Allan deviation. This is exactly how it should be, as for averaging times $\tau < 100$ the data set has a white spectrum and is not affected by the drift.

The situation becomes different when the same analysis is performed on a larger subset of data. The square markers in the figure represent the standard deviations of the means of data packages for a total data set of 1000 points. It can here be seen that the standard deviation is affected by the drift already for short averaging times: it deviates from the Allan deviation. If the analysis is performed on the entire set of data, i.e. with a length of 10^4 data points (indicated as diamonds in the plot), already the standard deviation for the shortest integration time, $\tau = 1$, is governed by the drift and takes approximately the same value as the Allan deviation takes for $\tau = 10^4$. Therefore, in all cases where a subset of length larger than $\tau_{\min}$ is investigated, the standard deviation is larger than the optimal one and should preferably not be used.

In this sense, the Allan deviation should be the preferred method of data analysis. It allows for convenient assessment of white-noise regions and present drifts. As long as the Allan deviation is decreasing according to $\tau^{-1/2}$, the data set has a normal distribution and the Allan deviation can be used as an estimate of the error. The maximum averaging time is given by the time for which the Allan deviation bends away from the white noise slope; in Figure 7.3, this is in fact already the case for $\tau_{max} \approx 40$ (and not after 100 time, as assumed above). It is often overlooked that if a measurement has to be performed by both a measurement of the actual signal and a corresponding background, it has to be ensured that both measurement are performed within τ_{max} in order not to be affected by a drift.

7.1.4 Detection limit

In the past, various definitions and interpretations of the detection limit have been around, leading to different numerical values for the same instrument or even the same set of data and very much to inconvenience of the scientific

[1]Since only 100 data points were considered, the maximum averaging time was 50 time units (half of the points in the data subset).

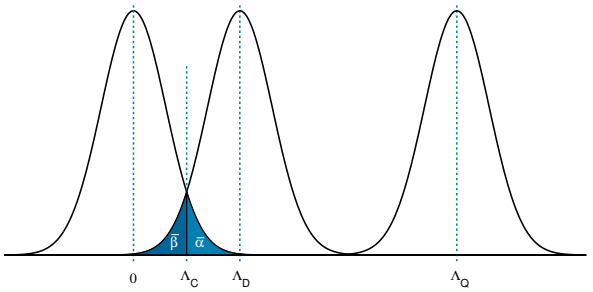

Figure 7.4: Illustration of the terms decision limit (Λ_C), detection limit (Λ_D) and quantification limit (Λ_Q). The variables $\bar{\alpha}$ and $\bar{\beta}$ stand for the probability to detect false positives and false negatives, respectively.

community [83, 89]. In order to set a common standard, both the International organization of standards (ISO) and the International union of pure and applied chemistry (IUPAC) prepared coordinated concepts [90–92], which provide a definition of the detection limit and related terms based on statistical hypothesis testing and the probability $\bar{\alpha}$ of detecting false positive or the probability $\bar{\beta}$ of detecting a false negative. Default values for $\bar{\alpha}$ and $\bar{\beta}$ are suggested to be 0.05. In the following, $\hat{\Lambda}$ represents the estimate of an analyte amount or concentration, with a true value of Λ. IUPAC defines the critical value, Λ_C, for a detection decision as

$$P(\hat{\Lambda} > \Lambda_C | \Lambda = 0) \leq \bar{\alpha}. \tag{7.4}$$

Given a blank sample, this is to say that the probability to detect a false positive is less than $\bar{\alpha}$, by default 5%. Similarly, the minimum detectable value, the detection limit, Λ_D, is defined via

$$P(\hat{\Lambda} \leq \Lambda_C | \Lambda = \Lambda_D) = \bar{\beta}. \tag{7.5}$$

This means, given a sample with a true amount or concentration of Λ_D, the probability to detect a false negative, i.e. to predict the absence of an analyte, is equal to $\bar{\beta}$, by default 5%. In addition to this, the quantification limit , i.e. the smallest quantifiable value, is defined as

$$\Lambda_Q = k_Q \sigma_Q, \tag{7.6}$$

where σ_Q stands for the standard deviation of $\hat{\Lambda}$ if $\Lambda = \Lambda_Q$ and k_Q is by default equal to 10. These cases are illustrated in Figure 7.4.

If the distribution of $\hat{\Lambda}$ is normal with a standard deviation of σ_0 and constant over the range of cases when $\Lambda = \Lambda_C, \Lambda_D$ and Λ_Q, the decision limit, the detection and the quantification limit are given by

$$\Lambda_C = 1.645\sigma_0, \tag{7.7}$$
$$\Lambda_D = 2\Lambda_C = 3.29\sigma_0, \text{ and} \tag{7.8}$$
$$\Lambda_Q = 10\sigma_0, \tag{7.9}$$

respectively.

In many works the critical value Λ_C (or even worse σ_0) is taken as a value for the detection limit. This implies that only the $\bar{\alpha}$-error (the probability of

detecting a false positive) is taken into account. At the same time, the $\bar{\beta}$-error (false negative) becomes 50%, as can be seen from Equation (7.5) by setting $\Lambda_D = \Lambda_C$ [89].

This shows that it is important to use the term "detection limit" with care. Definitions that differ from the one above, in particular those not based on statistical methods, should be entirely avoided [83]. Unfortunately, it is common among spectroscopists coming from physical or technical disciplines to use σ_0 as a value for the detection limit. If doing so – in order to avoid confusion – one should explicitly cite it as the 1σ detection limit. Spectroscopists using absorption spectrometry also commonly use the term "detection sensitivity" when describing the smallest detectable amount of absorption in different units, e.g. as $\Delta I/I$ (dimensionless) or α_0 (either in units of cm^{-1} or under white-noise limited conditions in units of $\mathrm{cm}^{-1}\mathrm{Hz}^{-1/2}$). If so, it should always be clearly defined.

7.2 Shot-noise – a natural limit of detection

With the above formalism one is well-equipped for the assessment of noise and drift levels in systems and for an attempt to identify, minimize, and eliminate their sources, thereby overcoming a series of technical limitations that prevents the experimentalist from reaching the shot noise limit. Examples for such technical limitations are alluded to in chapter 3.3; common to all of them is that they disturb the balance of the FM mode-spectrum, thereby deteriorating the immunity against laser-cavity jitter of NICE-OHMS. However, even having both noise levels and background signals decreased and under control, the shot-noise level constitutes a natural limit of detection with spectroscopic systems.

The shot-noise arises from the discrete nature of light [2] and the associated discrete interaction between photons and an absorber. For NICE-OHMS, the shot-noise limited absorption (for a signal-to-noise ratio of one [i.e. $S/N = 1$]) is given by [2, 4]

$$\alpha_0 L|_{\min} = \frac{\pi}{2F}\sqrt{\frac{e\Delta f}{\eta_c P_0}}\frac{1}{\max\left[\bar{\chi}_{\mathrm{NO}}^{\mathrm{Db}}(\nu_d, \theta_{\mathrm{fm}}, \beta, \mathrm{G})\right]}, \tag{7.10}$$

where e is the electron charge (C), Δf the detection bandwidth (Hz), η_c the detector responsively (A/W), P_0 the power incident on the detector (W), and $\bar{\chi}_{\mathrm{NO}}^{\mathrm{Db}}$ the NICE-OHMS line shape function as defined in Eq. (6.3). The first factor in Eq. (7.10) accounts for the cavity-enhancement, the second, i.e. the square root, represents the shot-noise limit for DAS, and the third contains the effect of the frequency modulation, represented by the normalized NICE-OHMS line shape function. Note that this formulation of the shot-noise level differs (primarily by half of the last factor) from the formulation given in earlier NICE-OHMS articles, due to a different definition of the NICE-OHMS signal, i.e. Eqs. (6.1)–(6.3), and a differently assumed S/N-level.

Example

Let us consider a spectroscopic experiment with a laser power of $P_0 = 1\,\mathrm{mW}$ (incident on the detector), a detector responsivity $\eta_c = 1\,\mathrm{A/W}$ and a detection bandwidth, Δf, of 1 Hz. The shot-noise limit for DAS under these conditions is 2×10^{-8}. The use of an optical resonator with a finesse equal to 10^5 decreases this limit down to 3×10^{-12}. However, these numbers are orders of magnitudes below what can be achieved in practice; for DAS commonly achieved detection limits reside in the 10^{-3} range [2]. Applying a frequency modulation layer and, in the absence of noise introducing background signals, detection close to the shot noise limit can be reached. In a similar way, the CE-shot noise level can be obtained by NICE-OHMSdue to its combination of frequency modulation and cavity enhancement.

Equation (7.10) demands some notes, as also was alluded to in [4]: In fact, this formula is valid only under the assumption that the laser frequency is on resonance with an absorber transition. However, since typically concentration assessments are performed through scans over the entire line shape profile and a successive fits of an analytical expression to it, for most accurate estimation, also the dead-time, i.e. the time spent off resonance, has to be considered. This increases the shot-noise limit to values above that given by Eq. (7.10). It is also worth to note that the shot-noise limit for FMS is larger than that for DAS, which can be understood by the fact that the intensity, which for DAS only resides in the carrier, is distributed into sidebands in the case of FMS.

8

Experimental Details

8.1 Fiber-laser-based NICE-OHMS

8.1.1 Basic setup

The core of FL-NICE-OHMS [32] is an erbium-doped dibtributed-feedback-laser pumped fiber-laser (EDFL, Koheras Adjustik E15) that emits light within a temperature-controllable wavelength range of 1530.8 nm to 1531.8 nm, a maximum output power of 14 mW, and a free-running linewidth over 100 µs of 1 kHz. The frequency of the EDFL can be modulated by a PZT tuning stage inside the laser with a bandwidth of up to 30 kHz and a modulation amplitude of around 3 GHz. The output fiber of the laser is of polarization-maintaining (PM) type, as are all fibres used in the experiment, unless specifically stated, and it is connected to the input of a fiber-coupled AOM (AA Opto-Electronic, MT110-IR25-3FIO) [45], whose first order output is, in turn, connected to the input of a fiber-coupled EOM (General Photonics, LPM- 001-15). The light transmitted through the EOM is coupled into free-space (FS) with the help of an fiber collimator, where it passes a polarizer (P), a half-waveplate ($\lambda/2$), a mode matching lens with a focal length of 1000 mm, a polarizing beam splitter cube (PBSC), and a quarter-waveplate ($\lambda/4$). Alignment to the optical resonator is achieved by two incoupling mirrors. The two mirrors (Layertec) of the resonator are glued to PZTs (Pickelmann Piezomechanik GmbH, HpSt 150/20-15/12 and HpSt 150/20-15/25) that are separated from each other by a Zerodur spacer (Microbas AB). The length of the resonator was initially adjusted with two Macor spacers between the PZTs and the Zerodur spacer. The properties of the two cavities in use are given in chapter 8.1.5. The cavity-transmitted light was redirected and focussed on a large bandwidth photo-receiver (NewFocus, 1611). The light in cavity-reflection was deflected by the combination of the quarter-waveplate and a PBSC onto another large bandwidth photoreceiver (of the same type as that in cavity-transmission). The setup is schematically depicted in Fig. 8.1 and pictures of the system are shown in Fig. 8.2. In order to supress contributions from background etalon fringes, the fiber collimator, cavity, the

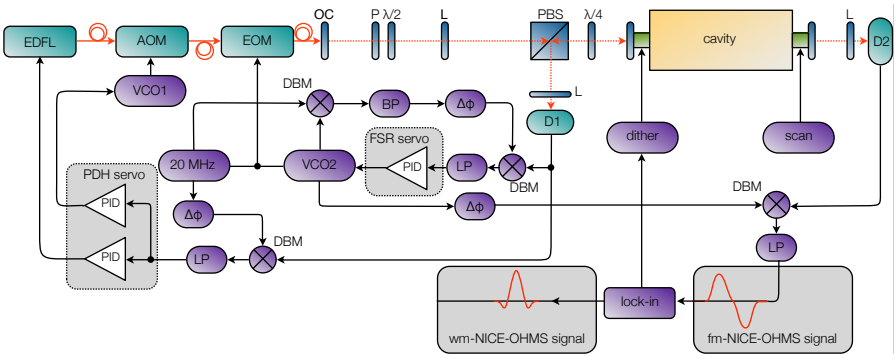

Figure 8.1: FL-NICE-OHMS setup. Electro-optic components, green elements: fiber laser (EDFL), acoustic and electro optic modulators (AOM/EOM), detectors (D1/D2). Optics, blue shaded: fiber collimator (OC), polarizer (P), half-wave plate ($\lambda/2$), mode-matching lens (L), polarizing beam splitter cube (PBS), quarter-wave plate ($\lambda/4$). Electronic components, violet: voltage controllable oscillators (VCO1/2), PDH frequency source (20 MHz), bandpass filter (BP), low-pass filters (LP), double-balanced mixer (DBM), phase shifter ($\Delta\phi$), lock-in amplifier (lock-in), triangular scan generator (scan), servo electronics (PID). This experimental realization was used for the measurements performed in **publication IV** [45]. It should be noted though that minor changes, especially to the optical path, were implemented for some of the other investigations, e.g. the insertion of attenuators, isolators, or additional polarizers.

beam-splitter, and the two detectors are spaced by etalon-immune-distances (EIDs), i.e. integer multiples of the cavity length [43, 50].

The frequency of the laser was locked to a longitudinal cavity mode by the PDH technique [73]. For this, the light was modulated at a frequency, ν_{PDH}, of 20 MHz and with a modulation index of 0.2 by sending a sinusoidal RF voltage from a fixed frequency source (NewFocus, 3363- B) to the EOM. The arising beat-note was detected by the reflection detector (D1). The RF output of the detector was connected to a double-balanced mixer (Minicircuits, ZLW-1), which was also fed with a phase-adjustable reference local oscillator signal for demodulation. The low-pass filtered mixer output contained the PDH error signal, which was then further filtered with servo electronics to match the criteria for a stable feedback system, before it was sent to both the PZT tuning stage of the laser (via a PZT amplifier [Pickelmann Piezomechanik GmbH, ST-150]) and the voltage-controlled-oscillator (VCO1, Mini-Circuits, ZOS-150) connected to the AOM via a 2-watt high-power amplifier (Mini-Circuits, ZHL-1-2 W).

Another modulation at a frequency, ν_{m}, equal to the FSR of the cavity, i.e. 381 MHz, was applied to the light to perform frequency modulation spectroscopy (FMS). For this, the signal from another voltage-controlled oscillator, VCO2, was sent to the EOM, which, due to its compact dimensions, has a broadband response, and is susceptible to both modulation frequencies, i.e. ν_{m} and ν_{PDH}; experimentally this is done by combining the two signals by the reverse use of a splitter (Minicircuits, ZFSC-2-1). Since the FSR of the cavity changed slightly during a scan over a molecular transition (due to changes in cavity length), this

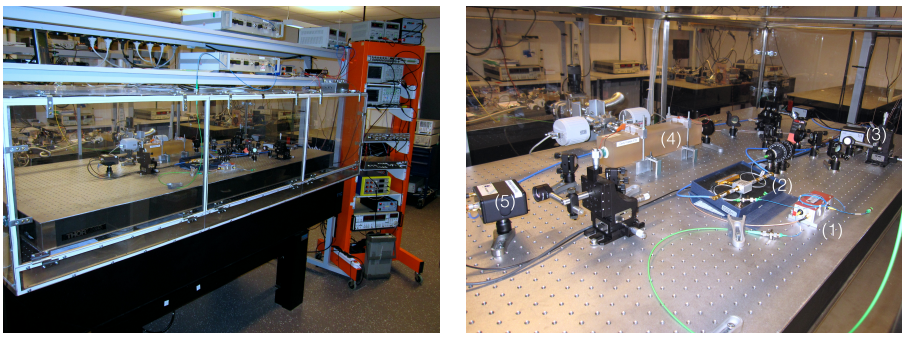

Figure 8.2: FL-NICE-OHMS setup. The left picture shows an overview over the entire instrument. Foreground: floating optical table encapsulated by a Lexan-box (see chapter 8.1.3; all optics are placed on a breadboard which stands passively damped on the floating table. Outer right: rack with supply and control electronics; putting as much electronic devices as possible close together reduced the amount of 50 Hz oscillations and overtones in the system significantly. Center top: two fiber-lasers on the shelf. The optical part is enlarged in the right picture: (1) AOM, (2) EOM, (3) reflection detector, (4) cavity, and (5) transmission detector.

modulation frequency had to be actively locked to the FSR. This was done by the deVoe-Brewer method [81], in which an error signal is derived in the same manner as the PDH error signal, in this case by detecting the beat-note at $\nu_{\mathrm{m}} - \nu_{\mathrm{PDH}}$, i.e. at around 361 MHz. After filtering, the deVoe-Brewer error signal is sent to VCO2.

The NICE-OHMS signal is derived from the beat-note in the output of the transmission detector (D2) by demodulating the signal with a reference signal from VCO2 and low-pass filtering with a cut-off frequency of 1 kHz. Phase-adjustment of the reference signal allowed for detection of absorption and dispersion signals, as well as any combination of them. The signal from a triangular function generator is fed to one of the cavity PZTs via a PZT controller to scan the laser frequency across a molecular transition. When wavelength modulation is done, which is particularly convenient for detection of sub-Doppler signals, the modulation signal from a lock-in amplifier (Stanford Research Systems, SR830) is sent to the other cavity PZT, i.e. the one not used for scanning the laser frequency over a molecular transition, and the DC component of the demodulated transmission signal is fed to the input of the lock-in amplifier (without additional low-pass filtering at 1 kHz) to extract the harmonic of interest [38].

For the work in **publication XI** the modulation index, β, had to be adjustable up to values of 2.4. To achieve this, the signal from VCO2 was first sent through a variable attenuator (ZX73-2500, Minicircuits) followed by a constant-gain amplifier (ZRL-700, Minicircuits), before it was sent to the EOM. The modulation index could by this be conveniently adjustable by sending a control voltage to the variable attenuator.

8.1.2 A closer look at the AOM frequency control

In recent works, the performance of the PDH scheme for locking of the laser frequency to a cavity mode has been limited by the bandwidth of the frequency tuning input of the EDFL, which due to resonances in the internal PZT at around 33 kHz [26] was restricted to around 10 kHz. In the work in **publication IV** [45] the locking was improved by the implementation of an AOM for external stabilization of the laser frequency.

Info

By applying a sound-wave in the radio-frequency domain to the crystal inside the AOM, the frequency of the light leaving the AOM through its first order output can be shifted by the modulation frequency.

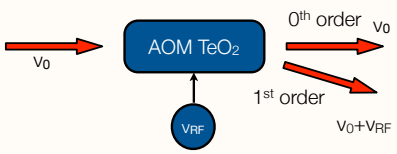

In order to utilize an AOM for mode-locking, the frequency shift has to be tunable. This can be achieved by using a VCO as a modulation source. The PDH error signal can then be sent the VCO to induce a correction of the frequency. The particular AOM in this work had a bandwidth of just below 1 MHz. The architecture of the controller was chosen in the following way: the PDH error signal was split and sent to the PZT of the laser and the AOM frequency control in parallel. The transfer functions of the control electronics were tailored in order to meet the requirements described in chapter 5 and the Bode plot of the controller is shown in Fig. 8.3 (the corresponding schematic can be found in the Appendix). The dark blue curve represents the frequency transfer function (FTF) for the controller part serving the PZT tuning stage of the EDFL, while the light blue curve the one that serves VCO1. Note that both FTFs already include the frequency response of the corresponding system (i.e. the laser and the AOM). Hence, they represent the open loop gain of the two regulating systems. The black curve is the overall FTF, following the FTF of the PZT controller up to a frequency of around 100 Hz, at which the AOM takes over, while it for frequencies above that follows the FTF for the AOM controller; for frequencies above 10 kHz, the overall FTF is pulled slightly downwards due to the fact that the gain of the PZT controller is much smaller than the one for the AOM. Due to intrinsic laser intensity noise in the EDFL at around 300 kHz, the bandwidth of the controller had to be limited to just above 100 kHz to avoid oscillations in this frequency regime. The slope of the FTF was designed to be around -20 dB/decade at frequencies around 100 kHz and the phase to be less than $-180°$ for all frequencies below 400 kHz. The difference in the slopes of the two FTFs (for PZT and AOM locking) at the hand-over point

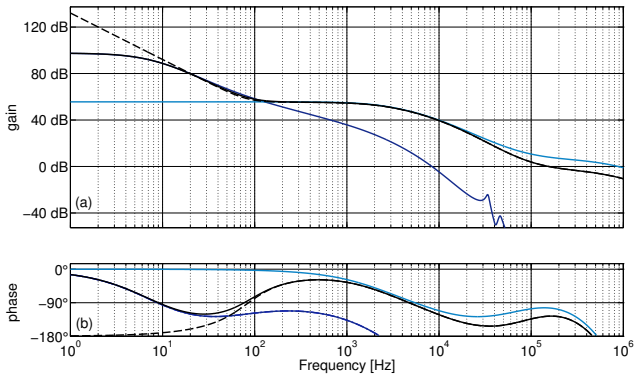

Figure 8.3: Bode plot with gain (panel [a]) and phase development (panel[b]) of the controller for the PDH locking scheme used [45]. The dark blue curve shows the open-loop FTF of the PZT controller including the FTF of the PZT tuning stage itself, the light blue curve the open-loop FTF for the AOM-control system, while the black curve shows the open-loop FTF of the entire system. The dashed curves represent the case when the double-integrating stage is activated.

at 100 Hz was around 20 dB/decade. This implies that the phase difference was marginally above than 90°. Since in the work in **publication IV** [45] it was of particular importance to be able to compare the system performance without and with the AOM-locking scheme, the FTF for the PZT part was stable even when operated separately; in this case, however, the gain had to be decreased so that the bandwidth was restricted to around 1 kHz.

The procedure for locking was as follows: first, the laser was initially locked with feedback to the PZT stage only. After that, the gain in the AOM controller was increased up to the level indicated in the Bode plot. Finally, a gain boost at low frequencies was added by two integration stages in the PZT controller, yielding a gain at 1 Hz of around 130 dB (dashed curves in the Figure).

In order to illustrate the impact of the mode locking, Fig. 8.4 shows, by the upper row, the transmission through the cavity with and without the AOM locking being activated. It can be clearly seen that the noise in the signals was reduced significantly, as a consequence of the reduction of laser-cavity jitter predominantly arising from frequency excursions of the laser at below 100 kHz, as can be seen from Figs. 4 and 5 in **publication IV**. The Figure also shows, by the lower row, two typical NICE-OHMS signals recorded with the AOM controller turned off and on. Even though the impact of the improved locking is visible (see residuals of the curve fits in those figures), the effect is much less than in direct cavity transmission. This is a beautiful demonstration of the noise-immunity inherent to the NICE-OHMS technique[1].

[1]In fact, and in full agreement with theory, the noise-immunity is disturbed the most in the maxima and minima of the signals, as at these locations the FM mode spectrum is most unbalanced, allowing any laser frequency jitter to convert in intensity noise of the cavity transmitted light.

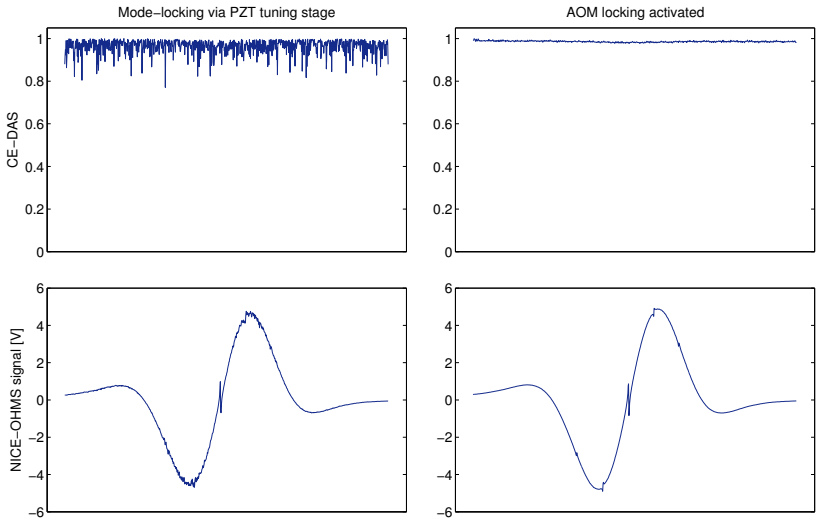

Figure 8.4: Direct cavity transmission (upper panels) for the case with locking solely by feedback to the PZT stage (left column) and with activated AOM locking scheme (right column), recorded with cavity I. The targeted transition is the $P_e(11)$ transition of acetylene and cavity was filled with a 1000 ppm C_2H_2/N_2 mixture at 10 mTorr, giving rise to an absorption coefficient of $2.3 \times 10^{-7}\,\mathrm{cm}^{-1}$, corresponding to a relative absorption, $\Delta I/I$, of 9×10^{-6}.

8.1.3 Environmental isolation

Temperature and noise isolation

As has been alluded to in chapter 7, any measurement will sooner or later be affected by drifts. The lower the white noise level of a measurement is, the larger are the needs of a stable experimental environment. Especially, the aforementioned improved performance of the PDH locking scheme due to the implementation of an AOM made it necessary to provide a more stable environment to the FL-NICE-OHMS. As the main source of drifts were attributed to drifting etalon fringes, an attempt was made to isolate the optical setup from the surrounding atmosphere by the construction of a double-table construction that was encapsulated by a transparent thermoplastic box made of polycarbonate material (Lexan). The double-table construction consisted of a lower floating optical table (TMC, 784-640-12R), on which a 11 cm thick breadboard (Thorlabs, PBI52517/SS-S9) was placed, separated from the lower table by four passive dampers (Thorlabs, PWA071). The Lexan-box insured equal temperature conditions on all sides of the breadboard (including above and below), preventing it from bending due to thermal expansion, and thereby reducing drifts of etalons created between disparate optical components. Moreover, the Lexan-box provided some damping of acoustical disturbances in the air and optical components inside the box.

Isolation of the mains

In order to isolate the system from noise and disturbances from the mains, all electronic devices, except those belonging to the vacuum system, were powered from the same phase through an isolating transformer (Tufvassons, PVM 900) using the coupling scheme shown in Fig. 8.5. The transformer had three connectors on the secondary side, denoted P, M, and N, where the voltage between P and N is equal to the input voltage between P' and N' on the input side, which correspond to the phase and neutral wire of the mains, respectively. The M (mid) connector is not used, but in principle it is providing an electrical potential equal to the average of the potentials at the connectors P and N. Since the potentials at both P and N were floating and it was preferred to have N on an electrical potential of 0 V, the N connector was connected to the main grounding terminal. The use of the isolating transformer significantly reduced noise in the systems. For safety reasons, a connector G was also installed on the secondary side; this had no negative effect on noise levels.

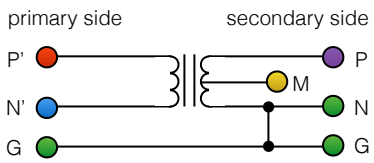

Figure 8.5: Coupling scheme of the isolating transformer (Tufvassons, PVM 900). Note that the absolute electrical potentials on the primary and secondary side are not equal, except the potential of the ground.

8.1.4 Vacuum system

Another important issue for signal stability is the control over the amount of analyte inside the cavity. It is of importance for assessments of the system stability to guarantee constant pressures over several hours. For this reason, a new gas system was installed (see Fig. 8.6, which, on the high-vacuum side, was fully[2] based on conflate (CF) flanges, providing low leaking rates down to 7×10^8 mTorr l/s per flange coupling. These systems are commonly used whenever connection with ultra-high vacuum (UHV) conditions are needed and NICE-OHMS, typically operated down to pressure around 1 mTorr, is far away from that.

The lowest inward leakage rate up to the first valve and against atmospheric pressure was as low as 3 mTorr per day. It should be noted that Copper was completely avoided in the parts of the system that was in direct contact with the cavity gas volume, since the most important target gas, acetylide, reacts with copper, producing copper acetylide (C_2Cu_2). This was of particular importance

[2]The first flange coupling closest to the cavity actually was a KF coupling, which was not possible to remove for the work in **publication IV**. Cavity II was constructed with a CF flange for connection to the vacuum system right away.

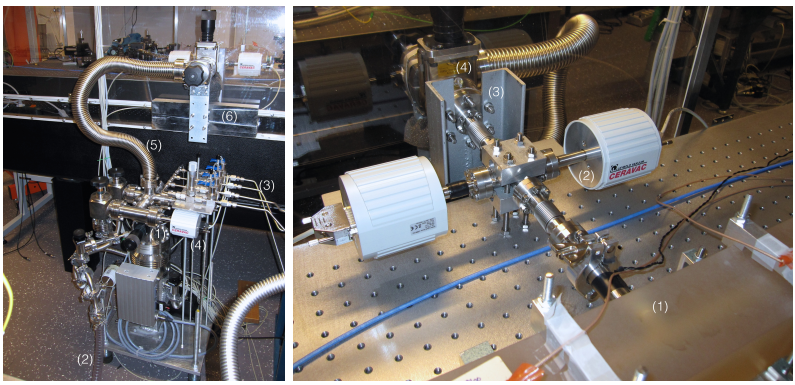

Figure 8.6: Vacuum system. Left picture: (1) turbo molecular pump with control unit, (2) hose supplying fore-vacuum, (3) gas supply lines, (4) capacitive pressure gauge, (5) flexible hose towards cavity unit, (6) anchor mounted on lower optical table for vibration absorption. Right picture: (1) cavity (2) capacitive pressures gauges, (3) vibration-damping anchor mount, (4) copper-free aluminum valve.

for the gaskets and the first valve connected to the cavity which had to be chosen as aluminum gaskets and a copper-free valve (Oerlikon Leybold Vacuum, Miniature UHV Gate Valve, 28684). Most other vacuum parts, e.g. pipes, hoses, or T-pieces could be used as standard parts since they normally made of either aluminum or stainless steel.

For adjustment of the sample pressure a turbo molecular pump (Oerlikon Leybold Vacuum, Turbo MAG W300 iP) is used, which, due to a magnetic bearing of the rotor provided both low-noise and low-vibration conditions. Remaining vibrations were absorbed by mounting the vacuum hose, which connects the cavity and the vacuum system, to the lower table of the double-table construction described in chapter 8.1.3, so that vibrations transferred to the cavity and the upper breadboard are kept at a minimum. The turbo molecular pump was backed up by a rotary vane pump (Oerlikon Leybold Vacuum, Scrollvac SC 5d), which was placed outside of the lab (for noise-reduction) with a hose wall-feed-through. The pressure was monitored both close to the cavity and at the input to the turbo molecular pump by two capacitance pressure gauges at each position (Oerlikon Leybold Vacuum, Ceravac CTR91-1Torr/1000Torr).

8.1.5 Optical cavities

Most measurements were performed with a cavity [26] with a finesse of 5700 (cavity I). However, since the PDH locking scheme incorporating an AOM decreased the laser-cavity jitter to such an extent that it opened for an increase of the cavity finesse, and in order to meet possible future requirements, e.g. in the case of assessment of acetylene in breath, a new cavity (cavity II) was constructed. Both cavities are built around a spacer made of Zerodur (see picture in Fig. 8.7), on which mirrors were glued, separated from the Zerodur

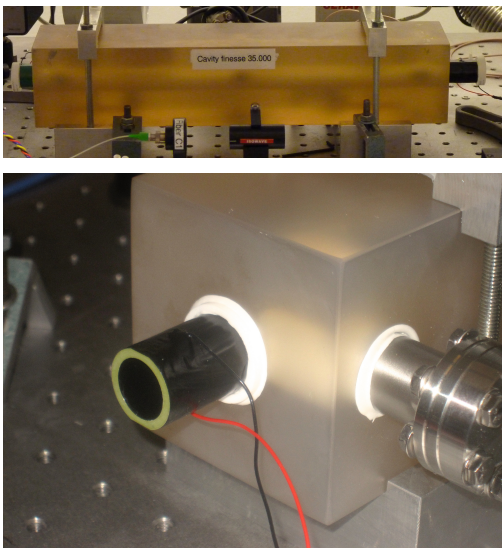

Figure 8.7: Upper picture: optical cavity with Zerodur spacer (yellow). The lower picture shows an enlargement of the cavity input front with a PZT element (black), Macor spacer (white) between the Zerodur bar and the PZT element, and a CF vacuum connection (silver, right). The mirrors are to be glued onto the PZT elements with TorrSeal.

Cavity	F	L_c [cm]	ν_{FSR} [MHz]	Γ_c [kHz]	T_c^{res}	R_c^{res}	κ
I	5700	39.37	381.02	33	90%	1%	1600
II	35000	39.33	381.40	5.4	50%	16%	11000

Table 8.1: Cavity properties of the two optical cavities. F is the finesse, L_c the cavity length, ν_{FSR} the free-spectral range, T_c^{res} and R_c^{res} are the on-resonance transmission and reflection giving the amount of incident power that is transmitted or reflected, respectively, and κ is the intra-cavity power buildup. The values for cavity I are taken from [26].

spacer by two PZT elements (one on each side) and additional Macor-spacers to realize the cavity length that matches the desired FSR. The PZT elements allow for a controllable change in cavity length. The maximum strokes of the input and output PZTs were 30 and 15 µm, corresponding to frequency-shifts of a cavity mode of around 15 and 7.5 GHz and changes in FSR of 30 and 15 kHz, respectively[3]. Cavity II differed from cavity I in the following details: (*i*) the mirror reflectivity was chosen to be larger; (*ii*) the cavity geometry was symmetric, i.e. both mirrors have the same radius of curvature; (*iii*) the bored volume in the Zerodur bar offered two more connections at the side of the bar allowing for the realization of a flow cavity. The most important properties of the two cavities are summarized in Table 8.1.

[3] Assuming a cavity length of 0.395 m and a laser wavelength of 1.5 µm

8.1.6 Fiber-coupled optical circulator

In **publication VIII**, the function of the combination of the quarter-waveplate and polarizing beam splitter cube (PBSC) for the deflection of the cavity-reflected light was replaced by the implementation of a fiber-coupled optical circulator (FCOC) that was coupled in between the EOM and the fiber collimator. The reflection port of the FCOC was connected to a fiber-coupled large bandwidth photodetector (NewFocus 1611). Figure 8.8 shows a picture of

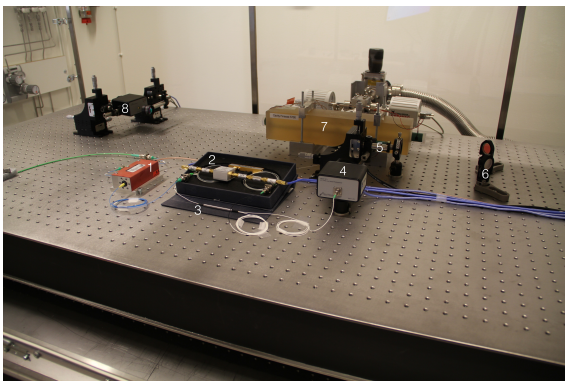

Figure 8.8: Picture of the optical part of the FCOC setup. (1) AOM, (2) EOM, (3) FCOC, (4) reflection detector, (5) fiber collimator mounted on a translation stage, followed by the lens for mode-matching, (6) mirrors for beam alignment, (7) cavity, (8) transmission detector preceded by a focusing lens.

the FCOC setup and is a nice demonstration to which extent the amount of free-space components in NICE-OHMS can be reduced[4].

In the free-space setup described above the combination of the quarter-waveplate and the PBSC provided a good isolation between the cavity mirrors and the fiber collimator, which were the surfaces contributing the most to background etalon fringes. This isolation was no longer present in the FCOC-setup. The insertion of an isolator is, in fact, prohibited since it would not allow the concept to work, because the cavity-reflection has to be directed back into the FCOC. In this configuration it was therefore of particular importance to space the fiber collimator and the cavity input mirror by an EID. To be able to make fine adjustments of the spacing while minimizing the etalon fringes in the NICE-OHMS signal the fiber collimator was mounted on a translational stage. It is worth to note that the optimum position of the mode-matching lens for this particular spacing of fiber collimator and cavity in fact is a few centimeters before the fiber collimator, which obviously is impossible to realize; for this reason the lens was placed as close as possible to the fiber collimator, causing some higher order TEM modes to appear, the strongest one of which was below 5% of the fundamental TEM mode. The noise-contribution in the

[4]In fact, one could go one step further, skip the transmission optics, and instead detect the analyte in cavity reflection, as was done in [40].

reflected light due to these higher order modes was shown to be negligible.

Info

An optical circulator (OC) is a device that has, in its most common realization, three optical ports. Light entering through port 1 will be transmitted through the OC so that it leaves through port 2. This is called the forward direction. In the reverse direction, i.e. when light enters through port 2, it will be redirected in a way that it exits the OC through port 3. There do exist more sophisticated versions with four ports, as well, separating the two modes of polarization in the reverse direction.

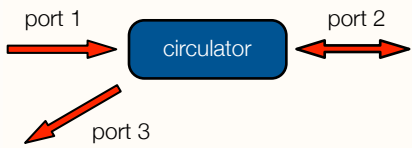

8.2 DFB-laser based NICE-OHMS

In **publication I**, NICE-OHMS was realized in a setup which was based on a distributed-feedback (DFB) laser (NEL, NLK1C6DAAA). The wavelength of the laser was tunable by temperature between 1549 nm to 1555 nm. The fast current tuning, with a bandwidth of around 700 kHz, allowed for a mode-hop-free tuning range of 65 GHz. The line width was stated by the manufacturer to be 70 kHz, determined with a self-heterodyne measurement; in reality, however, and although it was driven by a purposely-made low noise driver, it was found to be significantly larger, as was discussed in detail in [27].

Conceptually, the realization (depicted in Fig. 8.9) was similar to the above described FL-NICE-OHMS setup and is described in detail in [41], but with a few alterations caused by the slightly different behavior of the DFB with respect to that of the EDFL. The three most important changes are: (*i*) the PDH locking was realized by feedback solely by current tuning of the DFB laser, i.e. without using an AOM for frequency stabilization. (*ii*) Since the power of the DFB laser had a strong wavelength dependence, its intensity was stabilized by the use of the 0^{th}-order output of an AOM. An error signal for this was derived from an additional reference detector in front of the cavity. In later works, for an improved manageability of the system the AOM was replaced by an intensity modulator based on an electro-optic crystal. (*iii*) Since the line width of the DFB laser was significantly broader than that of the EDFL, and the upper bandwidth it could be modulated at without excessive phase shifts or noise was larger than the mode width of the cavities used for FL-NICE-OHMS, it was realized with a cavity with a finesse that was one order of magnitude below the one in the FL-NICE-OHMS setup, i.e. to a value of 460.

The main advantage of the DFB-NICE-OHMS setup as compared to the FL-NICE-OHMS setup is the larger scanning range of the DFB laser. While in the case of the EDFL a scan covers at most a frequency range of 3 GHz, it was

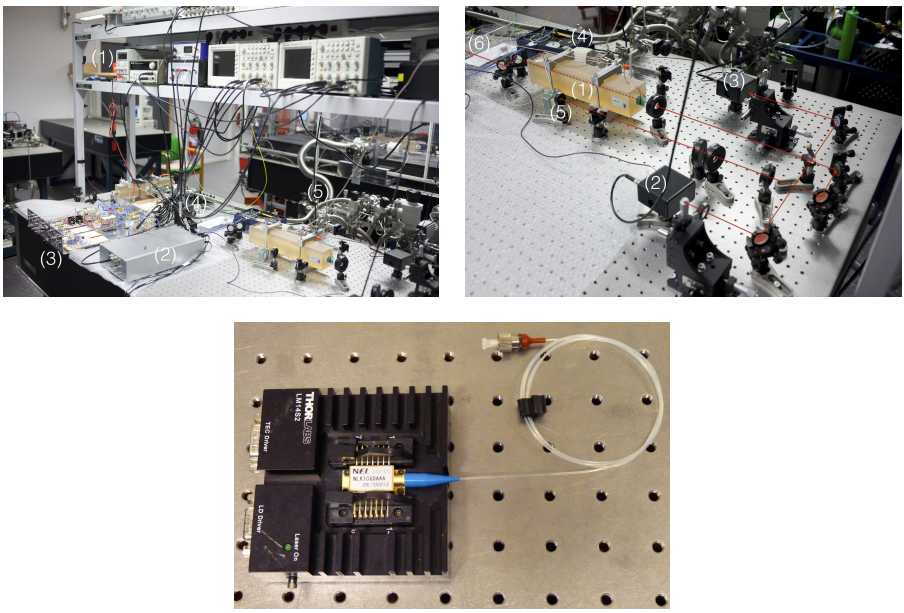

Figure 8.9: DFB setup. The left picture shows an overview with (1) a rack of supply electronics and equipment, (2) Al-shielded RF-electronics, (3) Al-shielded control electronics and passive RF-demodulation components, (4) transmission detector, and (5) vacuum system. The picture to the right shows the optical part of the setup with (1) the cavity, (2) reflection detection, (3) reference detector for intensity stabilization of the light, (4) fiber-coupled EOM, (5) fiber collimator, and (6) intensity modulator; the red lines indicate the laser beam path. ©Chemical Biological Centre KBC, Umeå university, picture by Johan Gunséus, Synk. Lower picture: DFB laser chip with fiber pigtail installed on a butterfly-mount with connectors for current and temperature control.

up to 16.5 GHz in DFB-NICE-OHMS, limited by the maximum stroke of the large cavity PZT. This allows not only for detection of an entire NICE-OHMS signal for cases when collisional broadening significantly widened the signal, but also for the acquisition of several transitions within the same scan, providing equal experimental conditions and thereby allowing for quantitative comparisons of line parameters [41].

As was alluded to above, the laser current control allowed for PDH frequency stabilization with a maximum bandwidth of 700 kHz. At that point the phase developed to more than −180°, so that the bandwidth of the closed-loop system had to be restricted to around 300 kHz. Unfortunately, there was excessive laser frequency noise at frequencies around 450 kHz. The source of this could not be identified, but it was found that it could neither be attributed to intensity noise nor noise from the locking electronics. Due to the limited current control bandwidth this problem could not be corrected for by feedback solely to the current control of the laser. In subsequent experiments it was investigated to

which extent the fiber-coupled EOM could be incorporated for improved locking. For this, in parallel to the feedback to the current control, the PDH error signal was integrated and sent to the RF-input of the EOM. However, it was found that the gain of the EOM only was sufficiently to compensate for frequencies above 1 MHz. Therefore, this approach did not provide a useful means for frequency actuation in the range between 300 kHz and 1 MHz. Despite this problem, the DFB-system provided excellent conditions for investigations of line shape effects as presented in **publications II, V, VI** and **IX**.

9 Results

This thesis is based upon both theoretical and experimental work performed with the main aim of improving the performance of Db-NICE-OHMS, primarily FL-NICE-OHMS but also to a certain extent DFB-laser based NICE-OHMS. The work has, over the years, been presented in a number of publications (**publications I – XIII**, reproduced below). In addition to these, some results have been presented at conferences. The most important contributions to the field are shortly summarized in this chapter. Note though that due to space constraints not all findings can be reported here; for more details, the reader is referred to the publications.

9.1 Reduction of the laser-cavity jitter by external means

In **publication IV** the PDH locking scheme was extended by an AOM for external corrections of the laser frequency, which is described in detail in chapter 8.1.2. For an investigation of the impact of the improved locking scheme on the noise levels of the technique and their impact on the detection limit, an Allan-Werle plot (Fig. 9.1) of the system was assessed for a variety of experimental conditions.

The lowermost black curve illustrates the shot-noise limit for a set of typical experimental conditions present during some typical assessment, i.e. $F = 5700$, $\eta_c = 1\,\mathrm{A/W}$, $P_0 = 700\,\mu\mathrm{W}$, $\beta = 0.36$, $\bar{\chi}_{NO}^{Db}(\nu_d, \pi) = 0.22$ (see Fig. 6.2 for $\nu_m/\Gamma_D \approx 1.6$ and the given β), and $L = 0.39\,\mathrm{m}$. Moreover, as was also alluded to in chapter 7.2, the level was increased by a factor of $\sqrt{6}$ with respect to Eq. (7.10) to account for the time effectively spent on resonance. The resulting shot-noise level is $1.1 \times 10^{-12}\,\mathrm{cm^{-1}\ Hz^{-1/2}}$. Note that this limit is marginally different from the value given in the paper, i.e. $8.8 \times 10^{-13}\,\mathrm{cm^{-1}\ Hz^{-1/2}}$, which did not take the time spent on resonance into account and was based on a different definition shot-noise limit ($S/N = 2$), whereby they differ by a factor of $2/\sqrt{6}$, i.e. by 20 %.

The uppermost (light blue) curve in the plot shows the Allan deviation

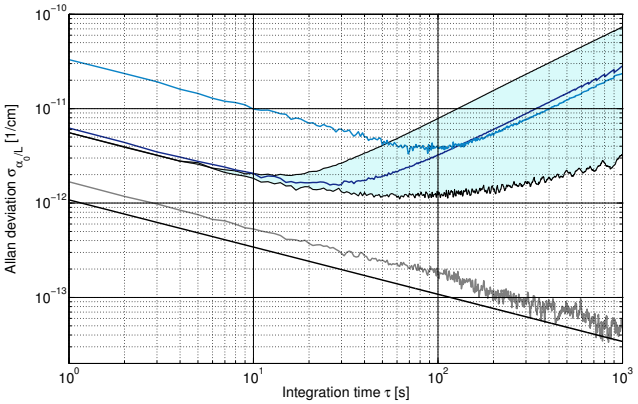

Figure 9.1: Allan-Werle plot of the system performance in terms of the Allan variance of the absorption coefficient under a set of different conditions: PDH locking only by the PZT stage (light blue curve) and AOM scheme activated (dark blue curve); the two black curves bordering the blue area are assessed with only N_2 being present in the cavity with the AOM scheme activated; the gray curve represents the noise contribution from electronic noise, and the black curve is the shot-noise limit for the given experimental conditions. See text for details.

for the case when the system was placed on the Lexan-insulated double-table construction encapsulating the optics but when the laser was locked to the cavity by feedback only to the PZT tuning stage of the laser, and when the cavity was filled with 150 mTorr of 10 ppm C_2H_2 in N_2. The white-noise level in this case is 3.3×10^{-11} cm^{-1} Hz $^{-1/2}$, which for short integration times was about the same as that reported in an earlier work with no encapsulation of the optics and a conventional optical table [43]. In the present case, however, the measurement was virtually not affected by any flicker-noise (i.e. the white-noise regime goes over into the drift regime without a "flicker-noise-floor".); this shows the clear impact of the improved design of the optical table and the environmental insulation by the Lexan-box which is encapsulating the optics. The case when the AOM locking scheme was activated (and again in the presence of analyte) is represented by the dark-blue curve; the white-noise level was here 6.2×10^{-12} cm^{-1} Hz $^{-1/2}$, which is five times below the case above when the AOM scheme was turned off. Since both these measurements were taken directly after each other, the drift behavior is similar, and it can be concluded that the AOM measurements were affected earlier by the drift.

In order to assess the drift behavior of the system, ten measurements on zero gas (N_2) were performed during randomized times during a few days; all Allan-Werle plots reside within the blue-shaded in Fig. 9.1, where the two curtailing black curves display the two measurements with the highest and lowest Allan deviation. Here, a signal strength-to-concentration calibration was performed on 10 ppm C_2H_2 at 150 mTorr. It is clearly visible that the white-noise-level is highly reproducible and slightly lower (5.6×10^{-12} cm^{-1} Hz$^{-1/2}$) compared to

the measurement in the presence of analyte. The type and strength of drifts, however, depend strongly on the particular experimental situation (or, more precisely, the environmental conditions present during the measurement); this fact is particularly important to remember when conclusions about the drift behavior of the system are to be drawn. The gray curve in the Allan-Werle plot shows the noise contribution arising from the demodulation and data acquisition part of the setup. The data for this was acquired in exactly the same way as the zero gas measurements above, but with the detector covered so that no light was impinging.

In some cases it can be of interest to know how much the gas pressure and the presence of an analyte affects the noise-level of a system (Fig. 9.2). The zero-gas noise-level was first assessed for various total pressures and found to be almost pressure-independent up to around 60 Torr, indicated by the blue bar in the lower part of the graph. The noise level of the recorded NICE-OHMS signal, expressed in terms of the shot-noise level, was then recorded in the same manner (but for different pressures of the analyte). This is illustrated as circles in Fig. 9.2. It was found that the presence of an analyte increases the noise-level only marginally up to pressures of around 100 to 200 mTorr, corresponding to an absorption coefficient of 2.5 to $5.0 \times 10^{-8}\,\mathrm{cm}^{-1}$, respectively, while for higher pressures the noise level increases with the amount of absorption. The latter can be explained by an increase in the unbalance of the FM mode spectrum and the accompanying degradation of the noise-immunity in the presence of an absorber. This shows that whenever the noise-level of the system is assessed in the presence of an analyte in the cavity, the amount of absorption should be kept sufficiently low to exclude effects of deteriorated noise-immunity, in our case, using a cavity with length 39.4 cm, preferable below a relative absorbance, $\Delta I/I_0$, of 2×10^{-6}.

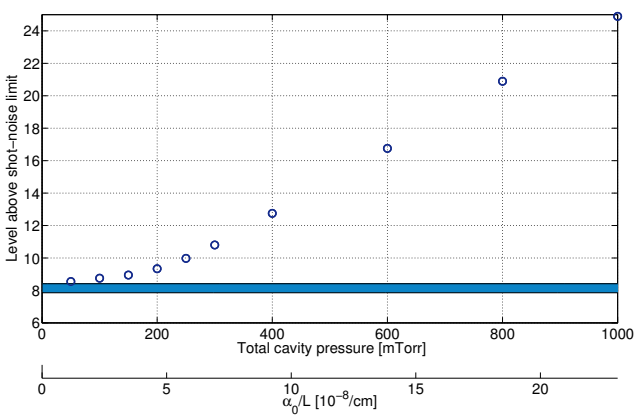

Figure 9.2: Noise level of the instrumentation in terms of the level above shot-noise as a function of analyte pressure (of a 10 ppm C_2H_2/N_2 mixture) or absorption, illustrated as circles. The blue bar at the bottom indicates the pressure-independent noise-level area for zero-gas measurements.

In summary it can be concluded [45] that by the use of an AOM for external frequency stabilization the 1σ detection sensitivity of Db-NICE-OHMS was lowered to around $1.8 \times 10^{-12}\,\mathrm{cm}^{-1}$ for an integration time of ten seconds. The relative absorption, $\Delta I/I_0$, therefore becomes 7.2×10^{-11}. This implies, when extrapolated to the optimum pressure, which is 63 Torr, a detection limit[1] in terms of the concentration of the analyte, C_2H_2, of 4 ppt (0.000 004 ppm).

9.2 NICE-OHMS instrumentation based on an optical circulator

In an attempt to decrease the size of the setup and the number of optical components of FL-NICE-OHMS, and as was described in chapter 8.1.6, the pick-up scheme for the cavity-reflected light was in **publication VIII** replaced by a fiber-coupled optical circulator (FCOC). Figure 9.3 shows, by the uppermost

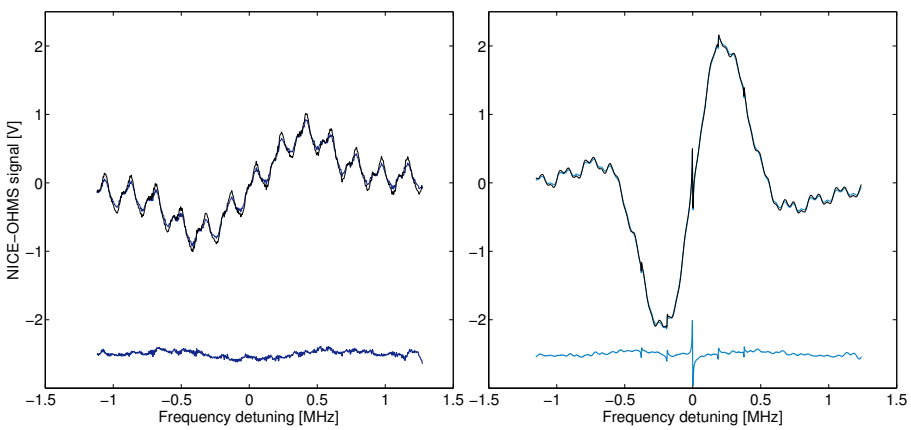

Figure 9.3: NICE-OHMS absorption (panel [a]) and dispersion signal (panel [b]) from a 1000 ppm C_2H_2/N_2 mixture at a pressure of 3 mTorr together with a corresponding fit of a sum of Eq. (6.1) and an expression for the etalon contribution (see text for details). The lowermost curve in each panel represents the residual of the fit.

curves in the left and right panel, a Db absorption and dispersion NICE-OHMS signal, respectively. Even though the position of the fiber-collimator was fine-tuned around an EID (with respect to the cavity mirrors) so as to minimize contributions of etalons[2], the signal was clearly affected by fringes in both detection modes, and stronger in the absorption than the dispersion mode of detection. This is in line with the fact that not all optical surfaces can simultaneously be placed exactly at EID positions and that the contribution

[1] For this particular transition addressed, one expects the largest NICE-OHMS signal size at 63 Torr, where it is approximately 140 times larger than at 150 mTorr, for which the detection limit was assessed.

[2] As explained in chapter 8.1.6 the use of any kind of an isolator between the cavity and the fiber-collimator is prohibited, since it would prevent the cavity-reflected light from re-entering the fiber-collimator.

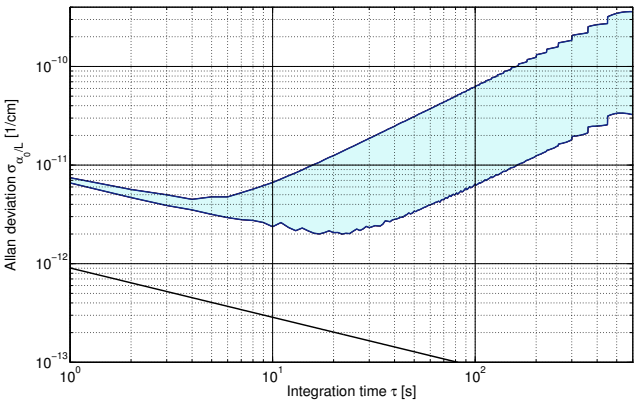

Figure 9.4: Allan-Werle plot for the FCOC version of FL-NICE-OHMS. The upper and lower blue curve represent the two outermost Allan deviation curves out of 10 measurements; the remaining Allan deviation curves lie within the shaded are. The black line indicates the shot-noise limit for the present conditions.

from an etalon in the absorption mode increases faster with detuning from a pure EID condition than in the dispersion mode (compare chapter 3.3).

A Fourier analysis of the two signals revealed that the fringe structure consists of a sum of three contributions from etalons with a spacing equal to one, two, and three times the cavity length. The black curves in the two panels, which almost completely overlie the blue curves, illustrate fits of a sum of Eq. (6.1) and an expression for the etalon contribution (consisting of a sum of three sines with frequencies corresponding to the lengths of the etalons) to the measured data. The lowermost curve in the two panels shows the residual of the corresponding fit.

It is of interest, of course, to assess how the performance in terms of stability of the FCOC version of the setup compares to that of the free-space version of FL-NICE-OHMS. For this, the Allan deviation was assessed in ten time-series measurements of the blank signal in dispersion mode of detection. The result is illustrated in the Allan-Werle plot in Fig. 9.4, where the two blue curves represent the lowest and highest Allan-deviation and where all other measurements are situated within the blue-shaded area. In the same way as above for the free-space setup, a signal strength-to-concentration calibration was performed on 10 ppm C_2H_2 at 150 mTorr. It can be seen that the white-noise level of around $7 \times 10^{-12}\,\mathrm{cm}^{-1}\,\mathrm{Hz}^{-1/2}$ is only marginally larger than the one assessed for the free-space setup and, in the best case, valid up to a 20 s integration time. In the worst case (upper blue curve) the measurement was affected by a drift already after 4 s to 5 s, while this was at the earliest the case around 10 s for the free-space setup. The black line shows the shot-noise limit at $9 \times 10^{-12}\,\mathrm{cm}^{-1}\,\mathrm{Hz}^{-1/2}$, calculated in the same way as for the free-space setup; this limit is slightly lower than the one indicated in Fig. 9.1 due to a slightly larger power impinging on the detector (1 mW in the present case).

It should be noted that in **publication VIII** also the performance of sD NICE-OHMS was assessed, which was slightly worse than the performance achieved with Db measurements. Still, whenever affected by spectral interference with neighboring transitions or with lines of other molecular species, the sD mode of detection could be addressed. This shows that NICE-OHMS can be

realized in a compact manner, i.e. with a minimum of free-space optics, and in particular with a fiber-based circulator.

9.3 NICE-OHMS beyond the triplet formalism – optimum system realization

In **publication X** it was scrutinized how to choose or optimize various system parameters of a NICE-OHMS instrumentation to achieve maximum signal response. The optimization part of this work was to a certain extent described in chapter 6.2.2 above. As a verification of the line shape proposed in that work, which was transferred from the FM technique to NICE-OHMS, especially its dependence on the modulation index and to some extent on optical saturation, a series of NICE-OHMS signals were analyzed in **publication XI** for modulation indices from 0.1 to 2.4 and for the two species acetylene and carbon dioxide. Figure 9.5 shows examples of such signals (by colored curves) for both C_2H_2

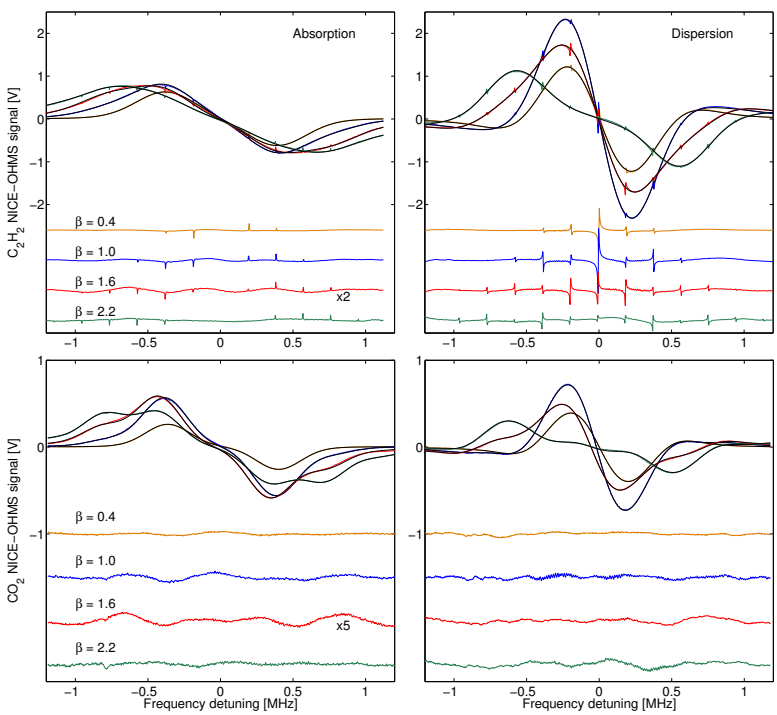

Figure 9.5: Db-NICE-OHMS signals for C_2H_2 (upper panels) and CO_2 (lower panels) in absorption (left row) and dispersion mode of detection (right row) for four different modulation indices, viz. 0.4 (orange), 1.0 (blue), 1.6 (red), and 2.2 (green), together with the corresponding fit of Eq. (6.1) in black. The lower curves represent the residuals of the associated fits, amplified by a factor of two and five for fits to C_2H_2 and CO_2 signals, respectively.

(upper panels) and CO_2 (lower panels), as well as for the absorption (left panels) and dispersion mode of detection (right panels). The black curves represent fits of the theoretical description of Db-NICE-OHMS for arbitrary modulation indices that was present in **publication X**. The lowermost curves represent residuals between the data and the fits. In general it can be concluded that the theoretical description given in that work is appropriate for all modulation indices addressed. Moreover, the description also accounts properly for the effect of optical saturation[3]. Due to the weak line strength of the CO_2 transitions addressed, the unsaturated CO_2 signals are not decreased in size. The appearance of sD signals on top of the Db signals from C_2H_2 alludes nicely to the increasing width of the FM spectrum with modulation index.

Figure 9.6 shows the dependence of the peak-to-peak value of the Db-NICE-OHMS signal on modulation index for the two gases and the two modes of detection. The intracavity power in this experiment was 1.25 W and the saturation power for the transitions addressed was 61 mW and 190 W for C_2H_2 and CO_2, respectively. Hence, the transition addressed in C_2H_2 is strongly optically saturated, while the one in CO_2 is not. The solid lines show the expected behavior of the Db-NICE-OHMS signal due to Eqs. (6.1)–(6.3). It can be seen from the Figure that the measured values follow the predicted curves to a large extent. This figure is thus a verification of not only the theoretical description presented in **publication X**, but also the predictions visualized in Fig. 6.2 [based on Eqs. (6.1)–(6.3)] for ν_m/Γ_d equal to 1.6 and 2.1 for C_2H_2 and CO_2, respectively. It can be concluded that in this particular case both the peak-to-peak signal of the C_2H_2 and the CO_2 series reaches a maximum around $\beta = 1.1$ in dispersion phase. The maximum in absorption phase for CO_2 appears at $\beta \approx 1.4$, while the C_2H_2 absorption phase shows a shallow plateau from $\beta \approx 0.6$ and up. The sharp bends (in all curves except the C_2H_2 absorption curve) appearing at a modulation index of around 2 arises when the contribution from the 2^{nd} order sidebands becomes larger than the contribution from the carrier and the 1^{st} order sidebands (compare for example the transition from the red to the green curve in the lower right panel of Fig. 9.5: while the peaks at around $\pm 1/4$ GHz become smaller with increasing β, the ones at around or slightly above $\pm 1/2$ GHz will increase in size). Another interesting finding in this context is actually that the width of the signals for which one expects the largest peak-to-peak, i.e. around $\beta = 1.1$, is only marginally broader than the width of the signals for $\beta = 0.4$, making a larger-than-normal modulation index attractive even for dense spectra when care has to be taken to prevent interference with adjacent transitions.

It was also found in **publication XI** that the 1σ detection limit of FL-NICE-OHMS (assessed in the dispersion mode of detection) could be decreased from 7.3×10^{-12} to around $4.9 \times 10^{-12}\,\mathrm{cm^{-1}\ Hz^{-1/2}}$ by increasing β from 0.4 to 1.0. This corresponds to an increase in detection sensitivity of around 50%. Since the corresponding increase in signal size is around 80% (as indicated by the dispersion curve for C_2H_2 in Fig. 9.6), it can be concluded that also

[3]Note that these signals were taken in the Doppler limit in order to avoid SDEs and effects from Dicke narrowing. For this reason, the effect of saturation broadening of the collisional width is not visible here.

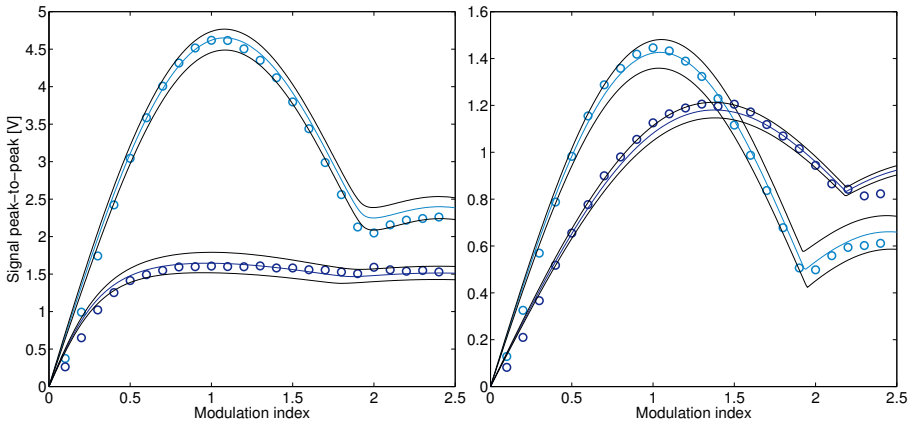

Figure 9.6: Db-NICE-OHMS signal peak-to-peak for absorption (dark blue circles) and dispersion (light blue circles) from C_2H_2 (left panel) and CO_2 (right panel). The solid lines show the expected behavior for absorption (dark blue) and dispersion mode of detection (light blue), while the consequent black lines indicate the corresponding behavior for a phase mismatch of ± 0.05 radians from pure absorption and ± 0.1 radians from pure dispersion.

the white-noise level of the system was slightly increased by this increase in modulation order. As was alluded to in the paper, this increase in noise can be attributed to the effects of the laser-cavity jitter: the size of the carrier becomes smaller with increasing modulation index until it vanishes at $\beta \approx 2.4$. Still, even in this extreme case, the lock can be maintained, since in fact, all modes of the FM spectrum have their own PDH sidebands and their size is proportional to the size of the corresponding FM sideband; all these "small" PDH error signals will now[4] contribute to the net PDH error signal. However, due to the finite performance of the lock of the modulation frequency, ν_{m}, to the FSR of the cavity, the quality of the PDH error signals will decrease with the mode-number, q, of the FM spectrum. All this indicates that, for optimum conditions, NICE-OHMS should not be run with the light being a "triplet", i.e. modulated at such a low modulation index that only one pair of sidebands is produced, but rather with a higher modulation index, and thus with light consisting of more than one pair of sidebands.

9.4 Impact of noise-immune distances on NICE-OHMS

The results in chapter 9.2 made clear how susceptible to etalons a system can be. For many measurements it is indispensable to make use of the principle of etalon-immune distances (EIDs, see chapter 3.3) when arranging optical components in an experiment. **Publication XII** contains an extensive investigation of

[4]They will always contribute, even for small modulation indices, but usually one only considers the contribution arising from the carrier satellites.

the use of EIDs in both FMS and NICE-OHMS. In order to demonstrate the impact of element positioning according to the EID principle in NICE-OHMS, Db-NICE-OHMS signals in both absorption and dispersion mode of detection were recorded for three different distances between the transmission detector and the reflective surface of the cavity output mirror, $d_{\mathrm{cav-det}}$, viz. 1.0, 1.25, and 1.5 times the cavity length, L_{c}. These signals, together with fits of Eq. (6.1) are shown in Fig. 9.7. For this experiment, contributions from all other

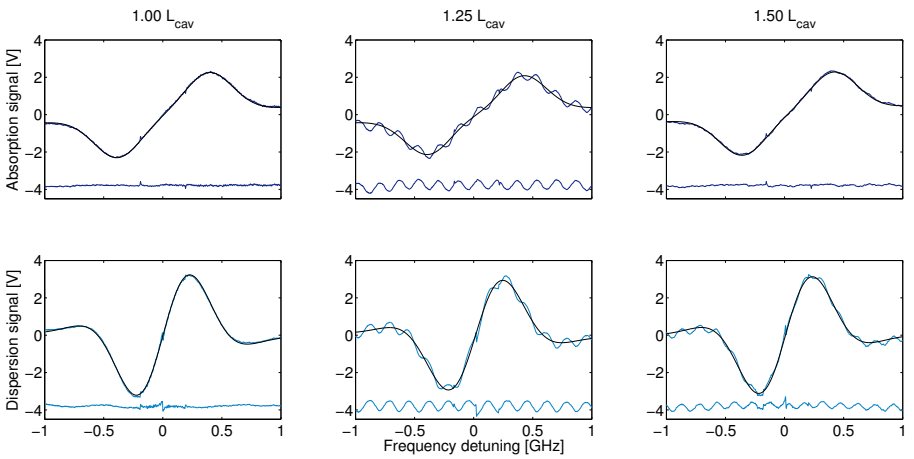

Figure 9.7: Db-NICE-OHMS signals in absorption (dark blue curves in upper panels) and dispersion mode of detection (light blue curves in lower panels) for $d_{\mathrm{cav-det}} = 1.0$, 1.25, and $1.5 \times L_{\mathrm{c}}$ (in the 1st, 2nd, and 3rd column of panels, respectively. The black line in each panel illustrates the corresponding fit of Eq. (6.1) to the data and the lowermost curve in each panel is the accompanying residual of the fit.

etalons were kept to a minimum by (*i*) removing all unnecessary components (e.g. the first polarizer after the fiber collimator, that otherwise serves for power adjustment and cleaning of the polarization state), (*ii*) placing all other components according to the EID principle as far as possible, and (*iii*) inserting an isolator in the light path between the polarizing beam splitter cube and the reflection detector. Since the position of the cavity was fixed, the transmission detector was positioned[5] so as to yield one of the three values for $d_{\mathrm{cav-det}}$ given above. As can be clearly seen and as is expected from theory, there are no major etalon contributions left in the signals for $d_{\mathrm{cav-det}} = 1.0L_{\mathrm{c}}$ and for the absorption signal for $d_{\mathrm{cav-det}} = 1.5L_{\mathrm{c}}$, whereas there are etalons in the others; this implies that $d_{\mathrm{cav-det}}$ for the $1.0L_{\mathrm{c}}$ and $1.5L_{\mathrm{c}}$ cases was at or close to an EID. The signals for $d_{\mathrm{cav-det}} = 1.25L_{\mathrm{c}}$ show a more or less equally strong contribution from the etalon, as is predicted by the theory. For $d_{\mathrm{cav-det}} = 1.50L_{\mathrm{c}}$, only the dispersion signal contains a fringe structure, as again should be the case.

[5]In order to simulate real conditions, this was done without any attempts to yield largest precision, but simply by using a ruler with mm scale, so that three positions of the detector were achieved with an accuracy of around ±3 mm.

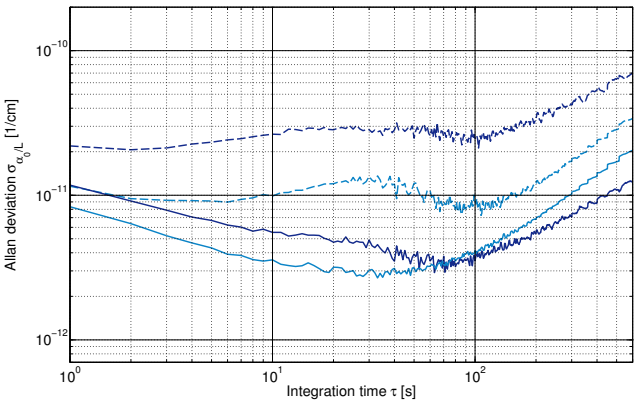

Figure 9.8: Allan-Werle plot for the experimental conditions when $d_{\mathrm{cav-det}} = 1.0L_{\mathrm{c}}$ (lower two [solid] curves) and $1.25L_{\mathrm{c}}$ (upper two [dashed] curves), both for the absorption (dark blue curves) and dispersion mode of detection (light blue curves).

However, the etalon contribution from this case should be about twice as large as in the dispersion signal at $d_{\mathrm{cav-det}} = 1.25L_{\mathrm{c}}$, which, however, is not the case. This can probably be contributed to detector alignment.

It is clear that such prominent fringe structures as those present in the signals for $d_{\mathrm{cav-det}} = 1.25L_{\mathrm{c}}$ will affect the system stability if not high care is taken. Figure 9.8 shows an Allan-Werle plot for two of the above situations ($L = 1.0L_{\mathrm{c}}$ and $1.25L_{\mathrm{c}}$) with the Lexan-box, which is encapsulating the optical system, run with open windows. In the case for $d_{\mathrm{cav-det}} = 1.25L_{\mathrm{c}}$ (represented by the two uppermost curves) the fringes in the signal were moving with time, which resulted in the fact that the assessed concentrations fluctuated, which is clearly visible in the upper two curves in the plot, which both show a hump approximately centered in the region between 10 and 100 s. When the detector was positioned so that $d_{\mathrm{cav-det}} = 1.0L_{\mathrm{c}}$, i.e. when both detection phases experienced EID conditions, this hump was not visible (even though the Lexan-box was open). All this underlines the impact and the importance of the EID principle, in particular when stable conditions cannot be provided.

9.5 DFB-laser based NICE-OHMS

The DFB laser-based NICE-OHMS system presented in **publications I** allowed for the first time the acquisition of several Db transitions within the same scan due to its wide mode-hop free injection current tuning range. Figure 9.9 shows examples, where the P_f30 line of C_2H_2 at 1550.8 nm was recorded together with its three closest neighbors. Signals have been taken for a large range of pressures reaching up to a third of an atmosphere and the Figure shows three examples thereof. It can be clearly seen that the signals get significantly broader with increasing pressure and that the effect is stronger in the absorption than in the dispersion mode of detection; e.g. compare the signals at 183 Torr, where the absorption lines melt into each other, while the dispersion signals are still reasonably well separated. Such scans did not only allow for a measurement of the broadening coefficients and center frequencies of the lines, but also for an assessment of the relative line strengths of the four transitions. In some

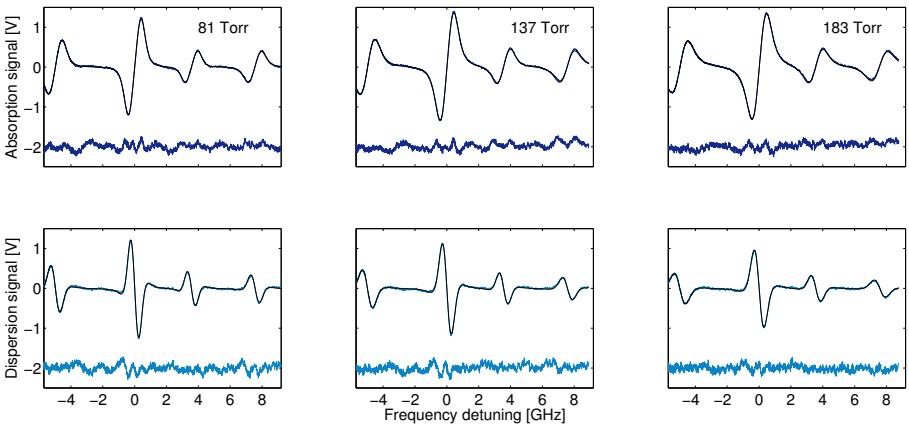

Figure 9.9: Db-NICE-OHMS signals for three different pressures, viz. 81 Torr, 137 Torr and 183 Torr (represented by the 1st, 2nd, and 3rd column of panels, respectively) for in the absorption (upper panels) and dispersion mode of detection (lower row). Curve fits of Eq. (6.1) are shown in black and the lowermost curve in each panel illustrates the accompanying residual of the fit (enlarged by a factor of 5).

cases considerable disagreements with values listed in the HITRAN database was found. This work has expanded the use of NICE-OHMS to include also DFB-lasers and spectroscopic assessments of molecular parameters from spectra incorporating a multitude of partly overlapping transitions.

9.6 Line shapes beyond the Voigt profile

It is well known that the use of an inappropriate line shape function when assessing molecular or gas parameters by fitting an expected profile to measured data can provide inaccurate results. For the cases when the transitions are affected by both Doppler and collisional broadening it is not always appropriate to use the Voigt line shape function. It has been known for a while that already at pressures around 10 Torr, the Voigt profile is no longer capable to reproduce measured data, and the situation becomes worse the higher the pressure. As was alluded to above, the two main reasons to this are Dicke narrowing and speed-dependent effects. The pressure region in which Dicke narrowing is the predominant distortion factor to the Voigt profile is roughly between 10 and 40 Torr. SDEs typically appear at pressures above 100 Torr. The influence of Dicke narrowing and speed dependent effects on pressure broadened NICE-OHMS signals has therefore been investigated thoroughly in the **publications II, V, VI** and **IX**. While both line shape effects were well-known for absorption signals, there were until recently no expressions for the line shapes incorporating these effects for the dispersion mode of detection; to be able to perform fitting to the measured signals such expressions had to be derived and verified. This was performed in the **publications II, V,** and **VI**.

As an example, Fig. 9.10 shows by the solid markers signals at two pressures, for which either Dicke narrowing (panels [a] and [b]) or SDEs (panels [c] and [d]) dominate. The solid and dashed curves represent fits to the NICE-OHMS signals based on various typos of line shapes, as indicated in the panels. It can be seen in the measurements at 40 Torr that both the Galatry and Rautian line shape function, modeling the effects of Dicke narrowing by soft and hard

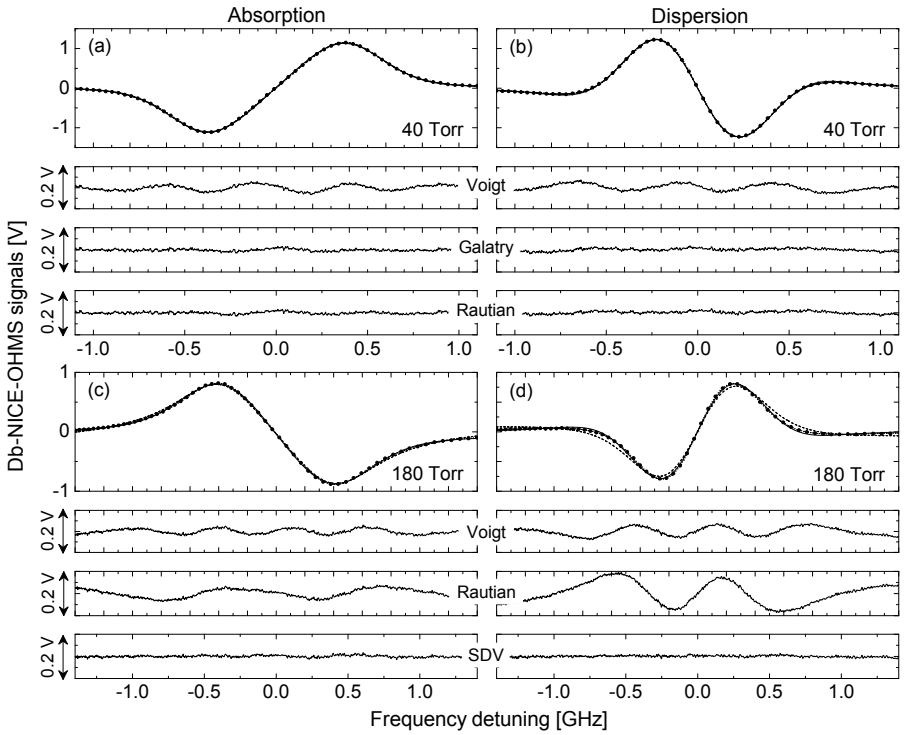

Figure 9.10: Db-NICE-OHMS signals from the $P_e(33)$ transition of acetylene at 1552.946 nm in the pressure broadened regime for two pressures, when Dicke narrowing is the dominating distortion factor to the Voigt model (40 Torr, upper panels) and when SDEs dominate (180 Torr, lower panels). The solid markers represent the measurement data and the curves the results of the fits of three line shape profiles in each case. In the panels below the accompanying residuals are illustrated.

collisions, respectively, can well account for the effects of Dicke narrowing, both in absorption and dispersion mode of detection. At 180 Torr SDEs clearly dominate the line shape profile and the Rautian profile can no longer account for all ongoing processes (not the Galatry profile either); in fact, it is even worse than the Voigt profile. Here, the speed-dependent Voigt (SDV) profile models the data impressively well. It is clear that the assessment of analyte concentration can be deteriorated if unsuitable line shape profiles are used for the fitting. The impact of the choice of the line profile on this has been investigated in **publication IX**, additionally taking phase errors into account.

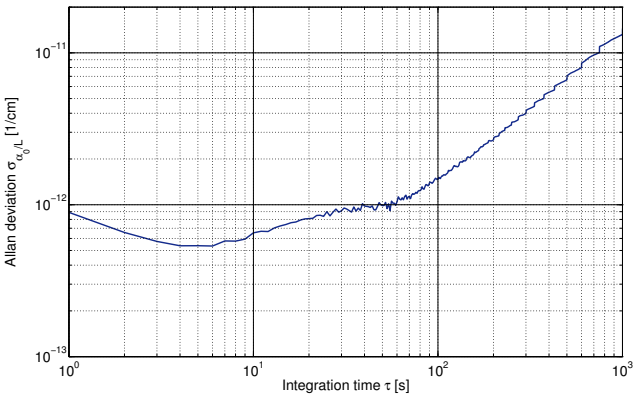

Figure 9.11: Allan-Werle plot of the system performance assessed with cavity II. The measurement was performed widely under the same conditions as for the assessment in Fig. 9.1, with an incident power on the detector of 800 µW.

9.7 Additional but yet unpublished results

The improved performance due to the strengthened laser-cavity-lock described in chapter 9.1 has offered the possibility for larger values of the finesse in FL-NICE-OHMS, and in fact a cavity with a finesse of 35000 (cavity II in chapter 8.1.5) has recently been implemented. Even though none of the attached publications includes results measured on this cavity, Fig. 9.11 shows an Allan-Werle plot with a preliminary assessment of the detection sensitivity for Db detection of dispersion signals. The white-noise level was found to be $8.9 \times 10^{-13}\,\mathrm{cm}^{-1}\ \mathrm{Hz}^{-1/2}$ up to an integration time of about four to five seconds, where it reaches $5.4 \times 10^{-13}\,\mathrm{cm}^{-1}$, corresponding to an estimated[6] lowest detectable C_2H_2 concentration of just above one part-per-trillion (1.3 ppt). As can be seen from the Figure, an etalon contributed to an increase of the Allan deviation at integration times of around five to 50 seconds, before finally a linear drift determines the system limit. The origin of this has not yet been assessed. Despite this, this is the so far best achieved NICE-OHMS detection sensitivity incorporating a tunable diode laser.

The large detection power of cavity II allows for a demonstration of the applicability of NICE-OHMS for detection of molecular compounds in breath. Figure 9.12 shows an example of detection of a center sD dispersion signal of the $P_e(11)$ line of acetylene, taken from a breath sample of a smoker approximately five minutes after having smoked a cigarette. However, it was found that detection of C_2H_2 using Db-NICE-OHMS addressing the frequently used $P_e(11)$ line was affected the presence of an overlapping, strong ammonia (NH_3) line in the direct neighborhood of the acetylene line. Since the NH_3 lines in this wavelength region have not yet been incorporated in the most commonly used databases, e.g. HITRAN [61], but only appear in specific research publications [93], these spectral interferences could not be predicted beforehand. On the other hand, since the C_2H_2 transition could be optically saturated, it was possible to adress a narrow sD feature of C_2H_2 which was not interfering with

[6] In **publication IV** the lowest detectable acetylene concentration was estimated to 4 ppt, where the lowest white-noise equivalent absorption was $2 \times 10^{-12}\,\mathrm{cm}^{-1}$, which is a factor of three above the value assessed with cavity II.

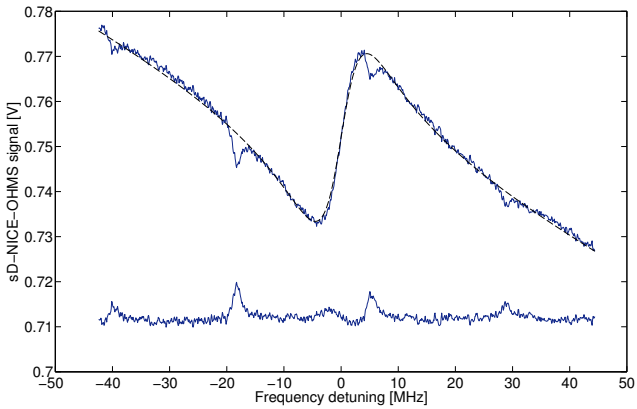

Figure 9.12: Center sD dispersion signal (upper blue curve) of a breath sample taken from a smoker approximately five minutes after smoking a cigarette, together with a fit of Eq. (6.30) in [4] (dashed black curve) and the accompanying residual (lowermost curve). The concentration of C_2H_2 was assessed to 100 ppb.

any other sD-signal. The concentration of acetylene in the exhaled air from a smoker was assessed[7] to be 100 ppb. This illustrates the potential of the technique for breath analysis. However, it also underlines the need of addressing transitions with a minimum of spectral interferences. More work is needed to assess the full potential of NICE-OHMS for breath analysis, and, for the case of detection of C_2H_2, in particular addressing a transition with no major spectral interference from any other constituents existing in breath.

[7] It should be noted that this was a demonstration of the detection capability. The assessed concentration level is significantly larger as compared to those found in the work in Ref. [94], which all were in the 1.0 ppb to 8.4 ppb range. The background level of acetylene in a sample, taken directly before smoking a cigarette, was assessed below the detection limit of C_2H_2 in the presence of NH_3.

10

Conclusion and Future Prospects

In the course of this thesis work, NICE-OHMS has not only been both technically further developed, but also scrutinized regarding its underlying concepts. Together, this formed a basis that made the technique more versatile and robust with an excellent detection sensitivity.

It is clear that there is a large number of species that exist in exceedingly low concentrations, sometimes even in the ppt or sub-ppt range, in various types of samples that are of interest to monitor. To be able to address such species, it should be clear that it is of importance to realize NICE-OHMS instrumentations with the highest possible detection sensitivity for as many types of species as possible. Therefore, whenever a new system is to be designed for a given molecular species, the work in **publication X** provides important guidelines and discussions concerning the choice of system parameters, among them the modulation index, modulation frequency, and detection phase to reach the optimum detection conditions for a given type of species. Moreover, this work provides the so far first consistent analysis of the intricate interplay between cavity length and modulation frequency. These findings are certainly also applicable whenever an existing system is to be optimized, even though some of the parameters, such as the cavity length, then are hard to change; still, both modulation and demodulation settings are mostly[1] of electronic character and can therefore be swiftly adjusted.

An attempt in striving for a robust system was presented in the work in **publication VIII**, where it was shown that the optical setup of NICE-OHMS can be significantly reduced by the implementation of a fiber-coupled optical circulator without a loss of detection sensitivity of the system but for a small factor. In fact, one could go one step ahead and detect the absorber in cavity reflection, more precise in the error signal for the FSR control, as has been demonstrated in Ref. [40]. This approach would restrict the free-space light path down to the way from the fiber collimator to the cavity and would make

[1] One might also be restricted by the modulation bandwidth of the EOM, which typically is a larger expense than RF electronics.

the optical part of the technique robust, flexible, and user-friendly.

Another important step to make NICE-OHMS more attractive for future applications was the realization of a NICE-OHMS setup around a DFB laser in **publication I**. Not only is this type of laser immune to acoustic disturbances[2], it also offers a wide mode-hop-free tuning range of several GHz. The DFB-NICE-OHMS system offered a detection sensitivity of $1.5 \times 10^{-9}\,\mathrm{cm}^{-1}\ \mathrm{Hz}^{-1/2}$, mainly limited by the laser line width control, and allowed for accurate studies of collisional broadened transitions[3] as presented in **publications II, V, VI, and IX**, where line shapes were investigated that account for speed-dependent effects and the effect of Dicke narrowing. These works have demonstrated that whenever high accuracy in the collisional broadened regime is needed, the use of line shape models beyond the Voigt profile is inevitable.

At the time when the work for this thesis was commenced, the most prosperous NICE-OHMS instrumentation was without any doubt the FL-NICE-OHMS instrumentation described in Refs. [32, 33, 35] with its best performance in Db detection of dispersion signals with an absorption sensitivity of only $1.8 \times 10^{-11}\,\mathrm{cm}^{-1}\ \mathrm{Hz}^{-1/2}$ for an integration times up to around ten seconds[4] [43]. Back then, the system performance was limited by the (*i*) restricted bandwidth of the laser-to-cavity lock incorporating only feedback to the PZT tuning stage of the fiber-laser and (*ii*) vibrations and disturbances that have their original in the laboratory environment and which are propagating into the detection scheme directly through the atmosphere or the optical table. These problems were tackled in the work described in **publication IV**, where both the laser-cavity lock (by incorporation of an AOM) and the insulation from the environment were markedly improved, which, together with an optimum choice of the modulation index (**publication XI**), yielded a lowest detectable absorption of $4.9 \times 10^{-12}\,\mathrm{cm}^{-1}\ \mathrm{Hz}^{-1/2}$ for integration times up to at least 10 s and a cavity with a finesse of 5700. In all this, it was particularly important to make use of EIDs (which is more deeply investigated in **publication XII**) to the largest possible extent.

As has been shown in chapter 9.7, the strengthened laser-cavity-lock opened for an increase of cavity finesse of almost one order of magnitude, i.e. from 5700 to 35000. The detection sensitivity of the instrument could by this be improved to a level of $8.9 \times 10^{-13}\,\mathrm{cm}^{-1}\ \mathrm{Hz}^{-1/2}$ up to an integration time of about five seconds, where it was assessed to $5.4 \times 10^{-13}\,\mathrm{cm}^{-1}$. This is the so far best achieved NICE-OHMS detection sensitivity assessed with an instrument based on a tunable diode laser and corresponds to a lowest detectable acetylene concentration of around one part-per-trillion or 4×10^{6} molecules / cm^3. This also implies that during the course of this thesis work the white-noise level has been decreased by a factor of 20.

This detection sensitivity together with the potential compactness and robustness of NICE-OHMS naturally opens for a variety of possible applications

[2] In contrast to the EDFL, the fiber-cavity inside of which easily picks up any kind of turbulences.

[3] Again in contrast to the FL-NICE-OHMS system, the tunability of which was limited to 3 GHz scans over molecular transitions.

[4] The approximate time where the Allan-Werle plot deviates from white-noise behavior.

Constituent		c_{atm}	$c_{\mathrm{min}}^{1\sigma}$	$\lambda_{\mu\mathrm{m}}^{\mathrm{region}}$
Acetylene	C_2H_2	–	1 ppt	1.5
Carbon dioxide	CO_2	380 ppm	10^2 ppb	1.5
Nitric oxide	NO_2	0–1500 ppt	10^2 ppm	1.1
Nitrous oxide	N_2O	–	10^2 ppt	1.5
Oxygen	O_2	21%	10^1 ppt	1.5
Hydroxyl radical	OH	0–0.6 ppt	10^1 ppt	1.5
Methane	CH_4	1800 ppb	10^1 ppb	1.5

Table 10.1: Molecular constituents in air that can possibly be addressed with fiber-lasers at either 1.1 or 1.5 µm. Typical concentration levels, c_{atm}, of course depend on the exact place of measurement and differs with altitude, longitude, latitude, season, local factors, etc. [1] The lowest detectable concentration, $c_{\mathrm{min}}^{1\sigma}$, has been extrapolated from the above estimation of the detection power of cavity II, together with the typical line strength of the corresponding species taken from the HITRAN database [61], rounded to the closest power of ten.

in the further course of FL-NICE-OHMS. Two possible application areas are detection of bio-markers in breath (see chapter 9.7) and atmospheric trace gas detection. Atmospheric species can occur in very different concentrations, covering the entire range from almost unity (air contains around 78% of N_2) down to ppt-levels (e.g. for HO_2) [1]; Table 10.1 shows a summary of molecular compounds present in the atmosphere that can in principle be reached with fiber-lasers either at 1.1 or 1.5 µm (for which the type of fiber lasers used in FL-NICE-OHMS presently are available), together with their extrapolated concentration detection limit. Despite the fact that there is a large number of other gases that cannot be addressed in either of the two wavelength regions, this shows the potential of the technique for these kind of investigations.

In the beginning of this thesis it was alluded to that instruments in the near-IR address overtones of transitions – and the fiber-laser-based NICE-OHMS system surely does this with an undeniably outstanding performance. A real potential for future NICE-OHMS applications, though, resides in the realization of spectrometers based on laser systems lasing in the mid-IR region that can address the fundamental vibrational-rotational transitions that are two to three orders of magnitude stronger than their overtones in the near-IR. In the last years, these systems have been started to be employed for instruments based on the noise-immune concept, e.g. with the use of difference frequency generation (DFG) systems [54], optical parametrical oscillators (OPOs) for detection of molecular ions [53, 55], or external cavity quantum-cascade-lasers [57]. A major problem all these systems have to cope with is though the lack of instrumentation in the mid-IR, primarily modulators and high-end detectors. A means around this is to use an OPO system to create light in the mid-IR region, and to perform the necessary modulation on the pump source in the near-IR region. It remains to be seen during the upcoming years whether these systems can eventually make use the potential that mid-IR transitions offer to the NICE-OHMS technique.

Another and so far never seriously adressed field is the transfer of NICE-OHMS towards analytical atomic spectrometry (AAS). Within the scope of an invited paper contribution to a special issue of Spectrochimica Acta B, **publication XIII** investigates the potential detection capability of noise-immune cavity-enhanced analytical atomic spectrometry (NICE-AAS) at the example of mercury (Hg) and sodium (Na). Converting the best (published) FL-NICE-OHMS detection sensitivity, i.e. $4.9 \times 10^{-12}\,\mathrm{cm}^{-1}\,\mathrm{Hz}^{-1/2}$ over 10 s, this work shows that it should be possible to detect[5] 25 Hg-atoms per cubic centimeter (corresponding to $10\,\mathrm{zg/cm}^3$) or solely 15 Na-atoms per cubic centimeter (injected into a graphite furnace, corresponding to 50 zg/ml in liquid solution), the latter corresponding to an analyte concentration in the parts-per-sextillion (pps, $1{:}10^{21}$) range. The estimated Hg-detection power is five orders of magnitude better than any previous realized laser-based AAS technique. This might even suggest the possibility of single-atom detection, but as a matter of course these numbers should be taken with care, since, for example, individual atoms do only have a finite residence time in the laser beam. Nevertheless, especially with diode-laser systems that are readily available in almost the entire spectrum from the UV up to the IR, there should not be any unconquerable technical problems for the realization of a NICE-AAS instrument with the potential to widen the scope of AAS.

[5] Addressing a transition in the UV at 253.56 nm for Hg, and a transition in the visible at 589.0 nm for Na.

Appendix – AOM frequency control servo

The AOM frequency control was described in detail in chapter 8.1.2. This schematic is the realization that has been implemented for the work in **publication IV**.

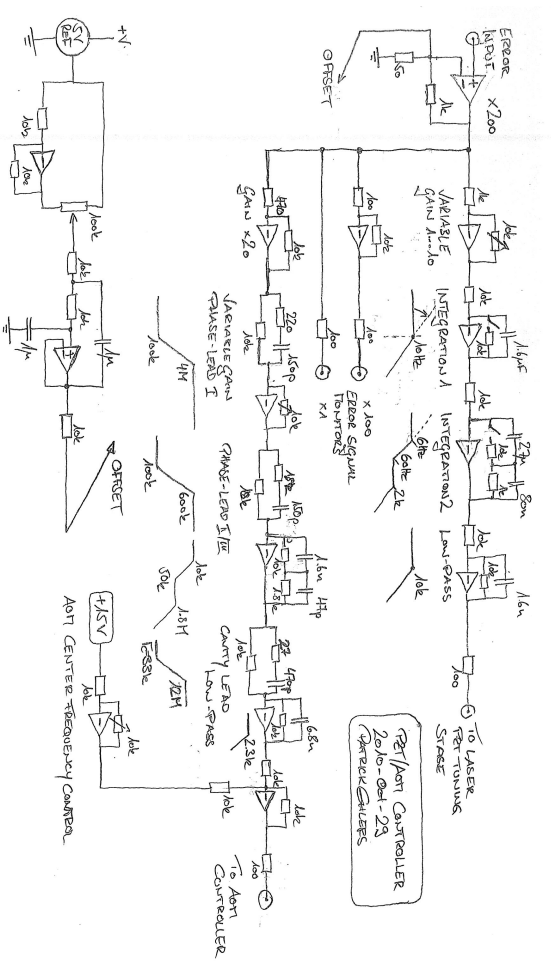

Acknowledgements

A PhD thesis work in experimental physics is seldom performed without the help of others and I want to take the opportunity at this point to thank various people for their help and contributions.

First of all, I wish to express my very great gratitude to my supervisor, Prof. Ove Axner, for giving me the opportunity to perform my PhD studies in his brilliant research group. In many situations I did not only appreciate his constructive help, but also his way of promptly being available for questions, problems, and concerns. His professional and modern leadership provided both efficient research conditions, as well as a pleasant working atmosphere, at the same time making it possible to smoothly combine my studies with the life challenges that young families encounter.

I want to thank Junyang Wang and Isak Silander for being great fellows on the project; thanks, Junyang, for solving whichever of my theoretical problems by the next morning, and Isak, for many fruitful discussions and some brilliant ideas that solved a lot of technical problems. Thanks also go to Aleksandra Foltynowicz and Weiguang Ma for competently introducing me into NICE-OHMS and for being available for help and support even afterwards. Then, of course, good luck to Thomas Hausmaninger for the upcoming years on the experiment. Moreover, I would like to thank Jonas Westberg for numerous hours on the UV-project discussing best bread-baking techniques.

I also would like to express my gratefulness to the staff at the Physics department. In particular, I would like to thank Lena Åström, Tomas Gustafsson, Leif Hassmyr, Roushdey Salh, and Peter Wikström for their valuable technical support. I also wish to thank the entire administrative team for their help and support, therefore my gratitude goes to Gabriella Allansson, Lilian Andersson, Lena Burström, Ann-Charlott Dalberg, Hans Forsman, Carina Jonsson, and – even though mostly invisibly acting, but not to forget – Kjell Rönnmark; moreover, special thanks go to Katarina Hassler for her unremitting efforts in guiding PhD students through the coppice of rules and regulations, which not always has been an easy task. I wish to thank Lars Karlsson and Tomas Lock for their qualified and fast help whenever I encountered problems with electronics. Moreover, I wish to acknowledge the help of Lars-Erik Svensson

and Nils Blix, whenever my computers did things that they were not supposed to do. My gratitude also goes to Bertil Sundqvist for sharing his immense experimental knowledge in many helpful discussions and advices. Thanks also go to Jörgen Eriksson and Karin Rinnefeldt, not only for keeping things running and clean, respectively, but also for many occasional conversations perking me up on cloudy days. All of you were always giving your best.

I would like to express my gratitude to Georg Hunn, Wolfgang Roether, and Michael Bach for inspiring and motivating me in the past, each of them in a unique way.

I want to thank my mother, my late father, my stepfather, and my parents-in-law for their unfailing support. Their help and love made it possible to establish a home in Umeå and to successfully work on my thesis. My deep gratitude also goes to my sister-in-law, Ina, for her invaluable help and presence.

Thank you, Andreas and Bastien, for being good friends. And thank you, Angelica, Lars, Wilma, Gabriel, Sofia, David, Edith, Imre, Ann, Samuel, and Linnea, for sharing a lot of time with us. Your friendship has made the time in Umeå unforgettable. Thanks also go to my german friends Stefan, Katharina, Martin, Daniel, Michael, and Hannah. And, of course, thanks to Stephan for uncountable hours of support and refreshment on the phone.

Finally, I deeply thank my wonderful wife, Sarah, and my sons, Felix and Jonas. Thank you, all three of you, for bringing plenty of joy into my life, giving it meaning, and for being there.

Nomenclature

Abbreviations

AOM	Acousto-optic modulator
DAS	Direct absorption spectroscopy
Db	Doppler broadened
DFB	Distributed feedback (laser)
DFG	Difference frequency generation
EC-QCL	External-cavity quantum cascade laser
ECDL	External-cavity diode laser
EDFL	Erbium-doped distributed-feedback-laser pumped fiber laser
EID	Etalon immune distance
EOM	Electro-optic modulator
FCOC	Fiber-coupled optical circulator
FFT	Frequency transfer function
FL	Fiber-laser(-based)
FM	Frequency modulation
fm	Frequency modulated
FMS	Frequency modulation spectroscopy
FS	Free-space

FSR ..... Free spectral range

FWHM ..... Full-width at half-maximum

HITRAN ..... Acronym for High Resolution Transmission, a compilation of molecular parameters

HWHM ..... Half-width at half-maximum

IR ..... Infrared

IUPAC ..... International Union of Pure and Applied Chemistry

NICE-OHMS ..... Noise-immune cavity-enhanced optical heterodyne molecular spectroscopy

OPO ..... Optical parametrical oscillators

PM ..... Polarization maintaining

ppb ..... Part(s)-per-billion

ppm ..... Part(s)-per-million

ppt ..... Part(s)-per-trillion

QCL ..... Quantum cascade laser

RAM ..... Residual amplitude modulation

RF ..... Radio frequency

sD ..... Sub-Doppler

SDE ..... Speed-dependent effects

SDV ..... Speed-dependent Voigt (-profile)

TDLAS ..... Tunable diode-laser based absorption spectroscopy

TEM ..... Transverse electromagnetic

VCO ..... Voltage-controlled oscillator

WMS ..... Wavelength modulation spectroscopy

Variables & Functions

α ..... Absorption coefficient ($1/[L]$)

α_0 ..... On-resonance absorption ($1/[L]$)

β ..... Modulation index

Γ'_{D} ..... Modified HWHM Doppler width, equal to $\Gamma_{\mathrm{D}}/[\ln(2)]^{1/2}$

Γ_c ..... HWHM cavity mode width

Γ_D ..... HWHM Doppler width ($[\nu]$)

Γ_L ..... HWHM Lorentzian width ($[\nu]$)

Δf ..... Detection bandwidth (Hz)

$\Delta I/I_0$ ..... Relative absorption

δ^A ..... Attenuation due to the presence of an absorber

δ_k^A ..... Attenuation of mode k due to the presence of an absorber

$\hat{\epsilon}$ ..... Unity vector indicating the direction of the electrical field

ϵ_0 ..... Vacuum permittivity,
equal to $8.854\,187\,817 \times 10^{-12}\,\mathrm{C/(Vm)}$

η_fm ..... FM instrumentation factor (V/W)

κ ..... Intra-cavity power buildup

$\bar{\Lambda}$ ..... Mean free path of a molecule

$\hat{\Lambda}$ ..... Estimate of an analyte amount or concentration

Λ ..... True value of an analyte amount or concentration

Λ_C ..... Detection decision limit

Λ_D ..... Detection limit

Λ_Q ..... Quantification limit

λ ..... Wavelength of the light ($[L]$)

λ_0 ..... Wavelength of the laser light (m)

μ ..... Expectation value

ν ..... Frequency of the light (Hz)

$\bar{\nu}$ ..... Wave number (cm^{-1})

ν_0 ..... Transition center frequency (Hz)

ν_q ..... Center frequency of cavity mode q

ν_c ..... Carrier frequency (Hz)

ν_d ..... Frequency detuning from mode center (Hz)

ν_FSR ..... Free spectral range (Hz)

ν_m ..... Modulation frequency (Hz)

σ ..... Standard deviation

$\sigma(\nu_\mathrm{d})$ ..... frequency-dependent transition cross section

σ_0 ..... Standard deviation of the blank

σ_A ..... Allan deviation

σ_m ..... Standard deviation of the mean

τ ..... Averaging or integration time

τ_c ..... Cavity decay time

τ_{max} ..... Maximum averaging time

ϕ^A ..... Phase-shift due to the presence of an absorber

ϕ_k^A ..... Phase-shift of mode k due to the presence of an absorber

χ_0 ..... Peak-value of χ^abs, i.e. the area-normalized absorption line shape function (cm)

χ^abs ..... Area-normalized absorption line shape function (cm)

$\bar{\chi}^\mathrm{abs}$ ..... Dimensionless peak-normalized absorption line shape function

χ^disp ..... Counter part to χ^abs, i.e. the area-normalized absorption line shape function (cm)

$\bar{\chi}_\mathrm{NO}^\mathrm{Db}$ ..... Doppler-peak normalized NICE-OHMS line shape function

$\chi_\mathrm{V}^\mathrm{abs}$ ..... Absorption Voigt profile (cm)

$\chi_\mathrm{V}^\mathrm{disp}$ ..... Dispersion Voigt profile (cm)

B_p ..... Pressure broadening coefficient (MHz/Torr)

c ..... Speed of light, equal to 299 792 458 m/s

c_rel ..... Relative analyte concentration

E ..... Real electrical field of the light (V/m)

e ..... Electron charge, equal to $1.602\,176\,57 \times 10^{19}$ C

E_0 ..... Amplitude of the electrical field of the light (V/m)

$\tilde{E}^\mathrm{A}$ ..... Absorber-transmitted electrical field (V/m)

$\tilde{E}$ ..... Complex electrical field of the light (V/m)

F ..... Cavity finesse

G ..... Degree of optical saturation

$G(f)$ ..... Frequency transfer function of the controlled system

$H(f)$ ..... Frequency transfer function of the control system loop filter

I ..... Intensity of light ($\mathrm{W/m^2}$)

I_0 ..... Incident intensity of light ($\mathrm{W/m^2}$)

I_c ..... Intracavity intensity ($\mathrm{W/m^2}$)

I_sat ..... Transition saturation intensity ($\mathrm{W/m^2}$)

J_k ..... Bessel function of order k

k_B ..... Boltzmann constant, equal to $1.380 \times 10^{-23}\,\mathrm{J/K}$

L ..... (Single-pass) Interaction length between light and sample (m)

$l_{1,2}$ ..... Intensity losses coefficient of front- and back-mirror, respectively

L_D ..... Characteristic cavity length, given by $c/(2\Gamma_\mathrm{D})$

$L_\mathrm{EID}^{q,\mathrm{abs/disp}}$ ..... Etalon immune length (m)

L_m ..... Length corresponding to ν_m, given by $c/(2n\nu_\mathrm{m})$ (given in m)

L_c ..... Cavity length (m)

L_eff ..... Enhanced / effective interaction length (m)

M ..... Molecular mass of a molecule (u)

n_0 ..... Loschmidt constant, equal to $2.686\,780\,5(24) \times 10^{25}\,\mathrm{molecules/m^3}$

n_A ..... Number density of molecules

p ..... Pressure (Torr)

P_0 ..... Power incident on the cavity or detector (W)

P_c ..... Intracavity power (W)

$r_{1,2}$ ..... Intensity reflection coefficient of front- and back-mirror, respectively

S ..... Molecular line strength ($\mathrm{cm^{-2}/[p]}$)

$\hat{S}$ ..... Integrated molecular line strength ($\mathrm{cm^{-1}/(molecule\ cm^{-2})}$)

S_0 ..... Signal strength (V)

S_Db ..... Doppler-broadened NICE-OHMS signal (V)

$S_{\mathrm{fm}}^{\mathrm{T}}$	DC component of the FM signal (V)
t	Time (s)
$t_{1,2}$	Intensity transmission coefficient of front- and back-mirror, respectively
T_k^{A}	Absorber transmission function for mode k
T_{exp}	Experimental temperature (K)
$\tilde{T}^{\mathrm{A}}$	Transmission function of the absorber
w	Half-width of a laser beam with a Gaussian intensity distribution profile (m)
w_0	Laser spot size in the beam waist (m)
$W(x+\mathrm{i}\,y)$	Error function for a complex argument
z_0	Rayleigh range (m)

Bibliography

[1] A. Fried and D. Richter. *Analytical Techniques for Atmospheric Measurement*, chapter 2: Infrared Absorption Spectroscopy. Wiley-Blackwell, 2006. (Cited on pages 1, 2, 3, 4, 7, 8, 21, and 81.)

[2] J. Ye and J.L. Hall. *Cavity-enhanced spectroscopies*, volume 40 of *Experimental Methods in the Physical Sciences*, chapter 3: Absorption detection at the quantum limit: probing high-finesse cavities with modulation techniques, pages 83–127. Elsevier Science, 2002. (Cited on pages 2, 49, and 50.)

[3] E.C. Richard, K.K. Kelly, R.H. Winkler, R. Wilson, T.L. Thompson, R.J. McLaughlin, A.L. Schmeltekopf, and A.F. Tuck. A fast response near-infrared tunable diode lase absorption spectrometer for in situ measurements of CH_4 in the upper troposphere and lower stratosphere. *Applied Physics B*, 75:183–194, 2002. (Cited on page 3.)

[4] O. Axner, P. Ehlers, A. Foltynowicz, I. Silander, and J. Wang. *Cavity-Enhanced Spectroscopy and Sensing*, volume 179 of *Springer Series in Optical Sciences*, chapter 6: NICE-OHMS – Frequency Modulation Cavity-Enhanced Spectroscopy - Principles and Performance, pages 211–251. Springer, 2014. (Cited on pages 4, 5, 6, 9, 12, 16, 17, 18, 35, 41, 42, 49, 50, and 78.)

[5] J. Ye. *Ultrasensitive high resolution laser spectroscopy and its application to optical frequency standards*. PhD thesis, University of Colorado, 1997. (Cited on page 4.)

[6] L.S. Ma, J. Ye, P. Dube, and J.L. Hall. Ultrasensitive frequency-modulation spectroscopy enhanced by a high-finesse optical cavity: theory and application to overtone transitions of C_2H_2 and C_2HD. *Journal of the Optical Society of America B*, 16(12):2255–2268, 1999. (Cited on pages 4 and 5.)

[7] J. Ye, L.S. Ma, and J.L. Hall. Ultrasensitive detections in atomic and molecular physics: demonstration in molecular overtone spectroscopy. *Journal of the Optical Society of America B*, 15(1):6–15, 1998. (Cited on pages 4 and 5.)

[8] C. Ishibashi and H. Sasada. Highly sensitive cavity-enhanced sub-Doppler spectroscopy of a molecular overtone band with a 1.66 μm tunable diode laser. *Japanese Journal of Applied Physics*, 38:920–922, 1999. (Cited on pages 4 and 5.)

[9] C. Ishibashi and H. Sasada. Near-infrared laser spectrometer with sub-Doppler resolution, high sensitivity, and wide tunability: A case study in the 1.65 μm region of CH_3I spectrum. *Journal of Molecular Spectroscopy*, 200:147–149, 2000. (Cited on pages 4 and 5.)

[10] L. Gianfrani, R.W. Fox, and L. Hollberg. Cavity-enhanced absorption spectroscopy of molecular oxygen. *Journal of the Optical Society of America B*, 16:2247–2254, 1999. (Cited on pages 4, 5, and 23.)

[11] J. Bood, A. McIlroy, and D.L. Osborn. Measurement of the sixth overtone band of nitric oxide, and its dipole moment function, using cavity-enhanced frequency modulation spectroscopy. *The Journal of Chemical Physics*, 124: 084311, 2006. (Cited on pages 4 and 5.)

[12] J. Bood, A. McIlroy, and D.L. Osborn. Cavity-enhanced frequency modulation absorption spectroscopy of the sixth overtone band of nitric oxide. *Proceedings of SPIE*, 4962:89–100, 2003. (Cited on pages 4 and 5.)

[13] N.J. van Leeuwen and A.C. Wilson. Measurement of pressure-broadened, ultraweak transitions with noise-immune cavity-enhanced optical heterodyne molecular spectroscopy. *Journal of the Optical Society of America B*, 21:1713–1721, 2004. (Cited on pages 4 and 5.)

[14] N.J. van Leeuwen, H.G. Kjaergaard, D.L. Howard, and A.C. Wilson. Measurement of ultraweak transitions in the visible region of molecular oxygen. *Journal of Molecular Spectroscopy*, 228:8–913, 2004. (Cited on pages 4 and 5.)

[15] C.L. Bell, G. Hancock, R. Peverall, G.A.D. Ritchie, J.H. van Helden, and N.L. van Leeuwen. Characterization of an external cavity diode laser based ring cavity NICE-OHMS system. *Optics Express*, 17:9834–9839, 2009. (Cited on pages 4 and 5.)

[16] C.L. Bell, J.H. van Helden, T.P.J. Blaikie, G. Hancock, N.J. van Leeuwen, R. Peverall, and G.A.D. Ritchie. Noise-immune cavity-enhanced optical heterodyne detection of HO_2 in the near-infrared range. *The Journal of Physical Chemistry A*, 116:5090–5099, 2012. (Cited on pages 4 and 5.)

[17] A.A. Mills, B.M. Siller, and B.J. McCall. Precision cavity enhanced velocity modulation spectroscopy. *Chemical Physics Letters*, 501:1–5, 2010. (Cited on pages 4 and 5.)

[18] B.M. Siller, A.A. Mills, and B.J. McCall. Cavity-enhanced velocity modulation spectroscopy. *Optics Letters*, 35:1266–1268, 2010. (Cited on pages 4 and 5.)

[19] A.A. Mills, B.M. Siller, M.W. Porambo, M. Perera, H. Kreckel, and B.J. McCall. Ultra-sensitive high-precision spectroscopy of a fast molecular ion beam. *The Journal of Chemical Physics*, 135:224201, 2011. (Cited on pages 4 and 5.)

[20] B.M. Siller, M.W. Porambo, A.A. Mills, and B.J. McCall. Noise immune cavity enhanced optical heterodyne velocity modulation spectroscopy. *Optics Express*, pages 24822–24827, 2011. (Cited on pages 4 and 5.)

[21] J. Ye, L.S. Ma, and J.L. Hall. High-resolution frequency standard at 1030 nm for Yb:YAG solid-state lasers. *Journal of the Optical Society of America B*, 17:927–931, 2000. (Cited on pages 4 and 5.)

[22] M.L. Silva. *Spectroscopic investigation of the X and A state dynamics of* $^{13}C_2H_2$. PhD thesis, Massachusetts Institute of Technology, 2002. (Cited on page 4.)

[23] D.R. Weise. *Preparation and highly sensitive detection of ultracold molecules.* PhD thesis, University of Konstanz, 2004. (Cited on page 4.)

[24] H. Zhang, Y.Z. Zhang, Z.X. Yin, X.B. Wang, and W.G. Ma. Theoretical Analysis of the RAM of FM strong absorption spectroscopy. *Spectroscopy and Spectral Analysis*, 32:1334–1338, 2012. (Cited on page 4.)

[25] H. Dinesan, E. Fasci, A. Castrillo, and L. Gianfrani. Absolute frequency stabilization of an extended-cavity diode laser by means of noise-immune cavity-enhanced optical heterodyne molecular spectroscopy. *Optics Letters*, 39:2198–2201, 2014. (Cited on pages 4 and 5.)

[26] A. Foltynowicz. *Fiber-laser-based Noise-Immune Cavity-Enhanced Optical Heterodyne Molecular Spectrometry.* PhD thesis, Umeå university, 2009. (Cited on pages 4, 6, 8, 9, 23, 32, 39, 42, 54, 58, and 59.)

[27] J. Wang. *Dicke narrowing and speed-dependent effects in dispersion signals: influence on assessment of concentration and spectral parameters by noise-immune cavity-enhanced optical heterodyne molecular spectrometry.* PhD thesis, Umeå university, 2013. (Cited on pages 4, 12, and 61.)

[28] F.M. Schmidt. *Laser-based absorption spectrometry: development of NICE-OHMS towards ultra-sensitive trace species detection.* PhD thesis, Umeå university, 2007. (Cited on page 4.)

[29] M.S. Taubmann, T.L. Myers, B.D. Cannon, and R.M. Williams. Stabilization, injection and control of quantum cascade lasers, and their application to chemical sensing in the infrared. *Spectrochimica Acta A*, 60:3457–3468, 2004. (Cited on pages 4 and 5.)

[30] Strebe. Winkel triple projection sw, licensed under creative commons attribution-share alike 3.0 via wikimedia commons. `http://commons.wikimedia.org/wiki/File:Winkel_triple_projection_SW.jpg`. [Online; accessed 29-July-2014]. (Cited on page 5.)

[31] J. Ye and J.L. Hall. *Cavity-enhanced spectroscopies*, chapter 3: Absorption detection at the quantum limit: probing high-finesse cavities with modulation techniques, pages 83–127. Experimental Methods in the Physical Sciences. Elsevier Science, New York, 2002. (Cited on pages 5 and 6.)

[32] F.M. Schmidt, A. Foltynowicz, W. Ma, and O. Axner. Fiber-laser-based noise-immune cavity-enhanced optical heterodyne molecular spectrometry for Doppler-broadened detection of C_2H_2 in the parts per trillion range. *Journal of the Optical Society of America B*, 24(6):1392–1405, 2007. (Cited on pages 5, 6, 51, and 80.)

[33] F.M. Schmidt, A. Foltynowicz, W. Ma, T. Lock, and O. Axner. Doppler-broadened fiber-laser-based NICE-OHMS - Improved detectability. *Optics Express*, 15(17):10822–10831, 2007. (Cited on pages 5, 6, and 80.)

[34] A. Foltynowicz, F.M. Schmidt, W. Ma, and O. Axner. Theoretical description of Doppler-broadened noise-immune cavity-enhanced optical heterodyne molecular spectroscopy under optically saturated conditions. *Journal of the Optical Society of America B*, 25(7):1144–1155, 2008. (Cited on pages 5, 6, 9, 11, and 15.)

[35] A. Foltynowicz, W. Ma, F.M. Schmidt, and O. Axner. Doppler-broadened noise-immune cavity-enhanced optical heterodyne molecular spectrometry signals from optically saturated transitions under low pressure conditions. *Journal of the Optical Society of America B*, 25(7):1156–1165, 2008. (Cited on pages 5, 6, and 80.)

[36] O. Axner, W. Ma, and A. Foltynowicz. Sub-Doppler dispersion and noise-immune cavity-enhanced optical heterodyne molecular spectroscopy revised. *Journal of the Optical Society of America B*, 25(7):1166–1177, 2008. (Cited on pages 5 and 6.)

[37] A. Foltynowicz, F.M. Schmidt, W. Ma, and O. Axner. Noise-immune cavity-enhanced optical heterodyne molecular spectroscopy: Current status and future potential. *Applied Physics B*, 92(3):313–326, 2008. (Cited on pages 5 and 6.)

[38] A. Foltynowicz, W. Ma, and O. Axner. Characterization of fiber-laser-based sub-Doppler NICE-OHMS for quantitative trace gas detection. *Optics Express*, 16(19):14689–14702, 2008. (Cited on pages 5, 6, and 53.)

[39] A. Foltynowicz, W. Ma, F.M. Schmidt, and O. Axner. Wavelength-modulated noise-immune cavity-enhanced optical heterodyne molecular spectroscopy signal line shapes in the Doppler limit. *Journal of the Optical Society of America B*, 26(7):1384–1394, 2009. (Cited on pages 5 and 6.)

[40] F.M. Schmidt, W. Ma, A. Foltynowicz, and O. Axner. Highly sensitive dispersion spectroscopy by probing the free spectral range of an optical cavity using dual-frequency modulation. *Applied Physics B*, 101(3):497–509, 2010. (Cited on pages 5, 6, 60, and 79.)

[41] A. Foltynowicz, J. Wang, P. Ehlers, and O. Axner. Distributed-feedback-laser-based NICE-OHMS in the pressure-broadened regime. *Optics Express*, 18(18):18580–18591, 2010. (Cited on pages 5, 6, 61, and 62.)

[42] J. Wang, P. Ehlers, I. Silander, and O. Axner. Dicke narrowing in the dispersion mode of detection and in noise-immune cavity-enhanced optical heterodyne molecular spectroscopy—theory and experimental verification. *Journal of the Optical Society of America B*, 28(10):2390–2401, 2011. (Cited on pages 5, 6, and 12.)

[43] A. Foltynowicz, I. Silander, and O. Axner. Reduction of background signals in fiber-based NICE-OHMS. *Journal of the Optical Society of America B*, 28(11):2797–2805, 2011. (Cited on pages 5, 6, 17, 18, 19, 52, 66, and 80.)

[44] I. Silander, P. Ehlers, J. Wang, and O. Axner. Frequency modulation background signals from fiber-based electro optic modulators are caused by crosstalk. *Journal of the Optical Society of America B*, 29(5):916–923, 2012. (Cited on pages 5, 6, and 17.)

[45] P. Ehlers, I. Silander, J. Wang, and O. Axner. Fiber-laser-based noise-immune cavity-enhanced optical heterodyne molecular spectrometry instrumentation for doppler-broadened detection in the 10^{-12} cm^{-1} $Hz^{-1/2}$ region. *Journal of the Optical Society of America B*, 29(6):1305–1315, 2012. (Cited on pages 5, 6, 18, 51, 52, 54, 55, and 68.)

[46] P. Ehlers, I. Silander, J. Wang, A. Foltynowicz, and O. Axner. Fiber-laser-based noise-immune cavity-enhanced optical heterodyne molecular spectrometry incorporating an optical circulator. *Optics Letters*, 39(2): 279–282, 2014. (Cited on pages 5, 6, and 18.)

[47] J. Wang, P. Ehlers, I. Silander, and O. Axner. On the accuracy of the assessment of molecular concentration and spectroscopic parameters by frequency modulation spectrometry and NICE-OHMS. *Journal of Quantitative Spectroscopy & Radiative Treansfer*, 136:28–44, 2014. (Cited on pages 5, 6, and 18.)

[48] P. Ehlers, I. Silander, and O. Axner. Doppler broadened NICE-OHMS – Optimum modulation and demodulation conditions, cavity length, and modulation order. *Journal of the Optical Society of America B*, 31(9): 2051–2060, 2014. (Cited on pages 5, 6, 37, and 41.)

[49] P. Ehlers, J. Wang, I. Silander, and O. Axner. Doppler broadened nice-ohms beyond the triplet formalism: assessment of optimum modulation index. *Journal of the Optical Society of America B*, 31:1499–1507, 2014. (Cited on pages 5 and 6.)

[50] P. Ehlers, A. Johansson, I. Silander, A. Foltynowicz, and O. Axner. On the use of etalon-immune-distances to reduce the influence of background signals in frequency modulation spectroscopy and NICE-OHMS. *Journal of the Optical Society of America B*, 2014. (Cited on pages 5, 6, and 52.)

[51] J. Wang, P. Ehlers, I. Silander, J. Westberg, and O. Axner. Speed-dependent Voigt dispersion line-shape function: applicable to techniques measuring dispersion signals. *Journal of the Optical Society of America B*, 20(10): 2971–2979, 2012. (Cited on pages 5, 6, and 12.)

[52] J. Wang, P. Ehlers, I. Silander, and O. Axner. Speed- dependent effects in dispersion mode of detection and in noise-immune cavity-enhanced optical heterodyne molecular spectrometry: experimental demonstration and validation of predicted line shape. *Journal of the Optical Society of America B*, 29(10):2980–2989, 2012. (Cited on pages 5, 6, and 12.)

[53] K.N. Crabtree, J.N. Hodges, B.M. Siller, A.J. Perry, J.E. Kelly, P.A. Jenkins, and B.J. McCall. Sub-doppler mid-infrared spectroscopy of molecular ions. *Chemical Physics Letters*, 512:1–6, 2012. (Cited on pages 5 and 81.)

[54] M.W. Porambo, B.M. Siller, J.M. Pearson, and B.J. McCall. Broadly tunable mid-infrared noise-immune cavity-enhanced optical heterodyne molecular spectrometer. *Optics Letters*, 37:4422–4424, 2012. (Cited on pages 5 and 81.)

[55] J.N. Hodges, A.J. Perry, P.A. Jenkins, B.M. Siller, and B.J. McCall. High-precision and high-accuracy rovibrational spectroscopy of molecular ions. *The Journal of Chemical Physics*, 139:164201, 2013. (Cited on pages 5 and 81.)

[56] A. Khodabakhsh, C. Abd Alrahman, and A. Foltynowicz. Noise-immune cavity-enhanced optical frequency comb spectroscopy. *Optics Letters*, 39 (17):5034–5038, 2014. (Cited on page 5.)

[57] F.J.M. Harren. External Cavity Quantum Cascade Laser baced NICE-OHMS. `http://www.ru.nl/tracegasfacility/trace_gas_research/experimental-setups/ec-qcl-baced-nice/`. [Online, accessed 30-July-2014]. (Cited on pages 5 and 81.)

[58] B.M. Siller and B.J. McCall. *Cavity-Enhanced Spectroscopy and Sensing*, volume 179 of *Springer Series in Optical Sciences*, chapter 7: Applications of NICE-OHMS to Molecular Spectroscopy, pages 253–270. Springer, 2014. (Cited on page 5.)

[59] Peter W. Milonni and Joseph H. Eberly. *Lasers*. John Wiley and Sons, Inc., 1988. (Cited on pages 6, 9, 10, 15, and 24.)

[60] W. Demtröder. *Laser Spectroscopy*. Springer Verlag, 1996. (Cited on pages 6, 9, and 10.)

[61] L.S. Rothman, I.E. Gordon, A. Barbe, D. Brenner, D. Chris, P.E. Bernath, M. Birk, V. Boudon, and L.R. Brown et al. The HITRAN 2008 molecular spectroscopic database. *Journal of Quantitative Spectroscopy & Radiative Treansfer*, 110:533–572, 2009. (Cited on pages 7, 8, 77, and 81.)

[62] R. H. Dicke. The Effect of Collisions upon the Doppler Width of Spectral Lines. *Physical Review*, 89(2):472–473, 1953. (Cited on page 12.)

[63] L. Galatry. Simultaneous effect of Doppler and foreign gas broadening on spectral lines. *Physical Review*, 122:1218–1223, 1961. (Cited on page 12.)

[64] S. G. Rautian and I. I. Sobel'man. Effect of collisions on Doppler broadening of spectral lines. *Soviet Physics Uspekhi*, 9:701–716, 1967. (Cited on page 12.)

[65] P. R. Berman. Speed-dependent collisional width and shift parameters in spectral profiles. *Journal of Quantitative Spectroscopy & Radiative Treansfer*, 12:1331–1342, 1972. (Cited on page 12.)

[66] F. Rohart, H. Mader, and H.W. Nicolaisen. Speed dependence of rotational relaxation induced by foreign gas collisions - studies on CH_3F by millimeter-wave coherent transients. *Journal of Chemical Physics*, 101(8):6475–6486, 1994. (Cited on page 12.)

[67] C.D. Boone, K.A. Walker, and P.F. Bernath. An efficient analytical approach for calculating line mixing in atmospheric remote sensing applications. *Journal of Quantitative Spectroscopy & Radiative Treansfer*, 112 (6):980–989, 2011. (Cited on page 12.)

[68] C.D. Boone, K.A. Walker, and P.F. Bernath. Speed-dependent Voigt profile for water vapor in infrared remote sensing applications. *Journal of Quantitative Spectroscopy & Radiative Treansfer*, 105(3):525–532, 2007. (Cited on page 12.)

[69] G.C. Bjorklund. Frequency-modulation spectroscopy: a new method for measuring weak absorptions and dispersions. *Optics Letters*, 5:15, 1980. (Cited on pages 13 and 14.)

[70] G.C. Bjorklund, M.D. Levenson, W. Lenth, and C. Ortiz. Frequency modulation (FM) spectroscopy. *Applied Physics B*, 32(3):145–152, 1983. (Cited on page 13.)

[71] J.M. Supplee, E.A. Whittaker, and W. Lenth. Theoretical description of frequency-modulation and wavelength modulation spectroscopy. *Applied Optics*, 33(27):6294–6302, 1994. (Cited on pages 13 and 14.)

[72] E.A. Whittaker, M. Gehrtz, and G.C. Bjorklund. Residual amplitude-modulation in laser electro-optic phase modulation. *Journal of the Optical Society of America B*, 2(8):1320–1326, 1985. (Cited on pages 13 and 18.)

[73] R.W.P. Drever, J.L. Hall, F.V. Kowalski, J. Hough, G.M. Ford, A.J. Munley, and H. Ward. Laser phase and frequency stabilization using an optical-resonator. *Applied Physics B*, 31(2):97–105, 1983. (Cited on pages 13, 31, 36, and 52.)

[74] I.A. Stegun and M. Abramowitz. *Handbook of mathematical functions.* Dover Pubn Inc., 1965. (Cited on page 15.)

[75] G.E. Hall and S.W. North. Transient laser frequency modulation spectroscopy. *Annual Review of Physical Chemistry*, 51:243–274, 2000. (Cited on page 17.)

[76] Y. Chen, K. Lehmann, J. Kessler, B.S. Lollar, G.L. Couloume, and T.C. Onstott. Measurement of the C-13/C-12 of Atmospheric CH4 Using Near-Infrared (NIR) Cavity Ring-Down Spectroscopy. *Analytical Chemistry*, 85 (23):11250–11257, 2013. (Cited on page 18.)

[77] M. Nikodem and G. Wysocki. Suppressing the influence of optical fringes in dispersion spectroscopy. *Photonics Letters of Poland*, 5:152–154, 2013. (Cited on page 18.)

[78] M.V. Klein and T.E. Furtak. *Optics.* John Wiley and Sons, Inc., 1986. (Cited on page 26.)

[79] R.W. Fox, C.W. Oates, and L.W. Hollberg. *Cavity-enhanced spectroscopies*, volume 40 of *Experimental Methods in the Physical Sciences*, chapter 1: Stabilizing diode lasers to high-finesse cavities, pages 1–46. Elsevier Science, 2002. (Cited on pages 29, 30, 31, and 32.)

[80] U. Tietze and C. Schenk. *Advanced Electronic Circuits.* Springer Verlag, 1978. (Cited on page 32.)

[81] R.G. deVoe and R.G. Brewer. Laser frequency division and stabilization. *Physical Review A*, 30(5):2827–2829, 1984. (Cited on pages 36 and 53.)

[82] W. Demtröder. *Experimentalphysik 1 – Mechanik und Wärme.* Springer Verlag, 2003. (Cited on page 43.)

[83] J.D. Ingle and S.R. Crouch. *Spectrochemical Analysis.* Prentice Hall, 1988. (Cited on pages 44, 48, and 49.)

[84] Graphic inspired by Wikipedia. Normal distribution – Wikipedia, the free encyclopedia, 2012. [Online; accessed 18-April-2012]. (Cited on page 44.)

[85] D.W. Allan. Statistics of atomic frequency standards. *Proceedings of the IEEE*, 54(2):221–230, 1966. (Cited on page 44.)

[86] P. Werle, R. Mucke, and F. Slemr. The limits of signal averaging in atmospheric trace-gas monitoring by tunable diode-laser absorption-spectroscopy (TDLAS). *Applied Physics B*, 57(2):131–139, 1993. (Cited on page 44.)

[87] J.A. Barnes. Tables of Bias Functions, B1 and B2, for Variances Based on Finite Samples of Processes with Power Law Spectral Densities, 1969. National Bureau of Standards Technical Note 375. (Cited on page 44.)

[88] D.W. Allan. Should the classical variance by used as a basic measure in standard metrology? *IEEE Transactions on Instrumentation and Measurement*, 36(2):646–645, 1987. (Cited on page 46.)

[89] L.A. Currie. Detection and quantification limits: origins and historical overview. *Analytica Chimica Acta*, 391:127–134, 1999. (Cited on pages 48 and 49.)

[90] L.A. Currie. Detection: International update, and some emerging dilemmas involving calibration, the blank, and multiple detection decisions. *Chemometrics and Intelligent Laboratory Systems*, 37:151–181, 1997. (Cited on page 48.)

[91] International Organization of Standardization (ISO). ISO/CD 11843-1,2 capability of detection (1995,1996), ISO/TC69/SC6, P. Wilrich, Chairman. (Cited on page 48.)

[92] L.A. Currie. Nomenclature in evaluation of analytical methods including detection and quatification capabilities. *Pure and Applied Chemistry*, 67 (10):1699–1726, 1995. (Cited on page 48.)

[93] L. Lundsberg-Nielsen, F. Hegelund, and F.M. Nicolaisen. Analysis of the high-resolution spectrum of ammonia ($^{14}NH_3$) in the near-infrared-region, 6400-6900 cm^{-1}. *Journal of Molecular Spectroscopy*, 162:230–245, 1993. (Cited on page 77.)

[94] M. Metsala, F.M. Schmidt, M. Skytta, O. Vaittinen, and L. Halonen. Acetylene in breath: background levels and real-time elimination kinetics after smoking. *Journal of Breath Research*, 4:046003, 2010. (Cited on page 78.)

Scientific Publications

Comments on the publications and my contributions to them

This thesis is based on the following scientific publications:

Publication I

Distributed-feedback-laser-based NICE-OHMS in the pressure-broadened regime

Optics Express Vol. 18, 18580–18591 (2010)

Aleksandra Foltynowicz, Junyang Wang, **Patrick Ehlers**, and Ove Axner

In this work, a NICE-OHMS instrumentation was realized around a distributed feedback (DFB) laser at 1.551 µm and a cavity with a finesse of 460. For the first time, several NICE-OHMS Doppler broadened transitions were targetable within the same scan at pressures up to 1/3 of an atmosphere, allowing for accurate relative quantitative investigations of acetylene transtitions. The 1σ-detection sensitivity was determined to be $1.5 \times 10^{-9}\,\mathrm{cm}^{-1}\ \mathrm{Hz}^{\ -1/2}$.

I took part in the development of the instrumentation and was partly responsible for the construction of the cavity. I contributed to data acquisition and analysis (except of the part concerning the assessment of the Allan variance). I took part in discussions, as well as the revision of the manuscript.

Publication II

Dicke narrowing in the dispersion mode of detection and in noise-immune cavity-enhanced optical heterodyne molecular spectroscopy – theory and experimental verification

Journal of the Optical Society of America B Vol. 28, 2390–2401 (2011)

Junyang Wang, **Patrick Ehlers**, Isak Silander, and Ove Axner

This paper is a first demonstration of Dicke narrowing in dispersion mode of detection. The effects of Dicke narrowing have been investigated and compared

for both the absorption and dispersion mode of detection, including a discussion of the relevant spectroscopic parameters. An expression for the dispersive counterpart of the conventional Rautian and Galatry line shape functions has been derived and proven to hold experiments.

My contrution to this work was primarily concerning the experimental part: I took part in the planning and execution of the measurements. I contributed to discussions and was part of the internal revision of the manuscript.

Publication III

Frequency modulation background signals from fiber-based electro optic modulators are caused by crosstalk

Journal of the Optical Society of America B Vol. 29, 916–923 (2012)

Isak Silander, **Patrick Ehlers**, Junyang Wang, and Ove Axner

This work provides a basis for the fact that background signals in fiber-coupled electro-optic modulators are caused by cross-coupling between the axes of the fibers and those of the crystal and thus cannot be cancelled out by the use of pre- or succeding polarizers. In turn, it is shown that a careful designed control of the crystal temperature and the DC voltage across the crystal can eliminate background signals originating from EOMs.

I took part in discussions concerning the theory, prepared Figure 1 in the manuscript, and contributed to the internal revision process of the manuscript.

Publication IV

Fiber-laser-based noise-immune cavity-enhanced optical heterodyne molecular spectrometry instrumentation for Doppler-broadened detection in the $10^{-12}\,\mathrm{cm}^{-1}\,\mathrm{Hz}^{-1/2}$ region

Journal of the Optical Society of America B Vol. 29, 1305–1315 (2012)

Patrick Ehlers, Isak Silander, Junyang Wang, and Ove Axner

In this work, the laser-cavity jitter of FLB-NICE-OHMS has been significantly reduced by the implementation of an acousto-optic modulator (AOM). The quality of the locking performance has been analyzed and the system noise and stability was assessed and compared to a version of the experiment without an AOM. Environmental influences have been reduced by placing the experiment on a double-table-solution, isolated from the laboratory by a transparent thermoplastix box. For the first time, FLB-NICE-OHMS showed a detection performance in the $10^{-12}\,\mathrm{cm}^{-1}\,\mathrm{Hz}^{-1/2}$ region.

I was responsible for the entire work concerning the implementation of the AOM for mode-locking. I took part in the planning of the double-table solution and the thermoplastic box. I planned, performed, and analyzed all measurements. I have written major parts of the manuscript.

Erratum. The Eqs. (7) and (8) are, according to the text, supposed to be area-normalized. As these equations presently are written, they are not. Therefore, they need to be multiplied by χ_0. Moreover, χ_{fm} is supposed to be dimensionless. This implies that Eq. (6) needs to be multiplied with χ_0^{-1}. These changes do not influence any of the results presented or conclusions drawn in the paper.

Publication V

Speed-dependent Voigt dispersion line-shape function: applicable to techniques measuring dispersion signals

Journal of the Optical Society of America B Vol. 29, 2971–2979 (2012)

Junyang Wang, **Patrick Ehlers**, Isak Silander, Jonas Westberg, and Ove Axner

This work is the theoretical basis for the accompanying experimental verification in **publication VI**. For the first time, an analytical expression for speed-dependent effects (SDEs) in dispersion line shapes is presented, basing upon a speed-dependent Voigt (SDV) line shape function for absorption spectrometry. It is validaded that for small SDEs the suggested expression approaches the ordinary Voigt line shape function.

I took part in discussions concerning the theory and simulations, as well as in the internal revision process of the manuscript.

Publication VI

Speed-dependent effects in dispersion mode of detection and in noise-immune cavity-enhanced optical heterodyne molecular spectrometry: experimental demonstration and validation of predicted line shape

Journal of the Optical Society of America B Vol. 29, 2980–2989 (2012)

Junyang Wang, **Patrick Ehlers**, Isak Silander, and Ove Axner

Speed-dependent effects (SDEs) have been assessed and compared for the absorption and dispersion mode of detection by a NICE-OHMS instrumentation. This was a first demonstration of the existence of SDEs in dispersion line shapes, validating the expressions derived and suggested in the accompanying **publication V**.

I took part in the planning and execution of all measurements performed for this work, as well as in discussions about the results. I contributed to the internal revision process of the manuscript.

Publication VII

NICE-OHMS – Frequency Modulation Cavity-Enhanced Spectroscopy – Principles and Performance

Chapter 6 in "Cavity-Enhanced Spectroscopy and Sensing", Springer Series in Optical Sciences Vol. 179 (2014)

Ove Axner, **Patrick Ehlers**, Aleksandra Foltynowicz, Isak Silander, and Junyang Wang

This comprehensive work is a review of the principles and performance of the NICE-OHMS technique. The theory for both Doppler-broadened and sub-Doppler NICE-OHMS is presented. Both a generic and the FLB-NICE-OHMS instrumentation are presented, as well as some typical results achievable with the technique.

I contributed to the planning and outline of the book chapter and have prepared sections 6.3 and parts of 6.4 of the manuscript. Furthermore, I was responsible for the preparation of all figures in the manuscript; while some already existed (mostly in a different layout though) and others had to be created. I contributed to the internal revision process of the manuscript.

Publication VIII

Fiber-laser-based noise-immune cavity-enhanced optical heterodyne molecular spectrometry incorporating an optical circulator

Optics Letters, Vol. 39, 279–282 (2014)

Patrick Ehlers, Isak Silander, Junyang Wang, Aleksandra Foltynowicz, and Ove Axner

In this work, a fiber-coupled optical circulator was implemented into the cavity-reflection pick-up-scheme in a FLB-NICE-OHMS instrumentaton. It was shown that the system performance was only slightly affected by the use of more fiber components. The system noise was assessed to $7 \times 10^{-12}\,\mathrm{cm}^{-1}\ \mathrm{Hz}^{-1/2}$ for the Doppler-broadened mode of detection and $1 \times 10^{-11}\,\mathrm{cm}^{-1}\ \mathrm{Hz}^{-1/2}$ for the sub-Doppler mode of detection and for integration times up to 20 and 10 seconds, respectively.

I was responsible for the planning and execution of all measurements, as well as the data analysis. I have written major parts of the manuscript and produced and prepared all figures.

Publication IX

On the accuracy of the assessment of molecular concentration and spectroscopic parameters by frequency modulation spectrometry and NICE-OHMS

Journal of Quantitative Spectroscopy and Radiative Transfer
Vol. 136, 28–44 (2014)

Junyang Wang, **Patrick Ehlers**, Isak Silander, Ove Axner

This work presents a thorough scrutiny of the inaccuricies of spectrometric parameters retrieved from curve fitting. Different line shape models and the influence of the detection phase are compared and discussed.

I took part in discussions of this work and contributed to the internal review of the manuscript.

Publication X

Doppler broadened NICE-OHMS – Optimum modulation and demodulation conditions, cavity length, and modulation order

Journal of the Optical Society of America B, Vol. 31, 2051–2060 (2014)

Patrick Ehlers, Isak Silander, Ove Axner

In this work, the optimum design of a NICE-OHMS instrumentation for detection of Doppler-broadened signals is discussed in terms of modulation and demodulation conditions (i.e. modulation frequency, modulation index, and detection phase), and cavity length. Simulations for various conditions were performed for both the case of pure Doppler broadening and the case when collisional broadening contributes to the same amount as Doppler-broadening. For a given cavity length, it is also discussed what is the most beneficial choice of the modulation order.

I performed all simulations in this chapter and contributed significantly to the writing of the manuscript.

Publication XI

NICE-OHMS beyond the triplet formalism: assessment of the optimum modulation index

Journal of the Optical Society of America B, Vol. 31, 1499–1507 (2014)

Patrick Ehlers, Junyang Wang, Isak Silander, Ove Axner

This work investigates the influence of the modulation index on Db-NICE-OHMS signals. It is shown that the line shape proposed in the foregoing publication holds for different modulation indices up to 2.4, both in the presence and absence of optical saturation. Moreover, it is investigated how a curve fitting procedure reacts if one neglects higher order sidebands, and to which extent the detection sensitivity can be increased for detection at the modulation index that yields largest signal size compared to the case for a commonly-used modulation index.

I was responsible for all measurements and the data evaluation in this work. I have taken part in all discussions and have written substantial parts of the manuscript.

Publication XII

On the use of etalon-immune-distances to reduce the influence of background signals in frequency modulation spectroscopy and noise-immune cavity-enhanced optical heterodyne molecular spectrometry

Journal of the Optical Society of America B (submitted in 2014)

Patrick Ehlers, Alexandra Johansson, Isak Silander, Aleksandra Foltynowicz,

Ove Axner

The concept of etalon-immune-distances (EIDs) is scrutinized in this work, both for pure FMS and NICE-OHMS. The etalon contribution to the detected FMS signal has been investigated as a function of etalon-surface spacing and it has been shown which impact the EID concept has on NICE-OHMS signals and the detection sensitivity of NICE-OHMS.

I supervised the Master thesis work, on which the measurements for the FMS part of this work is based on. Moreover, I was fully responsible for the NICE-OHMS measurements. I took part in discussions and have written parts of the manuscript.

Publication XIII

Noise-immune cavity-enhanced analytical atomic spectrometry – NICE-AAS – a technique for detection of elements down to zeptogram amounts

Spectrochimica Acta B (accepted for publication in 2014)

Ove Axner, **Patrick Ehlers**, Thomas Hausmaninger, Isak Silander, and Weiguang Ma

In this work, the transfer of NICE-OHMS towards analytical atomic spectrometry (AAS) is investigated at the example of mercury (Hg) and sodium (Na). Converting the best FL-NICE- OHMS detection sensitivity, i.e. $4.9 \times 10^{-12}\,\mathrm{cm}^{-1}\,\mathrm{Hz}^{-1/2}$ over 10 s, it should be possible to detect5 25 Hg-atoms per cubic centimeter (corresponding to $10\,\mathrm{zg/cm}^3$) or solely 15 Na-atoms per cubic centimeter when injected into a graphite furnace, the latter corresponding to an analyte concentration in the parts-per-sextillion (pps, $1{:}10^{21}$) range, which is orders of magnitude better than any previously realized laser-based AAS technique.

I contributed with MATLAB-codes for some of the simulations performed in this work and took part in the internal review process of the manuscript.

Publication I

Distributed-feedback-laser-based NICE-OHMS in the pressure broadened regime

Optics Express Vol. 18, 18580–18591 (2010)

Aleksandra Foltynowicz, Junyang Wang, **Patrick Ehlers**, and Ove Axner

Publication II

Dicke narrowing in the dispersion mode of detection and in NICE-OHMS – theory and experimental verification

Journal of the Optical Society of America B Vol. 28, 2390–2401 (2011)

Junyang Wang, **Patrick Ehlers**, Isak Silander, and Ove Axner

Publication III

Frequency modulation background signals from fiber-based electro optic modulators are caused by crosstalk

Journal of the Optical Society of America B Vol. 29, 916–923 (2012)

Isak Silander, **Patrick Ehlers**, Junyang Wang, and Ove Axner

Publication IV

Fiber-laser-based noise-immune cavity-enhanced optical heterodyne molecular spectrometry instrumentation for Doppler-broadened detection in the 10^{-12} cm^{-1} $Hz^{-1/2}$ region

Journal of the Optical Society of America B Vol. 29, 1305–1315 (2012)

Patrick Ehlers, Isak Silander, Junyang Wang, and Ove Axner

Publication V

Speed-dependent Voigt dispersion line-shape function: applicable to techniques measuring dispersion signals

Journal of the Optical Society of America B Vol. 29, 2971–2979 (2012)

Junyang Wang, **Patrick Ehlers**, Isak Silander, Jonas Westberg, and Ove Axner

Publication VI

Speed-dependent effects in dispersion mode of detection and in noise-immune cavity-enhanced optical heterodyne molecular spectrometry: experimental demonstration and validation of predicted line shape

Journal of the Optical Society of America B Vol. 29, 2980–2989 (2012)

Junyang Wang, **Patrick Ehlers**, Isak Silander, and Ove Axner

Publication VII

NICE-OHMS – Frequency Modulation Cavity-Enhanced Spectroscopy – Principles and Performance

Chapter 6 in "Cavity-Enhanced Spectroscopy and Sensing", Springer Series in Optical Sciences Vol. 179 (2014)

Ove Axner, **Patrick Ehlers**, Aleksandra Foltynowicz, Isak Silander, and Junyang Wang

Publication VIII

Fiber-laser-based noise-immune cavity-enhanced optical heterodyne molecular spectrometry incorporating an optical circulator

Optics Letters, Vol. 39, pages 279–282 (2014)

Patrick Ehlers, Isak Silander, Junyang Wang, Aleksandra Foltynowicz, and Ove Axner

Publication IX

On the accuracy of the assessment of molecular concentration and spectroscopic parameters by frequency modulation spectrometry and NICE-OHMS

Journal of Quantitative Spectroscopy and Radiative Transfer, Vol. 136, pages 28–44 (2014)

Junyang Wang, **Patrick Ehlers**, Isak Silander, Ove Axner

Publication X

Doppler broadened NICE-OHMS – Optimum modulation and demodulation conditions, cavity length, and modulation order

Journal of the Optical Society of America B, Vol. 31, pages 2051–2060 (2014)

Patrick Ehlers, Isak Silander, Ove Axner

Publication XI

NICE-OHMS beyond the triplet formalism: assessment of the optimum modulation index

Journal of the Optical Society of America B, Vol. 31, pages 1499–1507 (2014)

Patrick Ehlers, Junyang Wang, Isak Silander, Ove Axner

Publication XII

On the use of etalon-immune-distances to reduce the influence of background signals in frequency modulation spectroscopy and noise-immune cavity-enhanced optical heterodyne molecular spectrometry

Journal of the Optical Society of America B (submitted in 2014)

Patrick Ehlers, Alexandra Johansson, Isak Silander, Aleksandra Foltynowicz, Ove Axner

Publication XIII

Noise-immune cavity-enhanced analytical atomic spectrometry – NICE-AAS – a technique for detection of elements down to zeptogram amounts

Spectrochimica Acta B (accepted for publication in 2014)

Ove Axner, **Patrick Ehlers**, Thomas Hausmaninger, Isak Silander, and Weiguang Ma

Institutionen för fysik
Umeå universitet
SE-901 87 Umeå

www.umu.se

ISBN 978-91-7601-107-2